ILMATIETEEN LAITOS
METEOROLOGISKA INSTITUTET
FINNISH METEOROLOGICAL INSTITUTE

135
CONTRIBUTIONS

ATMOSPHERIC WATER VAPOR AND THE AEROSOL DIRECT RADIATIVE EFFECT: REMOTE SENSING AND GLOBAL MODEL STUDIES

JANI HUTTUNEN

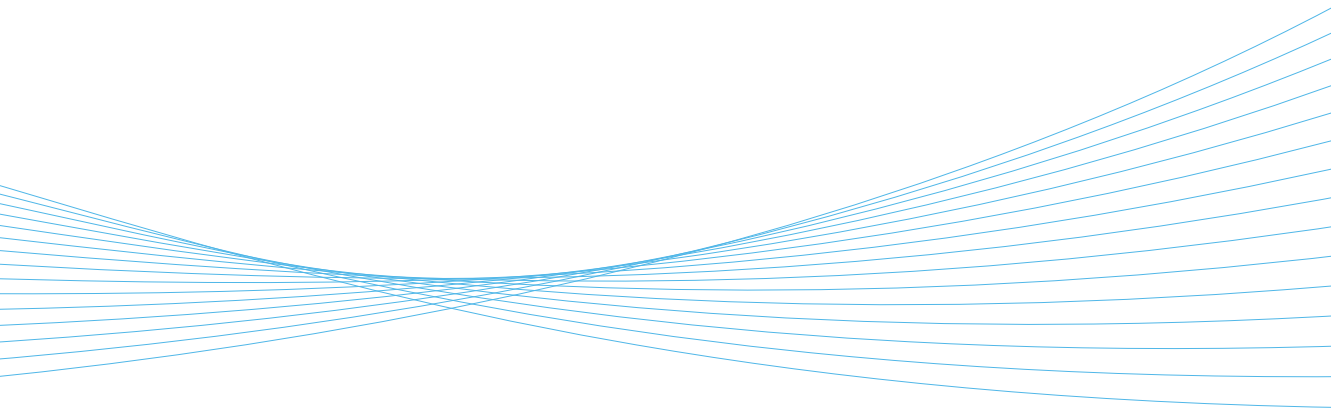

FINNISH METEOROLOGICAL INSTITUTE

Published by Finnish Meteorological Institute
(Erik Palménin aukio 1) , P.O. Box 503
FIN-00101 Helsinki, Finland

Series title, number and report code of publication
Finnish Meteorological Institute No. 135

Date 31st July 2017

Author(s)
Jani Huttunen

Name of project

Commissioned by Finnish Meteorological Institute

Title
ATMOSPHERIC WATER VAPOR AND THE AEROSOL DIRECT RADIATIVE EFFECT: REMOTE SENSING AND GLOBAL MODEL STUDIES

Abstract

Aerosols affect the climate both directly and indirectly. The direct effect comes from their influence on the radiation balance by scattering and absorption of solar radiation, while the indirect effect is based on the ways in which aerosols interact via clouds. Currently the total anthropogenic aerosol forcing includes one of the main uncertainties in the assessment of human induced climate change. The aerosol direct radiative effect (ADRE) can be simulated with either the radiative transfer modelling or estimated with solar radiation and aerosol amount measurements. Both approaches include significant uncertainties and this thesis focuses on the uncertainties on the measurement-based estimation of ADRE and the uncertainties therein.

The main scientific objectives of this thesis are to seek answers to the following four questions: 1) are the machine learning algorithms better than the a traditional look-up table (LUT) approach in estimating aerosol load (aerosol optical depth, AOD)?; 2) what is the role of water vapor (WVC) variability in the measurement-based regression method used to estimate the surface ADRE?; 3) how well do the radiative transfer codes, typically used in global aerosol models, agree?; 4) what is the impact of typically neglected diurnal aerosol variability in ADRE estimation?

The results show that: 1) the machine learning algorithms are able to provide AOD more accurately than the LUT approach for conditions of varying aerosol optical properties, since in the LUT approach the aerosol model (e.g. single scattering albedo, asymmetry factor) needs to be fixed in advance. 2) It was found that co-variability of AOD and WVC can have an influence in ADRE estimates, when using ground-based measurements of surface solar radiation and AOD. This has not been taken into account previously, but needs to be considered when these methods are applied. 3) The model inter-comparison study, in which the models estimated the radiative fluxes for the same atmospheric states, revealed that there is relatively large diversity between models regarding the results from their radiative transfer modelling. 4) The main conclusion from the study focusing on the impact of systematic diurnal AOD cycles in aerosol direct radiative effect, was that even a notable diurnal change in AOD does not typically affect the 24h-average ADRE significantly.

Publishing unit

Classification (UDC)

Keywords aerosol, radiation, water vapor, remote sensing, climate model

ISSN and series title 0782-6117

ISBN 978-952-336-026-6 Language English Pages 48

ILMATIETEEN LAITOS

Julkaisun sarja, numero ja raporttikoodi
Ilmatieteen laitos Num. 135

Julkaisija Ilmatieteen laitos, (Erik Palménin aukio 1)
PL 503, 00101 Helsinki

Tekijä(t)
Jani Huttunen

Toimeksiantaja Ilmatieteen laitos

Nimeke

ILMAKEHÄN VESIHÖYRY JA AEROSOLIEN SUORA SÄTEILYPAKOTE: KAUKOKARTOITUKSEN JA GLOBAALIEN ILMASTOMALLIEN TUTKIMUKSIA

Tiivistelmä

Ilmakehän hiukkaset (aerosolit) vaikuttavat ilmastoon sekä suoraan että epäsuoraan. Suorassa vaikutuksessa aerosolit sirottavat ja absorboivat auringon säteilyä, kun taas epäsuorissa vaikutuksissa aerosolit vaikuttavat pilvien muodostumiseen sekä niiden haihtumiseen. Tällä hetkellä ihmislähtöisten aerosolien säteilypakote muodostaa yhden tärkeimmistä epävarmuustekijöistä ihmisen aiheuttaman ilmastonmuutoksen arvioinnissa. Aerosolin suora säteilyvaikutus (ADRE) kuvaa kuinka aerosolit vaimentavat auringon säteilyä, ja tätä voidaan simuloida säteilynkulkua mallintamalla tai arvioida samanaikaisia auringon säteily- ja aerosolimittauksia hyväksi käyttäen. Molemmat lähestymistavat sisältävät merkittäviä epävarmuustekijöitä. Tässä työssä keskityttiin näihin aerosolien aiheuttaman suoran säteilypakotteen mittausperusteisen arvioinnin epävarmuustekijöihin.

Tämän tutkielman tavoite on etsiä vastauksia seuraaviin neljään tieteelliseen kysymykseen: 1) ovatko koneoppivat algoritmit perinteistä säteilynkulun hakutaulukkoa (LUT) parempia arvioitaessa aerosolien optista paksuutta (aerosol optical depth, AOD), kun on käytettävissä auringon säteilymittauksia maanpinnalta (surface solar radiation, SSR); 2) mikä on vesihöyryn (water vapor content, WVC) vaihtelun merkitys mittausperusteisessa menetelmässä, jota käytetään aerosolien suoran säteilypakotteen arvioimiseen regressiosovituksin; 3) kuinka hyvin globaalien mallien osana toimivat säteilynkulkukoodit käyttäytyvät vertailussa kun asetetaan samat ilmakehän olosuhteet kullekin mallille; 4) Kuinka merkittävä on päivänsisäisen aerosolipitoisuuden systemaattinen vaihtelu laskettaessa aerosolien suoraa säteilypakotetta?

Tulokset osoittavat tiivistetysti seuraavat seikat: 1) koneoppivat algoritmit pystyvät määrittämään AOD:n tarkemmin kuin LUT-lähestymistapa silloin kun aerosolien optiset ominaisuudet vaihtelevat, koska LUT:ssa on oletettava ennalta nämä säteilyn kannalta oleelliset aerosolien optiset ominaisuudet (esim. aerosolien sirontatehokkuus ja siroamisen epäsymmetrisyys). 2) Aerosolin optisen paksuuden ja vesihöyryn systemaattinen vaihtelu vaikuttaa säteilypakotearvioihin käytettäessä SSR:n ja AOD:n maanpintamittauksia. Tätä ei ole otettu aiemmin huomioon, mutta olisi tärkeä huomioida näitä menetelmiä sovellettaessa. 3) Mallien välinen vertailututkimus osoittaa, että käytetyt säteilymallit tuottavat suuria eroja mallien välillä. Lisäksi vertailututkimus osoittaa, että nämä mallien keskinäiset erot ovat suunnilleen samaa luokkaa mitä aikaisemmissa samankaltaisissa tutkimuksissa. 4) Huomattavakin päivänsisäinen systemaattinen vaihtelu AOD:ssa ei tyypillisesti vaikuta ADRE:n vuorokausikeskiarvoon merkittävästi.

Julkaisijayksikkö

Luokitus (UDK)
ilmastomalli

Asiasanat aerosoli, säteily, vesihöyry, kaukokartoitus,

ISSN ja avainnimike
0782-6117

ISBN 978-952-336-026-6 Kieli englanti Sivumäärä 48

FINNISH METEOROLOGICAL INSTITUTE
CONTRIBUTIONS

No. 135

ATMOSPHERIC WATER VAPOR AND THE AEROSOL DIRECT RADIATIVE EFFECT: REMOTE SENSING AND GLOBAL MODEL STUDIES

Jani Huttunen

Finnish Meteorological Institute
Kuopio, Finland

Doctoral dissertation

To be presented, with the permission of the Faculty of Science and Forestry of the University of Eastern Finland for public examination in the Auditorium MS301, Medistudia building, University of Eastern Finland, on October 20th, 2017, at 12 o'clock noon.

Finnish Meteorological Institute

Kuopio, 2017

Author's address: Finnish Meteorological Institute
Atmospheric Research Centre of Eastern Finland
Kuopio, Finland
jani.huttunen@fmi.fi

Supervisors: Docent Antti Arola, Ph.D.
Atmospheric Research Centre of Eastern Finland
Finnish Meteorological Institute
Kuopio, Finland

Professor Kari Lehtinen, Ph.D.
Department of Applied Physics
University of Eastern Finland
Kuopio, Finland

Professor Gunnar Myhre, Ph.D.
Centre for International Climate and Environmental Research
Oslo, Norway

Preliminary examiners: Professor Jarkko Koskinen, Ph.D.
Finnish Geospatial Research Institute
Helsinki, Finland

Professor Tuukka Petäjä, Ph.D.
Division of Atmospheric Sciences, Department of Physics
University of Helsinki
Helsinki, Finland

Opponent: Professor Veli-Matti Kerminen, Ph.D.
Aerosol-Cloud-Climate Interactions Group
University of Helsinki
Helsinki, Finland

Custos: Docent Antti Arola, Ph.D.
Atmospheric Research Centre of Eastern Finland
Finnish Meteorological Institute

FINNISH METEOROLOGICAL INSTITUTE
CONTRIBUTIONS No. 135
ISBN 978-952-336-026-6 (paperback)
ISSN 0782-6117
Erweko
Helsinki 2017
ISBN 978-952-336-027-3 (pdf)
Helsinki 2017

Acknowledgements

Kuopio, July 2017

The work presented in this Thesis has been carried out at the Atmospheric Research Centre of Eastern Finland of Finnish Meteorological Institute.

I am grateful to my main supervisor Dr. doc. Antti Arola for guiding in this Thesis, and also in my master thesis, throughout the years. I also thank my supervisors Professor Gunnar Myhre and Professor Kari Lehtinen. Your guidance and support has been the most crucial for this Thesis.

I thank the preliminary examiners Professor Jarkko Koskinen and Professor Tuukka Petäjä for your examinations. Due to your comments, the text is clearer and takes into account different aspects as well.

I would like to thank all the co-authors in the papers of this Thesis. Especially I would like to thank Dr. doc. Tero Mielonen, Dr. doc. Harri Kokkola, Dr. doc. Santtu Mikkonen, Dr. doc. Anders Lindfors, MSc. Mika Mononen, Dr. Juha Reunanen, Dr. Antti Lipponen and Dr. Mika Komppula. You played a major role in this Thesis.

Moreover, I thank all the people in the Finnish Meteorological Institute, Kuopio unit, also the remote sensing group heading Professor Gerrit De Leeuw in Helsinki and the University of Eastern Finland people in the Applied physics and the Environmental sciences. I would like to thank Dr. doc. Tero Mielonen (co-author/roommate), Dr. Jussi Malila, MSc. Mikko Pitkänen, MSc. Milko Vesterinen and Dr. Harri Portin, my roommates during the years, for the interesting conversations.

I thank lecturers and supervisors over the years. Some of you are no longer here, but the tools you gave us (BSc, MSc and PhD- students), are valued (but also in the development for science).

I also thank NMR Solutions Ltd. fellows, Dipl. Chem. Matthias Niemitz, Dr. Samuli-Petrus Korhonen and Dr. Juuso Lehtivarjo, for the great introduction into the industrial business.

Furthermore, I thank Teollisuuden Voima Oyj and Posiva Oy for hiring me to the excellent job.

Finally, thanks to my friends and family. Your value is great to me.

Jani Huttunen

Contents

List of publications

This Thesis consists of an Introduction and four original papers:

Paper I: Huttunen, J., Kokkola, H., Mielonen, T., Mononen, M. E. J., Lipponen, A., Reunanen, J., Lindfors, A. V., Mikkonen, S., Lehtinen, K. E. J., Kouremeti, N., Bais, A., Niska, H., and Arola, A. Retrieval of aerosol optical depth from surface solar radiation measurements using machine learning algorithms, nonlinear regression and a radiative transfer based look-up table *Atmos. Chem. Phys.*, 16, 8181-8191, doi:10.5194/acp-16-8181-2016, 2016.

Paper II: Huttunen, J., Arola, A., Myhre, G., Lindfors, A. V., Mielonen, T., Mikkonen, S., Schafer, J. S., Tripathi, S. N., Wild, M., Komppula, M., and Lehtinen, K. E. J. Effect of water vapor on the determination of aerosol direct radiative effect based on the AERONET fluxes *Atmos. Chem. Phys.*, 14, 6103–6110, 2014.

Paper III: Randles, C. A., Kinne, S., Myhre, G., Schulz, M., Stier, P., Fischer, J., Doppler, L., Highwood, E., Ryder, C., Harris, B., Huttunen, J., Ma, Y., Pinker, R. T., Mayer, B., Neubauer, D., Hitzenberger, R., Oreopoulos, L., Lee, D., Pitari, G., Di Genova, G., Quaas, J., Rose, F. G., Kato, S., Rumbold, S. T., Vardavas, I., Hatzianastassiou, N., Matsoukas, C., Yu, H., Zhang, F., Zhang, H., and Lu, P. Intercomparison of shortwave radiative transfer schemes in global aerosol modeling: results from the AeroCom Radiative Transfer Experiment *Atmos. Chem. Phys.*, 13, 2347–2379, 2013.

Paper IV: Arola, A., Eck, T. F., Huttunen, J., Lehtinen, K. E. J., Lindfors, A. V., Myhre, G., Smirnov, A., Tripathi, S. N., and Yu, H. Influence of observed diurnal cycles of aerosol optical depth on aerosol direct radiative effect *Atmos. Chem. Phys.*, 13, 7895–7901, 2013.

J. Huttunen is responsible for the data analysis and the writing, in **Paper I** and **Paper II**. In **Paper III** J. Huttunen provided the model number six (FMI-libRadtran) simulations of the paper. In **Paper IV** J. Huttunen was involved in the analysis of the study and plotted some of the figures.

1 Introduction

Aerosols, solid and liquid particles suspended in the atmosphere, are currently the main source of the uncertainty when estimating the radiative forcing of the Earths climate (IPCC, 2013). Aerosols are either primary or secondary based on their source; primary particles are directly emitted into the atmosphere (e.g. sea salt and desert dust) as liquid or solid particles. Secondary particles are formed in the atmosphere from condensable vapor (e.g. secondary organic aerosols, Hallquist et al. 2009). Aerosols cover a large size range - from a few nanometers to hundreds of micrometers in diameter, various shapes often with highly irregular structure, and a plethora of chemical properties; ranging from single compounds to complicated mixtures, mixed either internally or externally. Their concentration ranges from almost aerosol free conditions of tens up to 100 000 per cubic centimeter (Aalto et al., 2005). Both the concentrations and properties of aerosols can exhibit large variations both spatially and temporally. Due to all this complexity, aerosols can affect radiative transfer in very different ways (IPCC, 2013).

Compared with the most important greenhouse gases, carbon dioxide and methane, the lifetimes of aerosols are much shorter - from hours to weeks. They can typically only travel distances of a few kilometers to up to hundreds of kilometers from their source (Seinfeld and Pandis, 2006). This means that local pollution episodes are typical, in which some local source can increase the aerosol concentration drastically. Such episodes can induce hazardous effects to human health (e.g. Carmichael et al., 2009), especially small aerosol particles (less than few micrometers in diameter) can enter the alveolar region of the human lung and drift to the blood circulation, causing asthma, cardiovascular diseases and even premature deaths in highly aerosol polluted urban areas throughout the world (e.g. Fang et al., 2013). This brings up an interesting potential conflict: aerosols in general cool the climate (IPCC, 2013), compensating to some extent the greenhouse gas warming due to the recent fossil fuel usage, but at the same time, they can cause serious health problems (e.g. Löndahl et al., 2010).

Aerosols affect the climate both directly and indirectly. The aerosol direct radiative effect is defined as the attenuation of solar radiation due to scattering and absorption by the aerosols (aerosolradiation interaction, e.g. Mahowald et al., 2011). The indirect effects arise from the interactions of the aerosols with water vapor (aerosolcloud interaction). Higher aerosol concentrations result in brighter clouds with longer lifetimes (e.g. Lohmann and Feichter, 2005). There is also a so-called semi-direct effect, in which nearby absorbing aerosols

can lead to evaporation of cloud droplets (Lohmann and Feichter, 2005). The scientific level of understanding of these indirect and semi-direct effects is currently still very low (IPCC, 2013). Regarding the direct effect, Myhre (2009) stated that observation-based and global aerosol model estimates have converged, reducing the uncertainty. Loeb and Su (2010), however, concluded that significant uncertainties still exist with the aerosol direct radiative effect, mainly caused by the uncertainty with the aerosol single scattering albedo, describing aerosols' ability to scatter incoming radiation. If the aerosol is purely scattering its vertical profile has negligible impact in the radiative effect. However, the effect becomes important with absorbing aerosols, particularly in case of black carbon (e.g. Samset et al. 2013). As IPCC (2013) states, the radiative forcing is caused by anthropogenic particles only and radiative effect by all aerosol particles (natural and anthropogenic).

Fig. 1 shows the anthropogenic (effective) radiative forcing of the Earth's climate between 1750 and 2011 for the main atmospheric components. Greenhouse gases produce the main part of the positive forcing, thus warming the climate, and their confidence level is very high. The confidence level of aerosol impact is low, but they probably produce a negative total forcing, hence cancelling in some extent the warming due to the greenhouse gases. Fig. 1 divides the aerosol radiative forcing into the aerosol-radiation interaction and the aerosol-cloud interaction, and both have significant uncertainty limits. Overall, the confidence level of the positive forcing caused by the greenhouse gases is high. However, the main reason for the large uncertainty in the total anthropogenic forcing is associated with the above-mentioned aerosol effects. Particularly this thesis provides improvements on the understanding of aerosol-radiation interactions and reduced the associated uncertainties in the climate forcing.

The effects of aerosols and clouds on radiation can be seen visually in Fig. 2, which shows a satellite image example of a large aerosol concentration case. The image, captured over China in June 2015, shows reflected sunlight so that both aerosols and clouds are clearly distinguishable. Fig. 3 represents the aerosol size distributions for the same day and location, only about 1.5 hours apart. As clearly seen in the figure, both the concentration and mean size of the aerosol has changed significantly within this short time. This is very typical for aerosols and is one of the main challenges both regarding observing and modeling their dynamics.

The overarching aim of this Thesis is to understand better the aerosol direct radiative effect using remote sensing and global climate modeling techniques, with a special focus on how aerosol-water vapor interactions affect it. Water

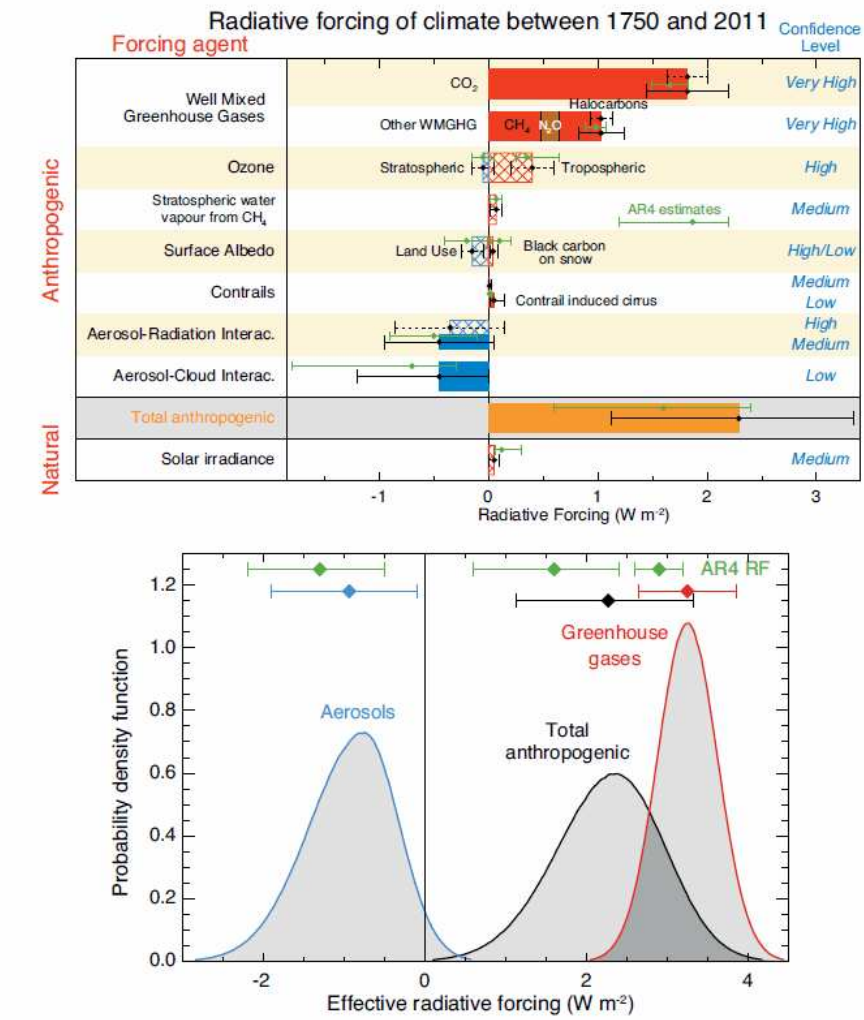

Figure 1: The effect radiative forcing (ERF) and the radiative forcing (RF) for the main atmospheric components according to the latest IPCC (2013) report. RF is defined as the change in net downward irradiance (the solar and longwave emitted by the Earth) at the tropopause while allowing for stratospheric temperatures to readjust to radiative equilibrium, holding other variables such as tropospheric temperatures, water vapour and cloud cover fixed. ERF is defined similarly as the radiative forcing, but allows for all variables to readjust except for global mean surface temperature, ocean temperature and sea ice cover. In the upper sub figure a positive number indicates warming and a negative cooling (during the Industrial Era between 1750 and 2011). Solid bars are ERF, hatched bars are RF, green diamonds and associated uncertainties are for RF assessed in the previous, IPCC (2007) report. Moreover, the confidence levels are listed. The lower sub figure shows the probability density functions for greenhouse gases, aerosols and total anthropogenic ERF. The green shows IPCC, (2007) RF 90 % confidence intervals, while the red, blue and black lines lines show IPCC, (2013) RF 90 % confidence intervals.

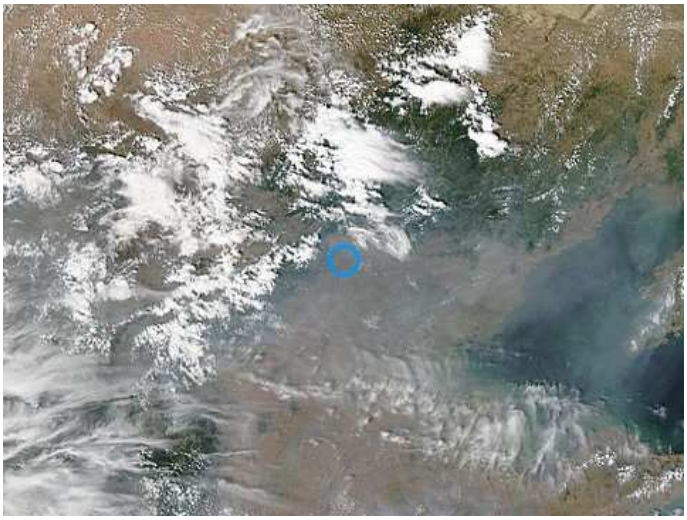

Figure 2: Image captured by the Moderate-resolution Imaging Spectroradiometer aboard Aqua-satellite (http://modis.gsfc.nasa.gov/), on June 16th 2015. The blue circle is centered to Beijing (lat: 39.98°, long: 116.38°), close to XiangHe (lat: 39.75°, long: 116.96°).

vapor affects solar radiation transfer in the atmosphere not only by absorbing itself, but also by its ability to change the aerosol optical properties. To reach this aim, the following more specific questions are studied:

1) Is it possible to estimate aerosol optical depth reliably with solar surface radiation measurements, using robust machine learning algorithms and do they perform better than a traditional look-up table generated with a radiative transfer code? Solar surface radiation measurements cover decades or even more than a century at some stations, whereas aerosol optical depth measurements are basically absent earlier than 1990s. The aerosol optical depth is the most fundamental aerosol related parameter describing indirectly the aerosol concentration. The key potential weakness of the radiative transfer code method is that it needs additional information about the atmospheric state, which may have to be guessed, and thus may result in systematically erroneous estimates of aerosol optical depth. The prescribed and fixed aerosol type is the most critical information in this respect.

2) What is the role of atmospheric water vapor in the aerosol direct radiative effect, due to its tendency to correlate with the aerosol optical depth? This information is crucial when solar radiation intensity without aerosols is esti-

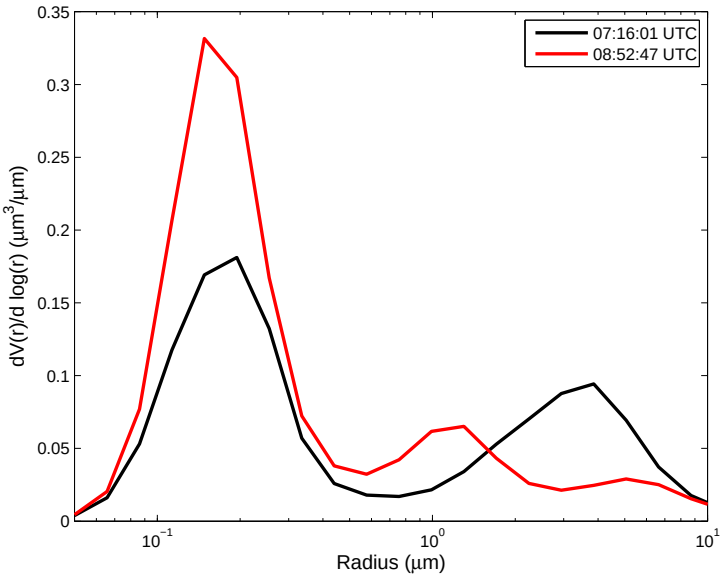

Figure 3: Aerosol size (column integrated volume) distribution (in the base-10 logarithmic scale) retrieved by the aerosol robotic network (http://aeronet.gsfc.nasa.gov/), in XiangHe-station, on June 16th 2015 (see the previous figure). The black and red lines refers for UTC time.

mated with the extrapolation method using measurements of solar irradiation and the aerosol optical depth.

3) What is the performance of an ensemble of 31 global models in estimating of the solar shortwave radiation? Setting the same atmospheric states for all the models (e.g. absorbing or scattering aerosol population), only the models characteristics produce the inter-model diversity. The study aims to understand characteristics' of the models as a purpose to develope them.

4) How does a diurnal change in the aerosol optical depth affect the aerosol direct radiative effect? Especially, are the aerosol direct radiative effect estimates derived from satellite observations valid? If yes, this would spatially extend the aerosol direct radiative effect estimates significantly. Ground-based aerosol optical depth measurements are very limited spatially, whereas satellites cover most of the Earth's surface.

2 Aerosol and solar irradiation interaction - aerosol direct radiative effect (ADRE)

Electromagnetic radiation is defined as the amount of energy transmitted via photons, which contains gamma, röntgen, ultraviolet, visible, infrared, micro and radiowavelength (e.g. Hecht, 2002). Often the unit is $\mathrm{Wm^{-2}m^{-1}}$ or $\mathrm{Wm^{-2}}$, for spectral and spectrally integrated irradiance, respectively (Liou, 2002). Solar irradiance indicates irradiance produced by the Sun, which can be approximated with the Planck's black body radiation law, giving the spectral irradiance's magnitude dependence on the wavelength. Solar surface radiation (herein SSR) is the solar irradiance detected at surface of the Earth.

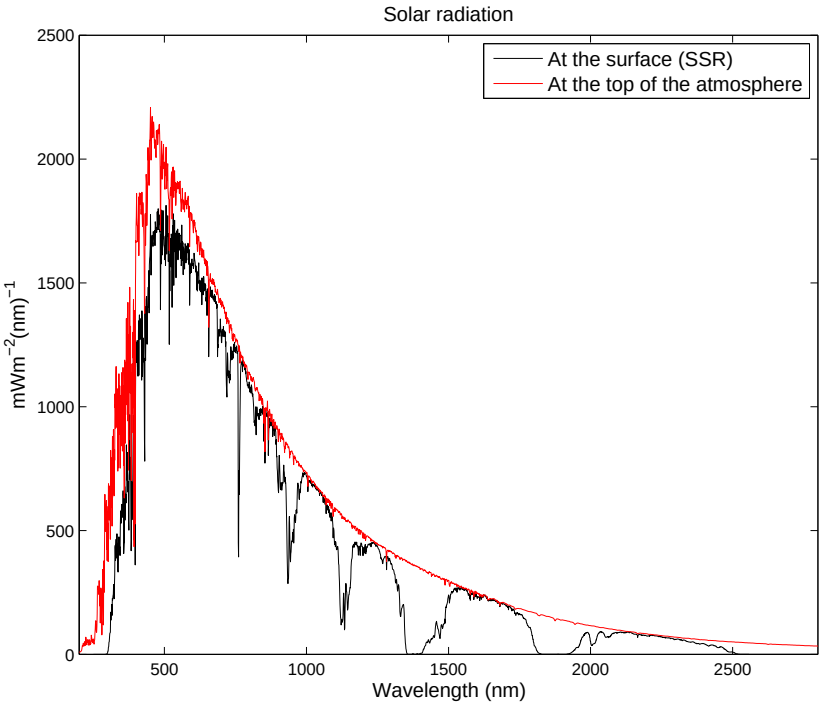

Figure 4: Solar radiation at the top of the atmosphere and at the surface (SSR) for aerosol and cloud free case, and solar zenith angle is 0°. The solar radiation was determined with the libRadtran code (Mayer and Kylling, 2005) using the Kurucz spectrum (Kurucz, 1992).

Fig. 4 shows solar irradiance at the top of the atmosphere and at the surface (SSR) for aerosol and cloud free case when the sun is overhead. At the top of the atmosphere, the annually averaged solar irradiance is roughly 1367 Wm^{-2} (the whole spectrum of the Sun, Kurucz, 1992). Visible range (roughly 400 nm - 700 nm) contains a window in the atmosphere, where the solar irradiance is not significantly attenuated (for cloud free cases), whereas for shorter than 300 nm, it is attenuated effectively, due to the nitrogen, oxygen and ozone molecules (Seinfeld and Pandis, 2006). For infrared, the solar irradiance is attenuated, mainly due to the water vapor absorption. The molecular absorption means that incident irradiances changes to vibrational, translational and rotational changes of the molecules (e.g. Modest, 2013).

I_λ, radiance (the spectral irradiance per unit solid angle), attenuates due to absorption and scattering (Bohren and Huffman, 1983) with the following relation

$$\mathrm{d}I_\lambda/\mathrm{d}z = -(\alpha+\beta)I_\lambda, \tag{1}$$

where z is the propagation length in the atmosphere (toward the normal of the surface), α and β are the absorption and scattering components of the attenuation, respectively. Integrating the absorption and scattering over the vertical atmosphere (z, altitude, goes from the top of the atmosphere to the surface), gives the total extinction (absorption + scattering) , τ,

$$\tau = \int (\alpha+\beta)dz = \tau_{\mathrm{abs}} + \tau_{\mathrm{scat}}, \tag{2}$$

gives the Aerosol Optical Depth (AOD, τ=τ_{abs} + τ_{scat}, for absorption and scattering AOD, respectively) (Bohren and Huffman, 1983). The globally and annually averaged AOD at visible (550 nm) is about 0.14 over oceans and 0.19 over land based on the satellite data (e.g. Remer et al., 2008). But regionally the seasonal average AOD can be less than 0.05 for pure conditions and more than 1 in heavily polluted urban regions.

Thus, the exponential decay holds for I_λ (eq. (1) and eq.(2) combined and then integrated),

$$I_\lambda = I_\lambda^0 e^{-m\tau}, \tag{3}$$

where I_λ^0 is the (solar) spectral radiation at the top of the atmosphere. I_λ^0 is measured with the Solar Zenith Angle (SZA) aparting from direction of

the surface's normal. AOD is vertical extinction, therefore the slant path effect needs to be taken into account by air mass factor, m. m normalizes the increased attenuation by the longer optical path in the atmosphere. Moreover, m can be approximated by the plane-parallel atmosphere (excluding the Earth's curvature) for Solar Zenith Angle (SZA, θ) less than 80° by $\sec(\theta) = m$. Fig. 5 shows the increased optical path length with respect of SZA. For SZA larger than 80°, the plane-parallel approximation does not hold, and more sophisticated approximations are needed (e.g. Kasten and Young, 1989).

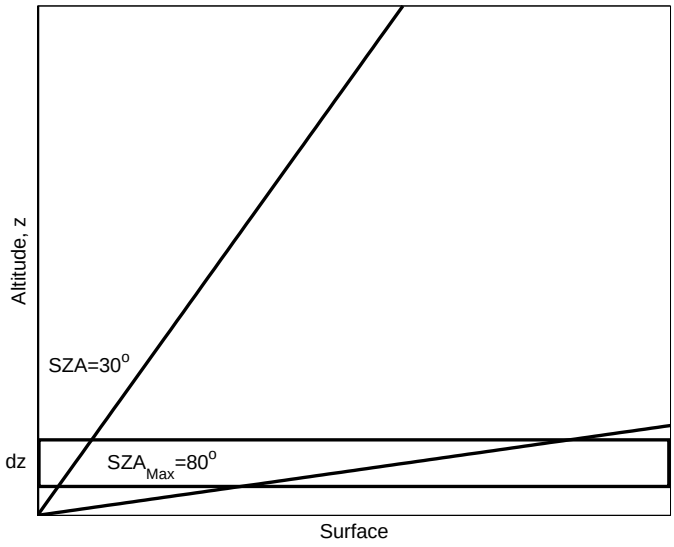

Figure 5: A representation of the plane parallel approximation, which ignores the Earth's curvature (the atmosphere continues horizontally infinitely). The vertical axis of the Earth (altitude in the atmosphere) and the Sun lead to Solar Zenith Angle (SZA), and the optical path of solar radiation through the atmosphere depends on this angle. As the rectangle shows, as an example for SZA=30°, the optical path is significantly increased compared with the vertical and have to be normalized for AOD independent on SZA. The maximum SZA is roughly 80° for the plane parallel approximation.

As eq. (3) shows, AOD is derived for a certain wavelength. However, a crucial information is the wavelength dependence of AOD and it can be approximated by Ångström law (Ångström exponent, AE, α)($\mathit{Ångström}, 1929$),

$$\alpha = -\frac{\log\frac{\tau_{\lambda_1}}{\tau_{\lambda_2}}}{\log\frac{\lambda_1}{\lambda_2}}, \tag{4}$$

where λ_1 and λ_2 are wavelengths with two different values, thus giving the AOD's spectral pattern. Often this is approximated by selecting one wavelength in the shorter and the other at the longer end of the visible spectrum. Typically small AE is an indication of the dominance by large particles (Schuster et al., 2006). Very often AE in the visible wavelengths (from 400 nm to 700 nm) ranges between 0.5 to 2, values below 1 having significant contribution by larger particles. Also the AE's change with wavelength can give an indication of the aerosol type as shown in Eck et al., (1999): AE from 380 nm to 870 nm (with a small difference between λ_1 and λ_2) can increase factor of 2-5 for biomass burning and urban aerosols, whereas it stays close to a constant for mineral dust.

Single scattering albedo (SSA, ω) describes the relative role of aerosol scattering over total extinction (scattering+absorption).

$$\omega = \frac{\tau_{\text{scat}}}{\tau_{\text{scat}} + \tau_{\text{abs}}}, \tag{5}$$

i.e. the portion of attenuation of I_λ caused by aerosol scattering. SSA has values from 0 (I_λ is totally absorbed) to 1 (totally scattered) (Bohren and Huffman, 1983). Often in the visible wavelengths, SSA is close to 0.9 or more, rarely less than 0.8 (Takemura et al., 2002). The critical single scattering albedo describes the value of SSA when the aerosol radiative effect changes from positive to negative. The critical single scattering albedo increases with increasing surface reflectance, in other words, relatively smaller aerosol absorption can lead to a positive effect over surfaces of higher reflectance (e.g. Haywood and Boucher 2000). Furthermore, SSA is a strongly wavelength dependent parameter. For large aerosols, e.g. dust, SSA increases from ultraviolet to visible wavelengths, and is close to a constant in the near infrared and a bit beyond (700 nm - 1700 nm, see Bergström et al., 2007). But for small aerosols, e.g. urban particles, SSA decreases significantly from ultraviolet to near infrared, being large for shorter wavelengths. Classification of aerosols has been attempted by using this information regarding the spectral SSA (e.g. Li et al., 2015(b)).

The asymmetry parameter (AP, g) describes the direction of scattering

$$g = \frac{1}{2} \int_0^{\pi} \mathrm{P}(\phi) \cos\phi \sin\phi \, d\phi, \tag{6}$$

where $\mathrm{P}(\phi)$ is the angular distribution of the scattered irradiance. Values of the asymmetry parameter, g, vary from -1 (totally backscattered, ϕ=180°) to 1 (totally forward scattered, ϕ=0°), whereas g=0 stands for the symmetrical, isotropic, scattering. For instance, the scattering of solar radiation by the atmospheric gaseous molecules, nitrogen and oxygen is close to isotropic, resulting in g close to zero (Bohren and Huffman, 1983). Typical values of g by atmospheric particles are in the range 0.65-0.75 (Andrews et al., 2006), thus aerosols tend to scatter the radiation much more into the forward direction. The forward scattering contribution also increases with aerosol particle size. Some aerosols, so-called hygroscopic aerosols, readily intake water vapor and thus increase by size, which results in an increase of the asymmetry parameter.

The aerosol optical depth, Ångström exponent, single scattering albedo and asymmetry parameter are the main parameters, which determine the aerosol optical properties, amount and their influence in aerosol-radiation interactions. These interactions can be described more fundamentally with the aerosol size distribution and the complex refractive index. The complex refractive index contains real and imaginary parts, the former stands for the refraction of radiation between interface of different substances and the latter absorption/emission of radiation (Feynman et al., 1963). The aerosol size distribution and the complex refractive index determine together AOD, AE, SSA and AP. Moreover, the polarization of radiation (Mishchenko, 2014) is an additional tool to study aerosols, especially established by active remote sensing instruments using the laser-method, either space-borne or ground-based. They give information about aerosol type, e.g. separate dust from non-dust aerosols (Yu et al., 2010).

The clear-sky aerosol direct radiative effect (ADRE) is defined as the difference between the net irradiance (downward irradiance minus upward irradiance) for a clear-sky atmosphere with and without aerosols. A similar definition can be adopted for both the top of the atmosphere (TOA) and for the surface, the latter often denoted also by bottom of the atmosphere (BOA). In this thesis, the focus is on the surface radiative effects. The aerosol Direct Radiative Effect (ADRE) is defined for the surface with the following equation

$$\mathrm{ADRE}_{\mathrm{surface}} = (1 - A)(\mathrm{SSR} - \mathrm{SSR}^0), \tag{7}$$

where SSR is irradiance with and SSR^0 without aerosols, and A is surface reflectance (albedo) derived often with satellites (e.g. Moody et al., 2008).

Table 1: Typical spectrally integrated albedos of some land cover types.

Ecosystem	Albedo value (coarsely)
Grass	0.25
Forest (boreal)	0.10
Soil	0.10
Ocean	0.05
Snow	0.90

Here, albedo is the reflected part (from the surface of Earth) of SSR divided with the incoming part (the reflected and absorbed) of SSR. The albedo varies significantly over different surfaces, (e.g. Moody et al., 2007 summarises different ecosystems' albedos with the presence of snow on the ground) and often has a strong spectral dependency. For instance, typical spectrally integrated albedos of some land cover types are shown in the Table 1 (for more details, see the spectral albedo figure of different surfaces from http://profhorn.meteor.wisc.edu/wxwise/satmet/lesson3/surfacerad.html).

The water vapor content (WVC) describes the amount of the free water vapor in the atmosphere. The unit of AERONET derived WVC, which was used in this study is cm ($\sim g/cm^2$), and is defined as the atmospheric water vapor compressed to the surface with the standard temperature and pressure conditions. A very dry air have WVC less than 1 cm, whereas in a humid air the WVC values can reach 5cm or more.

The amount of solar radiation reached at the surface, for a given solar zenith angle, depends most strongly on the prevalent cloudiness. Therefore, in order to estimate the aerosol direct radiative effects by the solar surface radiation measurements, robust cloud-screening is required to select clear-sky measurements only. These clear-sky SSR measurements mainly depend on the following factors: SZA, WVC, AOD, AE, SSA, AP, A:

$$\mathrm{SSR} = \mathrm{SSR}(\theta, \tau, \mathrm{WVC}, \alpha, \omega, g, A, \mathrm{B}), \quad (8)$$

where B stands for other minor constituents such as ozone, nitrogen dioxide, etc. The effects of SZA, AOD, WVC, AE, SSA, AP, A and B in clear-sky SSR are described in the following:
- Solar Zenith Angle is the angle between the zenith and the Sun, being the most significant parameter, corresponding easily with a change of hundreds of

Wm^{-2} in SSR.
- AOD often decreases SSR with tens of Wm^{-2} and AE determines the spectral attenuation due to AOD.
- Increase of WVC decreases SSR due to the water vapor absorption (see Fig. 4) at particular absorption bands and the change in SSR is typically few percents between the dry and humid atmospheric state.
-SSA and AP can induce roughly an impact in SSR of the same magnitude or less than that by AOD (McComiskey et al., 2008). More specifically, the diffuse part of the solar radiation decreases with the increasing absorption, thus with the decreasing SSA.
Albedos contribution in SSR is often less than the previous factors, but over bright surfaces (at least in visible and near infrared), as deserts or glaciers, the solar irradiance is effectively reflected into the space, whereas over oceans, it is more effectively absorbed.

Fig. 6 represents schematically, how the solar radiation (and the Earth's thermal radiation) propagates in the atmosphere: a part of the solar radiation reaches more or less directly the Earth's surface, whereas some part of it is diffused due to the scattering processes with aerosols, air molecules and clouds. SSA and AP determine the aerosol contribution in the propagation of the solar radiation. For example, a larger AP corresponds to a stronger forward scattering by aerosols. Some portion the solar radiation is absorbed e.g. due to the water vapor and aerosols. For aerosols, the smaller is SSA the larger is the impact by aerosol absorption. The atmospheric components decrease SSR (cooling at the surface), whereas in the top of the atmosphere, there can be either cooling or warming, depending on the scattering and absorption processes.

For simplicity, the effect of the vertical profile of aerosols into SSR is not considered in the list above. Summarizing the above, the usual contributions of the mentioned parameters in SSR can be listed from the largest to the smallest: SZA $>$ AOD $>$ SSA $>$ AP $\approx A$ (e.g. McComiskey et al., 2008).

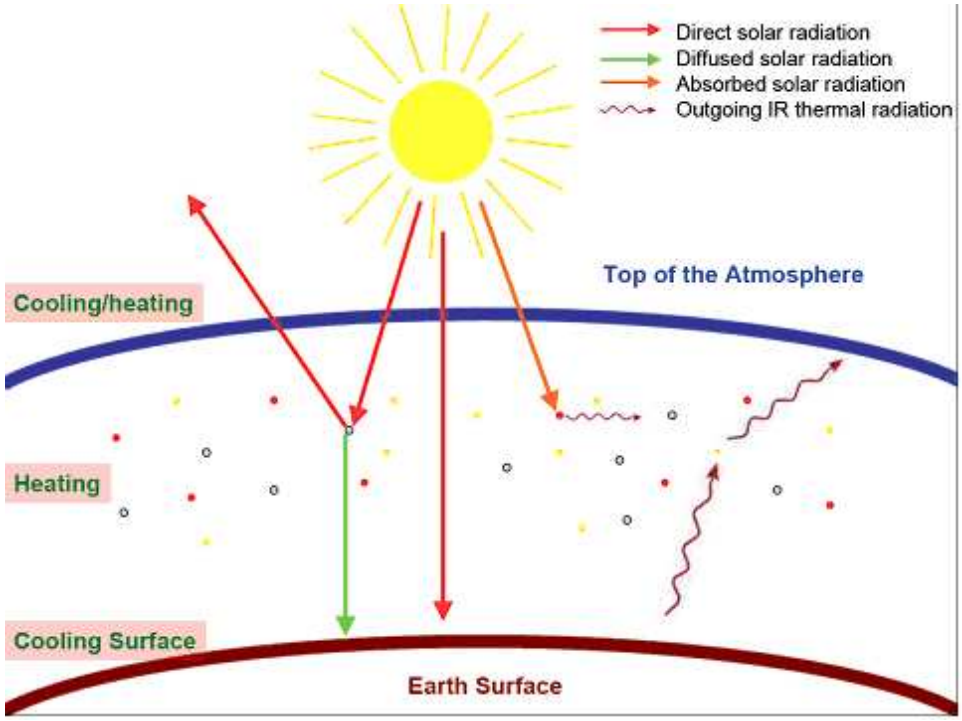

Figure 6: The solar radiation's propagation in the atmosphere. Also the Earth's emitted thermal radiation included. Although the contribution of the surface albedo is missing, some portion of the incoming radiation is reflected also from the surface. The figure is copied with a permission from http://www.isac.cnr.it/cimone/aerosol_properties.

3 Remote sensing of aerosols and radiation measurements

Remote sensing can be divided into active and passive detection. Active remote sensing creates its own detectable signal, whereas passive remote sensing relies on the solar (or Earth) radiation. Both detecting methods are established for both with the ground based and spacebased instruments.

By remote sensing measurements, information is obtained from an object without being in physical contact with it. Remote sensing can be divided into active and passive detection. Active remote sensing creates its own detectable signal, whereas passive relies on the solar (or Earth) radiation. Both detecting methods are established with the ground-based and satellite instruments.

The remote sensing instruments most commonly applied in aerosol research are ground-based sun photometers and Lidars (see Weitkamp, 2006 for Lidar-method) and space-based satellite instruments. Ground-based sun photometers offer essentially the ground-truth for AOD, while the obvious advantage of the satellite instruments is to provide a global coverage. On the other hand, satellite retrievals suffer some limitations, it is particularly difficult to retrieve AOD over highly reflecting surface with sufficient accuracy. Lenoble et al. (2013), gives a thorough introduction to the aerosol remote sensing measurements and retrievals. This Thesis exploited mainly ground-based passive remote sensing data (from AERONET, http://aeronet.gsfc.nasa.gov/).

3.1 Ground-based observations

The main source of ground-based remote sensing of aerosols is the Aerosol Robotic Network (AERONET). Fig. 7 shows the network's stations in the global map. AERONET is a ground-based remote-sensing global network of sun photometers (see Fig. 8) (Holben et al., 1998).

The sun photometer detects the solar radiation, directly from the Sun (sun measurements) or scattered from the atmosphere (sky measurements), with several wavelength bands (often with 340, 440, 500, 670, 870 and 1020 nm, depending on the network's invidual instruments' filters), having field of view 1.2^{o}. The instrument measures voltages induced by the incoming radiation at each wavelength band and this information together with the voltages corresponding the case without atmospheric extinction (i.e. intensity at the top of atmosphere). The latter needs to be estimated and is derived with the Langley method in AERONET(see the analogy with eq. 3). Measurements then provide indirectly the extinction caused by the atmospheric gases and aerosols (for cloud free cases). The aerosol contribution in the extinction is then determined by excluding the atmospheric gases (including the water vapor, which is detected with 940 nm band), finally providing AOD. Moreover, the extinction is divided into the scattering and absorption components using the inversion protocol with the sun and sky measurements. The inversion protocol for aerosol parameters from the network's observations is described in Dubovik and King (2000). An extension of the inversion, to account for particle non-sphericity, is described in Dubovik et al. (2006). AERONET provides e.g. AOD, AE and WVC from the direct sun measurements and SSA, AP and aerosol size distribution from the sky measurements (symmetrical measurements with varying almucantar and principal angles with respect to the Sun). See Holben et al. (1998) and Dubovik and King (2000) for the AERONET's

description. The uncertainty of the AERONET's AOD is 0.01-0.02 depending on the wavelength (Eck et al., 1999), and the uncertainty in WVC is 12 % (Holben et al., 1998). However, the uncertainty in AOD is considered being independent of the aerosol load (thus AOD), while the uncertainty in the other products (e.g. SSA and AP) does depend on AOD. For large enough values (AOD 440 nm > 0.4), the uncertainty in SSA is 0.03 (Dubovik et al., 2000). SSA and AP are problematic to retrieve with a good accuracy, if AOD and, thus the signal to noise ratio, is small. Therefore SSA and AP are accurate only if AOD is sufficiently large, limiting the amount of quality measurements of SSA and AP (example shown by Li et al., 2015(a)).

Figure 7: The Aerosol Robotic Network's stations in year 2016.

3.2 Satellite based observations

Aerosols are detected remotely also from satellites, mainly with so-called polar orbiting satellites (e.g. Stephens et al., 2002), but also with geostationary satellites (e.g. Laszloa et al., 2008). Polar orbiting satellites circulate the Earth between the poles while they at the same time move also in the latitudinal direction. Geostationary satellites circulate the Earth with the same angular velocity as the Earth circulates, and they are following the same view from the Earth with the larger distance (36 000 km compared with 700-800 km as for many polar orbiting satellites). The passive satellite instruments detect the reflected solar radiance with certain wavelength bands. For aerosol

Figure 8: The sun photometer measuring on the roof of Finnish Meteorological Institute main building, Helsinki, Finland.

retrievals cloud-free conditions are required, and the reflectivity has to be be divided into the components from atmosphere and from the surface, resulting finally in the estimate of aerosol contribution in the satellite-measured back-scattered radiance (see Mielonen, 2010 and Sundström, 2014). The active satellite instruments differ from the passive instruments by creating their own signal to detect after reflections from aerosols and the surface. Also a crucial difference is that the active instruments detect only a narrow vertical path (not wide swaths as many passive satellite instruments. Mielonen (2010) and Sundström (2014) describe satellite based instrumentations. For example, Cloud-Aerosol Lidar with Orthogonal Polarization (CALIOP) (http://www-calipso.larc.nasa.gov) emits and detects two perpendicular linearly polarized spectral radiation beams, giving the aerosol (and cloud) vertical profile and depolarization of aerosols, indicating aerosol shapes. Moreover, AOD, radiation and surface albedo are routinely detected from satellites, giving highly important information, e.g. Moderate Resolution Imaging Spectroradiometer (MODIS) (https://modis.gsfc.nasa.gov) instrument aboard satellites provides AOD and albedo, and Clouds and the Earth's Radiant Energy Sys-

tem (CERES) (https://ceres.larc.nasa.gov/) detects solar (reflected) and Earth (emitted) radiation.

3.3 Solar surface radiation (SSR) observations

SSR is mainly measured by pyranometer instruments. Pyranometer measurements are obtained with the thermopile method, where the temperature difference between the Sun exposed and shadowed parts of the instrument generates a voltage being linearly proportional with SSR (see e.g. http://www.kippzonen.com/ProductGroup/3/Pyranometers for more details, including also other pyranometer methods detecting SSR). The pyranometer typically covers the wavelength range from 300 nm to 2800 nm covering almost totally the SSR spectrum (see Fig. 4), with 180^o field of view angle, and the sample frequency is 1-2 seconds and every 1-2 minutes the average SSR are stored with the standard deviation. The pyranometers measurements have to be inverted to SSR with a known source of irradiance, providing possibility for the calibration. The pyranometers accuracy is ± 2 % (SolRadNet, http://solrad-net.gsfc.nasa.gov/). E.g. Solar Radiation Network (SolRadNet) and Baseline Surface Radiation Network (BSRN, http://www.bsrn.awi.de/) provide SSR measurements, but the number of stations is significantly less than of the AERONET's stations. Some of the pyranometer stations have, however, long time series, even more than hundred years (Lindfors et al., 2013). Furthermore, even though the pyranometer SSR measurements are rather accurate, still the cloud screening is a problematic task to select clear-sky measurements.

4 Overview of key results

4.1 The retrieval of AOD from SSR measurements with a nonlinear regression method, a radiative transfer code and machine learning algorithms

Paper I was motivated by Kudo et al., (2011) and Lindfors et al., (2013), where AODs are estimated with SSR measurements using the radiative transfer modeling. In **Paper I** the main goal was to assess, if applying sophisticated machine learning methods to observed data are able to produce better AOD estimates than those based on radiative transfer modeling. The approach utilizing radiative transfer modeling requires an assumption of the aerosol type, thus single scattering albedo, asymmetry parameter and spectral dependence in the extinction. However, in reality there is variability in time not only in the aerosol type, but also in the co-variability of aerosol properties and WVC, for instance. Therefore, it would provide a significant improvement if the machine learning methods, which do not need to assume aerosol type, would be able to implicitly find and account for this variability.

The SSR data were collected from Thessaloniki (Lindfors et al., 2013 describes the data and the station) and for our analysis we selected clear-sky measurements only. We included four machine learning algorithms, a regression method and a look-up table (LUT) based approach. The machine learning algorithms are random forest (RF), gaussian process (GP), neural network (NN) and support vector machine (SVM).

NR is a multivariate regression method, which allows nonlinear behaviour between inputs and an output. We tested different analytical functions and selected the best one for this purpose (see **Paper I**). RF is a nonlinear regression based on decision trees. The randomized training constructs trees, where variables are classified randomly at each node of trees, providing an ensemble of trained binary trees for the estimation data set. NN consists of neuron layers: an input layer, hidden layers and an output layer. Interconnected neurons with numeric weights are tuned in the training using multiple neural networks. SVM (in this study the standard SVM regression) finds a function that maximizes the mapped gap between the outputs in the training, and then the estimation data are mapped into the same space being classified different sides of the gap. We used a nonlinear classification and high-dimensional spaces for the classification gaps. GP treats inputs and an output as Gaussian random variables and constructs a model derived with conditional probability distributions. Again, multiple GP models were used in this study. For more details

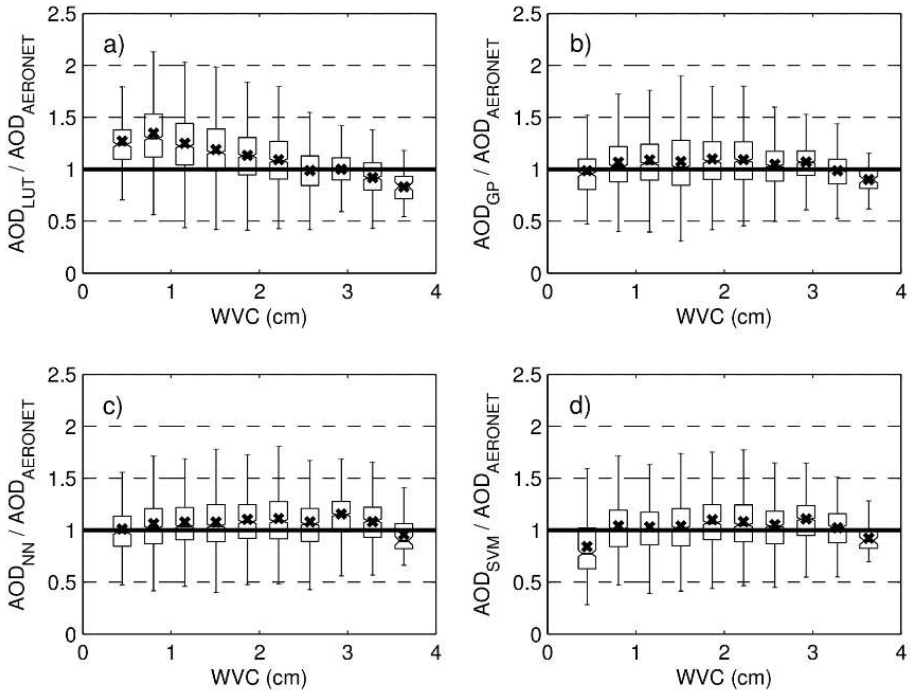

Figure 9: Predicted AOD divided by observed (AERONET) AOD for the methods of a) LUT (look-up table), b) GP (gaussian process), c) NN (neural network) and d) SVM (support vector machine) as functions of the observed water vapor content (WVC). The crosses indicate the means for the sub-groups, the limits of the boxes are 25 % (the lowest edges for of the boxes), 50 % (the middle vertical lines) and 75 % (the highest edges) of the data, and the lines represent 1.5 times the standard deviation.

about the machine learning methods, see the **Paper I** descriptions and the references.

We used more recent data (2009-2014) for the teaching and older data (2004-2008) for the estimation/validation. LUT contained the best information of the station's aerosol type (based on the AERONET sky measurements, see Lindfors et al., 2013). The AERONET sun measurements of AODs, collocated with SSR measurements, were set as a reference. Fig. 9 shows the performance of LUT, GP, NN and SVM compared with the AERONET-measured AODs as a function of the measured WVC. LUT-based AOD estimates tend to overesti-

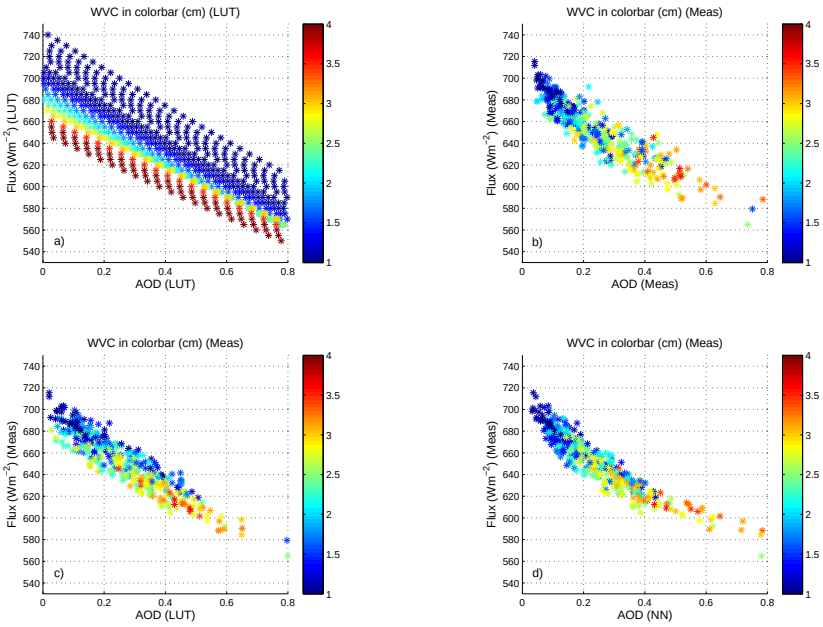

Figure 10: Solar surface radiation (SSR, F^{aer}) as a function of aerosol optical depth (AOD) for different values of water vapor column (WVC) for a fixed solar zenith angle (48.50°-51.50°) for a) look-up table (LUT) and b) measurements (Meas). The predicted AODs for c) LUT and d) neural network (NN) corresponding the same SSR, WVC and SZA.

mate AOD for the cases of small WVC and underestimate for the large WVC, which pattern is missing in the estimates by the the other methods.

Fig. 10b shows collocated AOD, WVC, and SSR. SSR measurements were collected from a narrow SZA range from 48.5 to 51.5 degrees. They were then normalized by a cosine rule (see Fig. 5) to better correspond to a fixed angle of 50 degrees. Moreover, since the measurements were from different seasons of the year, an Earth-Sun distance (e.g. the International Astronomical Union, www.iau.org/) correction was carried out, in order to make all the measurements corresponding to the conditions of 1st January. Evidently the patterns between a) and b) are different, in overall an increase in the measured AOD is accompanied by an increase in WVC. However, the pattern in LUT is necessarily very different, since it has been structured using a fixed aerosol model. For

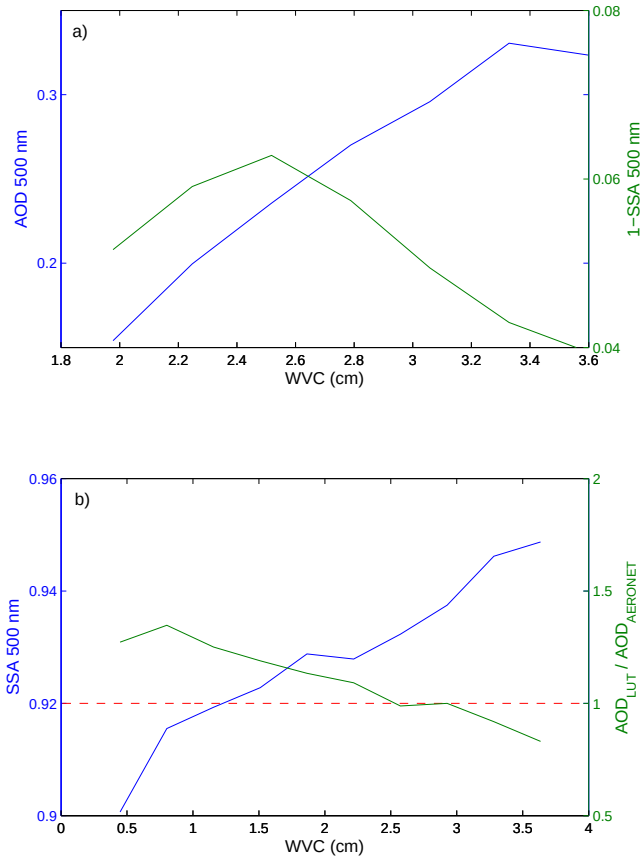

Figure 11: a) Aerosol optical depth (AOD), water vapor column (WVC) and 1-SSA at 670 nm from the AERONET inversion sky data. b) SSA at 500 nm, WVC and the LUT's predicted AOD divided with the observational AOD (AERONET), with the red line fixed to SSA (500 nm) = 0.92 (as in LUT).

instance, for a given SSR, the absorption by an increase in WVC must be compensated by a decrease in AOD (Fig. 10a). In the lower sub-figures of Fig. 10 the estimated AODs are shown for c) LUT and d) NN corresponding to these same measurements of SSR, WVC and SZA (Fig. 10b). The AOD vs. WVC structure by NN resembles most closely that by the measurements. LUT-based

method produces AOD vs. WVC dependence for a given SSR, following the pattern illustrated by the Fig. 10a; however this pattern does not exist in the measurements. Thus, in the actual measurements there obviously need to be some other co-variabilities between aerosols and atmospheric conditions that influence the measured surface solar radiation, which remain out of reach for the LUT with fixed aerosol model. Fig. 11 a) shows the SZA (58°-62°), SSR (420 Wm^{-2}-460 Wm^{-2}) and season (June-August) limited average values of AOD, WVC and 1-SSA (AOD at 500 nm and SSA estimated to 550 nm from 440 nm and 670 nm measurements) from these Thessaloniki measurements. It turned out that this overall pattern of decreasing single scattering co-albedo (co-albedo is defined with 1-SSA), being dependent on increasing WVC explained mainly why LUT had WVC-dependent bias that the machine learning methods did not have. There is a compensating effect between the water vapor absorption and by the absorption by aerosols, indicated by the single scattering co-albedo, 1-SSA. However, the LUT-based method necessarily assumes a fixed SSA, which cannot account for these kind of co-variabilities and thus results in the WVC-dependent bias illustrated by Fig. 9.

In **Paper I**, we show the problem of LUT with respect of WVC, but the case could be a more straightforward to show if essentially the same amount of SSA-data (as SSR, SZA, WVC and AOD, the inputs and the output) were available. Then a similar figure as Fig. 9, but with SSA in the horizontal axis, could be represented, showing immediately the difference between LUT and the machine learning methods: the former has the fixed atmospheric state, limiting the AOD estimation, whereas the latter are free and still can provide the valid AOD estimation, with respect of SSA. Moreover, in general (for other data sets than in **Paper I**), all the eq. (8) parameters, excluding the input/output, are potential to vary significantly and change the AOD estimation, not only SSA (as in **Paper I**).

The main application to exploit surface solar radiation measurements in estimating AOD is to assess the historical aerosol loads also in past before the era of dedicated sun-photometers. However, it is likely that also the aerosol single scattering albedo has changed, for instance due to the historical emissions of mostly absorbing black carbon and mainly scattering sulfate aerosols. Therefore, it is a very significant characteristic of these machine learning methods that they do not need to rely on pre-scribed aerosol properties and particularly the fact that they seem to be able to take the variability in aerosol optical properties into account in their AOD estimation.

4.2 The SSR^0 extrapolation for the observational based ADRE with SSR measurements - the water vapor effect

The aim in **Paper II** was to estimate the ADRE with SSR and AOD measurements using the regression fitting method. The key question is how to estimate the surface solar radiation accurately in conditions without aerosols, SSR^0. This becomes then necessarily an extrapolation problem, from the range covered by the AOD measurements to the hypothetical case of zero aerosols. We used the method introduced by Satheesh and Ramanathan, (2000), which extrapolates SSR^0 with a linear fit, as shown in Fig. 12. We also included nonlinear fit, an exponential decay, which was considered to be physically more representative than the linear fit due to e.g. the aerosol multiple scattering. The linear fit has been used already in many papers to derive observational ADRE (e.g., Kaufman et al., 2002; Bush and Valero, 2002, 2003; Dumka et al., 2006; Roger et al., 2006; di Sarra et al., 2008; Garcia et al., 2009; Satheesh et al., 2010). The nonlinear fit was motivated by few studies (e.g. Conant et al. 2003, Markowicz et al. 2008 and Kudo et al. 2010) implying that SSR attenuates nonlinearly with respect to AOD. In order to study the regression method with as wide range of aerosol as possible, all the available AERONET sites were taken into the analysis providing a substantial amount of stations from different regions on the Earth (see Fig. 7). Moreover, the simulated SSR^0 using AERONET measurements gave us the reference values of SSR^0.

The nonlinear fit was expected to give a better estimation of ADRE than the linear one (e.g. Conant et al. 2003, Markowicz et al. 2008 and Kudo et al. 2010). We found that, contrary to the expectation, in most cases the linear fit gave better results than the nonlinear fit. Fig. 12 shows a comparison of the methods for one station Kanpur, as an example, where AOD is in the horizontal axis and SSR in the vertical axis. The surface solar radiation with and without aerosols are represented with plusses and circles respectively. The SSRs rely on the radiative transfer coding including e.g. aerosols, air molecules, SZA, albedo and water vapor. In the SSR^0s simulations the aerosols are excluded in the simulations, otherwise corresponding to the same conditions as in the SSRs. The aim of the fits is to estimate SSR^0s as close the truth as possible relying the SSRs, while WVC and the other, atmospheric and aerosols', conditions are varying freely, expect SZA, which is limited. But, seemingly the nonlinear and linear fits provide significantly different SSR^0s, the bar on the vertical axis represents the mean value of the simulated SSR^0.

Nevertheless it is the linear fit that results in somewhat more accurate estimate for the average SSR^0, and thus for the ADRE. The main reason for this behav-

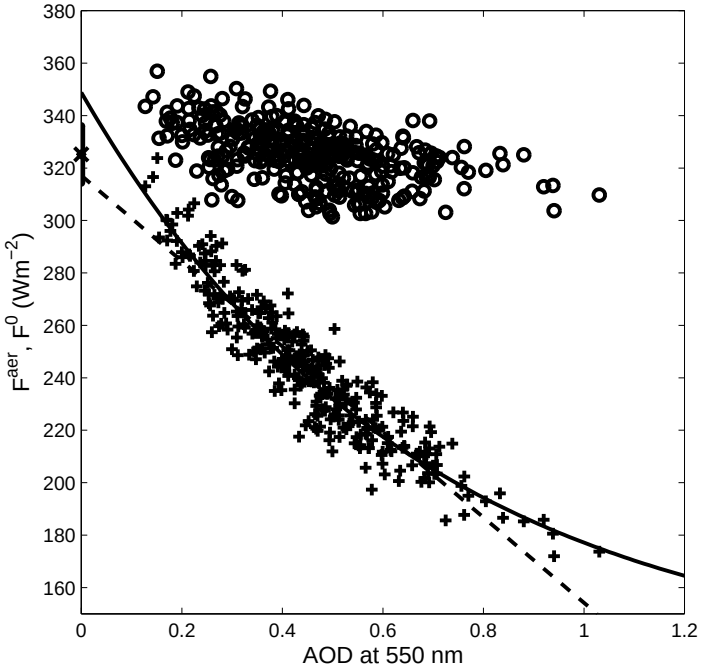

Figure 12: Solar surface radiation with aerosols, F^{aer} (plusses) and without aerosols F^0 (circles) with AOD at 550 nm. The data are from Kanpur, March-May season with SZA = 69°±1.5°. The bar on the vertical axis is the average of the F^0 values (all circles). The nonlinear (x_1 $\exp^{-x_2 \mathtt{AOD}}+x_3$, where x_1, x_2 and x_3 are constants) and linear (z_1 AOD+z_2, where z_1 and z_2 are constants) fits included.

ior is illustrated by the pattern of SSR^0 against AOD, i.e. by the circles. The negative correlation between SSR^0 and AOD is indirectly caused mainly by a positive correlation of AOD with WVC due to humid air masses with large aerosol concentration. With increasing AOD and WVC, the WVC dims an increasing fraction of the radiation intensity - resulting in a smaller SSR^0. In other words, while WVC increases with AOD, then SSR^0 decreases. Therefore, the feature of the linear fit to provide a smaller SSR^0 fortuitously results in better SSR^0 estimate. When the measurements contain co-variability between AOD and WVC that, in turn, causes a systematic effect in the average SSR^0 to decrease. The WVC's effect on the analysis will be illustrated later, in Fig. 14. Figure 13 shows the WVC and AOD correlation coefficient at all the sites

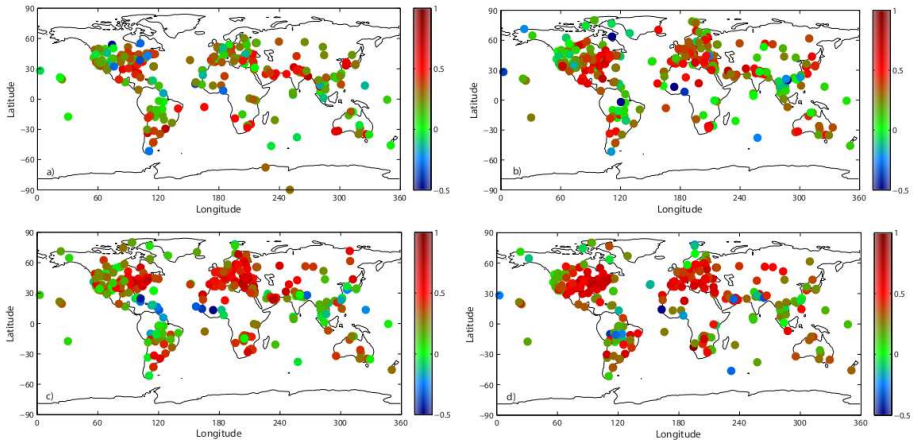

Figure 13: Geographical distribution of the AOD and WVC correlation coefficient, at all AERONET stations considered in this study for a) December-February, b) March-May, c) June-August and d) September-November (all available years).

available from AERONET. For a majority of locations AOD and WVC have a positive correlation, and for these cases the linear method gives somewhat better results in general than the nonlinear approach. There are specific regions of strong negative WVC and AOD correlation, most notably in the Saharan dust outflow region, where the opposite takes place and nonlinear approach results in better estimate for ADRE.

4.3 The overall influence induced by the co-variability between AOD and WVC in measurement data sets

Common finding in **Paper I** and **Paper II** is related to the correlation in the data sets between AOD and some other variable affecting SSR, most strongly WVC and SSA. In **Paper I**, it was shown that in Thessaloniki the increasing AOD values are typically accompanied by increasing WVC, as well as by increasing SSA. Then it was demonstrated that these correlations essentially caused the look-up table based method, which assumes fixed aerosol type, to produce systematic WVC dependent bias. On the other hand, in **Paper II** this very same relationship between AOD and WVC within the selected data set was the reason for the systematic bias in the estimated SSR^0. In case of positive correlation between AOD and WVC, which is clearly more typical based

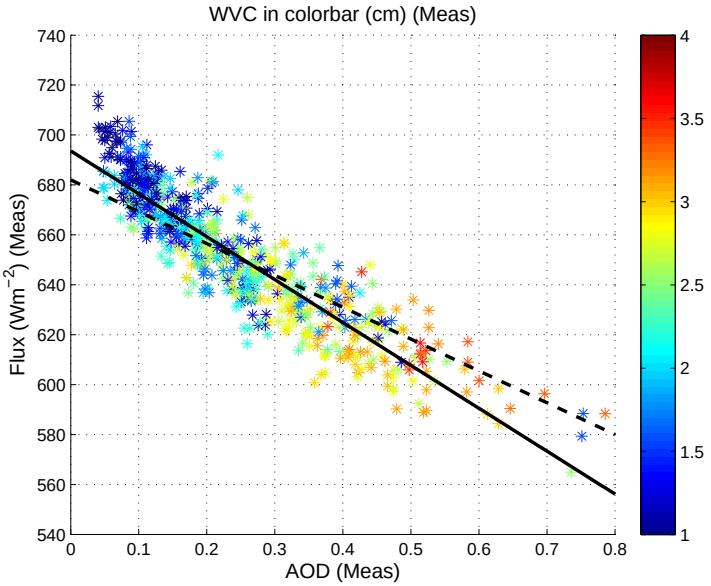

Figure 14: Measured AOD in the horizontal axis, SSR in the vertical axis and WVC in the colorbar (not shown: SSA increases with AOD also, as WVC in the colorbar). The solid line represents the regression fit into the measurements data, whereas the dashed line is fitted in the WVC-normalized SSR. In the normalization, the SSRs are divided with the ratio of SSR^0s/$SSR^0{}_{\texttt{average WVC}}$, where $SSR^0{}_{\texttt{average WVC}}$ is the SSR^0 corresponding to the average WVC (see the crosspoint of the lines) and SSR^0s corresponds with the SSRs (with the same WVCs). The SSR's dependence on WVC is assumed to be only contributed by the water vapor absorption, not e.g. due to the aerosol hygroscopicity (the fraction between the aerosol hygroscopicity and the water vapor absorption can be estimated indirectly with the aerosol optical property and spectral-SSR measurements).

on our analysis of all AERONET sites, this results in overestimation of SSR^0. The solid line in Fig. 14 illustrates this, through a comparison with the dashed line corresponding to the case if WVC within the data set was constant. With the help of this same figure, one can also illustrate the influence of AOD and WVC (and AOD and SSA) correlation in the WVC-dependent systematic bias in LUT-retrieved AOD. Selecting a constant value of SSR from y-axis, say 610 Wm^{-2}, the measurement spread indicates increasing WVC when one moves from smaller to larger AOD. This pattern is exactly opposite to the structure

that the LUT-approach needs to assume regardless of the fixed aerosol model (see Figure 10a). This is essentially what is behind the WVC-dependent bias seen in the AOD-estimates produced by LUT.

4.4 The intercomparison of shortwave radiative transfer schemes with global aerosol models

Paper III shows the performance of 31 global models, for deriving ADRE, with given atmospheric schemes including fixed aerosol types. Thus, e.g. AOD, SSA and WVC are given, whereas SSR and SSR^0 (also TOA irradiance) are simulated with the models. The study involves two high-spectral resolution line-by-line models (LBL) (e.g. Edwards, 1992), giving a benchmark for the rest of the 29 models. In addition, the models can be divided into multi-stream (more than two streams) and two-stream approximations of the radiative transfer modeling. In the two-stream approximation, radiation propagates only two discrete directions following a radiative transfer equation, whereas the multiple-stream allows the multiple scattering. **Paper III** established the protocol given in Halthore et al. (2005), where the following atmospheric schemes are considered: 1) pure Rayleigh scattering, where aerosols are removed in the simulations and only scattering and absorption by gases e.g. nitrogen, oxygen, argon, ozone etc., is included, 2) a purely scattering aerosol type (SSA=1, which is a constant as a function of the wavelength) and 3) a strongly absorbing aerosol type (SSA=0.8). Ozone and A (and other parameters as a function of the altitude) are prescribed and the model simulations are done for SZA=30° and SZA=75° (see Table 2 from **Paper III**). For all the schemes, irradiances are considered, and in addition, for the scheme 2 and 3, ADREs are determined based on the irradiance calculations.

The model results show (for the schemes 1, 2, 3), that 1) the Rayleigh scattering scheme produced up to 6 % error for the models, the largest model deviation being with large SZA. Table 3 of **Paper III** summarizes the distributions within the models for direct and diffuse, shortwave (UV-VIS, ultraviolet-visible) and longwave (near-IR, near-infrared), and surface and TOA irradiances (surface irradiance represents SSR^0). The near-IR irradiance produces the largest distribution within the models, whereas the direct and the diffuse (surface and TOA) are in the better agreement. The deviation is large especially in the near-IR, presumably due to representations in the water vapor absorption. Moreover, the partition of the irradiance into its direct and diffuse components also produces a significant deviation, and this is probably caused in treatments of the ozone absorption.

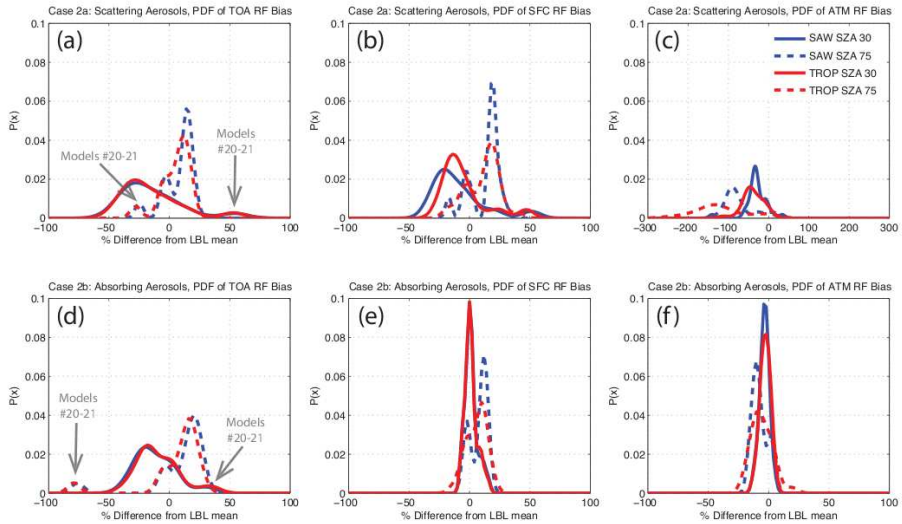

Figure 15: The probality density functions P(x) for scattering aerosol type a) at the top of the atmosphere (TOA), b) at the surface (SFC) and c) in the atmosphere. Absorbing aerosol type d) at the top of the atmosphere (TOA), e) at the surface (SFC) and f) in the atmosphere. Blue indicates subarctic winter (SAW) and red tropical (TROP) atmospheres (see Randles et al., 2013 for details). The continuous line is for solar zenith angle 30° and the dashed line for 75°. The P(x) difference is calculated from the line-by-line models' (LBL) mean value for the non-LBL results. Notice that subfigure c) has a different horizontal scale than the other subfigures.

In 2) and 3) the total scattering aerosol scheme produces the largest error for the smaller SZA (30°) which decreases for the larger SZA (75°). See Appendix Tables A3 and A4 of **Paper III**, which contain the result for the scheme 2 and 3. The irradiances determine ADRE and Fig. 15 summarizes the ADRE results for simulations 2) and 3), showing the probability density functions for the models (some of them are highlighted) compared with LBL. The sub figures hold for different schemes and SZA. The probability density functions in Fig. 15 e) and Fig. 15 f) are much narrower than in Fig. 15 c) (see the changed horizontal scale). Thus, the model bias depends on SZA, especially for the scattering-only aerosol type, whereas the strong absorbing aerosol type produces a smaller dependency with SZA. As the major result of **Paper III**,

the strong absorbing aerosol scheme (the scheme 3) did not produce such a large error as the purely scattering aerosol scheme (2), although it is still in the same order of the magnitude.

This result is indicatively due to problems in the aerosol multiple scattering, because the multi-stream models manage the purely scattering aerosol scheme better. But the computational cost will be decreased in the future and one may calculate more readily with the more sophisticated multi-stream method. The aerosol schemes (2 and 3) provide a 10 %-20 % error, and if AOD and SSA were simulated (in **Paper III** they were given) with the models independently, the deviations would have been even larger. Furthermore, the difference between models for the scheme 2 and 3 are essentially the same as in the previous studies mentioned in **Paper III**.

4.5 The change in ADRE due to the diurnal changes in AOD

The aim of **Paper IV** was to study how the AOD's diurnal variability influences the estimate of ADRE, and if it is suitable to use a single overpass time only from satellite based AOD instead of more frequent AOD from local stations. Currently, AERONET has less than 800 stations, with most of the Earth being without valid AOD surface measurements (see Fig. 7). Satellite based AOD measurements, however, cover the whole Earth, but with a lower temporal coverage.

All the AERONET sites, with varying aerosol and albedo conditions, are included in this study (see Fig. 7). With the radiative transfer modeling, ADRE at TOA is calculated assuming either the diurnally varying or the daily averaged ground-based AOD. The data criteria and the radiative transfer model are mentioned in **Paper IV**. Fig. 16 shows the difference between the hourly and daily averaged values for AOD (red), and the difference in ADRE simulated with the hourly averaged AOD and the daily averaged AOD (blue) for the four stations. The largest difference in ADRE exists, if the extremum (minimum or maximum) AOD, is reached during local noon (Fig. 16 c and d). Otherwise, even if AOD has a significant diurnal change (without the extremum during local noon), the ADREs for local hours are compensating each other to large extent (Fig. 16 a and b). For individual sites and seasons there can be significant difference between the diurnally varying and the daily averaged AOD derived ADRE, but considering all the results, the difference is small being often within ± 5 % (see Fig. 5 and 6, and Table 1, in **Paper IV**).

Finally, ADRE TOA based on satellite overpass AOD (represents also the daily averaged AOD), instead of the ground-based AOD, is compared with the ADRE TOA calculated with the diurnally averaged AOD. This comparison shows, that in general the difference is small, almost always within ±10 %. Thus, the satellite based AOD derived ADRE represents essentially the same as the diurnally varying AOD derived ADRE TOA. The main conclusion of **Paper IV** is, that even a significant diurnal variation of AOD does not induce a strong change in ADRE and also that the satellite based AOD is suitable for the ADRE calculations.

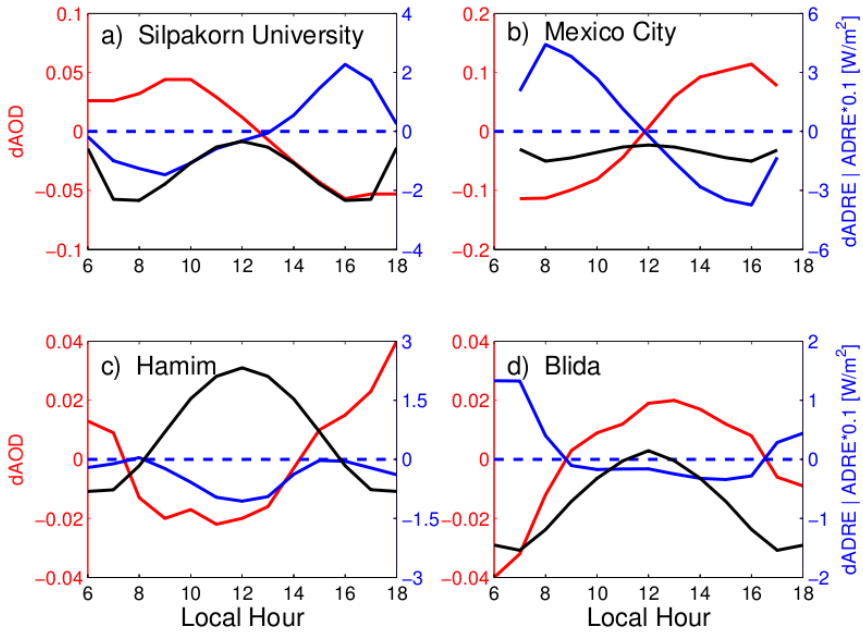

Figure 16: Hourly averaged AOD minus its daily average value (red, dAOD, left axis) and the difference in ADRE simulated by the hourly averaged AOD and the daily averaged AOD (blue, dADRE, right axis). The true ADRE with true diurnal AOD cycle (black, right axis). Notice that ADRE is multiplied with 0.1 to fit into the same scale. a) Silpakorn University, Thailand (March-April-May), b) Mexico City, Mexico (December-January-February), c) Hamim, United Arab Emirates (June-July-August) and d) Blida, Algeria (June-July-August).

5 Conclusions and view to the future

Aerosol remote sensing and solar radiation measurements provide an invaluable dataset for studying the contribution of atmospheric aerosols in radiation propagation. The main focus of this study was to investigate how the correlation between the amount of water vapor (and single scattering albedo) and the aerosol amount affect the aerosol direct radiative effect.

The first objective was to assess, whether it is possible to estimate aerosol optical depth reliably with surface solar radiation measurements using machine learning algorithms and how well they perform if compared with a loo-up table (LUT) based on radiative transfer modeling. **Paper I** shows that the AOD estimation is possible and that the machine learning algorithms are able to estimate AOD better than LUT. Moreover, the most significant finding is the LUT's systematic bias with respect to WVC, while the machine learning algorithms did not produce such a systematic bias. The aerosol scattering efficiency is enhanced with increasing WVC, which explains the result, as **Paper I** highlights. Furthermore, it was shown in **Paper II** that this co-variability of AOD and WVC can have an influence in ADRE estimates, using ground-based measurements of SSR and AOD. This relationship was the reason why linear regression extrapolates SSR^0 better than the more physical nonlinear method, against expectation. Thus, in the second objective, the role of atmospheric water vapor is crucial for ADRE and this complicates the extrapolation method application.

The third objective considered the performance of an ensemble of many global models (**Paper III**), the solar shortwave radiation (at the surface, in the atmosphere and at the top of the atmosphere) for three schemes: 1) the aerosol free (only the gaseous atmosphere), 2) the total scattering aerosols and 3) the strongly absorbing aerosols. As a conclusion: the scheme 1) produced up to 6 % error by the models, while the schemes 2) and 3) produced 10 %-20 %. The result is generally the same than the previous similar inter-comparisons (e.g. Schulz et al., 2006).

The fourth objective was to assess how does a diurnal variability in AOD influence ADRE estimates. Although ground-based AOD measurements have a large temporal frequency, they still are very limited spatially, whereas satellites cover most of the Earth's surface. The drawback for satellite AOD is its limited temporal resolution. In **Paper IV** we found that, even a significant AOD's diurnal variation did not typically induce a strong change in ADRE.

As a view to the future, **Paper I** opens possibility for a new analysis, where AOD can be estimated (with cloud screened temporally homogeneous SSR-data) for a time period reaching at least decades, possibly even for more than a hundred years, with the robust machine learning methods.

This analysis could bring new information also about the aerosols' contribution in the climate change. Moreover, the author encourages to solve the SSR0

estimation problem using new methods, e.g. machine learning algorithms mentioned in this Thesis, for instance with a many dimensional analysis considering all the variables free (not fixed as e.g. in Fig. 12). An accurate measurement based SSR^0 is crucial before the case when the atmospheric state is so well monitored that SSR, and SSR^0, can be simulated with a great accuracy, and without an offset compared with SSR measurements.

Bibliography

Aalto P., K. Hmeri, P. Paatero, M. Kulmala, T. Bellander, N. Berglind, L. Bouso, G. Castano-Vinyals, J. Sunyer, G. Cattani, A. Marconi, J. Cyrys, S. von Klot, A. Peters, K. Zetzsche, T. Lanki, J. Pekkanen, F. Nyberg, B. Sjvall, and F. Forastiere, Aerosol Particle Number Concentration Measurements in Five European Cities Using TSI-3022 Condensation Particle Counter over a Three-Year Period during Health Effects of Air Pollution on Susceptible Subpopulations, Journal of the Air & Waste Management Association, Vol. 55 , Iss. 8, doi:10.1080/10473289.2005.10464702, 2005.

Andrews, E., Sheridan P. J., Fiebig M., McComiskey A., Ogren J. A., Arnott P., Covert, D., Elleman R., Gasparini R., Collins D., Jonsson H., Schmid B. and Wang J., Comparison of methods for deriving aerosol asymmetry parameter, J. Geophys. Res., 111, D05S04, doi:10.1029/2004JD005734, 2006.

Bergstrom, R. W., Pilewskie, P., Russell, P. B., Redemann, J., Bond, T. C., Quinn, P. K., and Sierau, B.: Spectral absorption properties of atmospheric aerosols, Atmos. Chem. Phys., 7, 5937-5943, doi:10.5194/acp-7-5937-2007, 2007.

Bohren C. F. and Huffman D. R., Absorption and Scattering of Light by Small Particles, Wiley, 1983.

Bush, B. C. and Valero, F. P. J.: Spectral aerosol radiative forcing at the surface during the Indian Ocean Experiment (INDOEX), J. Geophys. Res., 107, 8003, doi:10.1029/2000JD000020, 2002.

Bush, B. C. and Valero, F. P. J.: Surface aerosol radiative forcing at Gosan during the ACE-Asia campaign, J. Geophys. Res., 108, 8660, doi:10.1029/2002JD003233, 2003.

Carmichael, G. R., Adhikary, B., Kulkarni, S., D'Allura, A., Tang, Y., Streets, D., Zhang, Q., Bond, T. C., Ramanathan, V., Jamroensan, A. and Marrapu, P., Asian Aerosols: Current and Year 2030 Distributions and Implications to Human Health and Regional Climate Change, Environ. Sci. Technol., 43, 15, 58115817, 2009.

Conant, W. C., Seinfeld, J. H., Wang, J., Carmichael, G. R., Tang, Y., Uno, I., Flatau, P. J., Markowicz, K. M., and Quinn, P. K.: A model for the radiative forcing during ACE-Asia derived from CIRPAS Twin Otter

and R/V Ronald H. Brown data and comparison with observations, J. Geophys. Res., 108, 8661, doi:10.1029/2002JD003260, 2003.

Dumka, U. C., Satheesh, S. K., Pant, P., Hegde, P., and Krishna Moorthy, K.: Surface changes in solar irradiance due to aerosols over central Himalayas, Geophys. Res. Lett., 33, L20809, doi:10.1029/2006GL027814, 2006.

Dubovik, O. and King, M. D.: A flexible inversion algorithm for retrieval of aerosol optical properties from Sun and sky radiance measurements, J. Geophys. Res., 105, 2067320696, doi:10.1029/2000JD900282, 2000.

Dubovik, O., Smirnov, A., Holben, B. N., King, M. D., Kaufman, Y. J., Eck, T. F., and Slutsker, I.: Accuracy assessments of aerosol optical properties retrieved from Aerosol Robotic Network (AERONET) Sun and sky radiance measurements, J. Geophys. Res., 105, 97919806, doi:10.1029/2000JD900040, 2000.

Dubovik, O., A. Sinyuk, T. Lapyonok, B.N. Holben, M. Mishchenko, P. Yang, T.F. Eck, H. Volten, O. Muoz, B. Veihelmann, W.J. van der Zande, J.-F. Leon, M. Sorokin, and I. Slutsker, Application of spheroid models to account for aerosol particle nonsphericity in remote sensing of desert dust. J. Geophys. Res., 111, D11208, doi:10.1029/2005JD006619, 2006.

Di Sarra, A., Pace, G., Meloni, D., De Silvestri, L., Piacentino, S., and Monteleone, F.: Surface shortwave radiative forcing of different aerosol types in the central Mediterranean, Geophys. Res. Lett., 35, L02714, doi:10.1029/2007GL032395, 2008.

Eck, T. F., Holben, B. N., Reid, J. S., Dubovik, O., Smirnov, A., ONeill, N. T., Slutsker, I., and Kinne, S.: Wavelength dependence of the optical depth of biomass burning, urban, and desert dust aerosols, J. Geophys. Res., 104, 3133331349, doi:10.1029/1999JD900923, 1999.

Edwards, D. P.: GENLN2: A general line-by-line atmospheric transmittance and radiance model. Technical Report NCAR/TN-367+STR, NCAR, P.O. Box 3000, Boulder, Colorado, 80307-3000, 147 pp., 1992.

Fang, Y., Naik, V., Horowitz, L. W., and Mauzerall, D. L.: Air pollution and associated human mortality: the role of air pollutant emissions, climate change and methane concentration increases from the preindustrial period to present, Atmos. Chem. Phys., 13, 1377-1394, doi:10.5194/acp-13-1377-2013, 2013.

Feynman R. P., Leighton R. B. and Sands M., The Feynman Lectures on Physics. Mainly Mechanics, Radiation, and Heat (Vol. 1). Addison-Wesley, Reading, 1963.

Garcia, O. E., Daz, A. M., Expsito, F. J., Daz, J. P., Redondas, A., and Sasaki, T.: Aerosol radiative forcing and forcing efficiency in the UVB for regions affected by Saharan and Asian Mineral Dust, J. Atmos. Sci., 66, 10331040, doi:10.1175/2008JAS2816.1, 2009.

Hallquist, M., Wenger, J. C., Baltensperger, U., Rudich, Y., Simpson, D., Claeys, M., Dommen, J., Donahue, N. M., George, C., Goldstein, A. H., Hamilton, J. F., Herrmann, H., Hoffmann, T., Iinuma, Y., Jang, M., Jenkin, M. E., Jimenez, J. L., Kiendler-Scharr, A., Maenhaut, W., McFiggans, G., Mentel, Th. F., Monod, A., Prvt, A. S. H., Seinfeld, J. H., Surratt, J. D., Szmigielski, R., and Wildt, J.: The formation, properties and impact of secondary organic aerosol: current and emerging issues, Atmos. Chem. Phys., 9, 5155-5236, doi:10.5194/acp-9-5155-2009, 2009.

Halthore, R. N., et al., Intercomparison of shortwave radiative transfer codes and measurements, J. Geophys. Res., 110, D11206, doi:10.1029/2004JD005293, 2005.

Haywood, J., and Boucher O., Estimates of the direct and indirect radiative forcing due to tropospheric aerosols: A review, Rev. Geophys., 38(4), 513543, doi:10.1029/1999RG000078, 2000.

Hecht E., Optics, 2nd Ed, Addison Wesley, 2002.

B. N. Holben, T. F. Eck, I. Slutsker, D. Tanre, J. P. Buis, A. Setzer, E. Vermote, J. A. Reagan, Y. J, Kaufman, T. Nakajima, F. Lavenu, I. Jankowiak and A. Smirnov, AERONET-A Federated Instrument Network and Data Archive for Aerosol Characterization, Remote Sens. Env. 66:1-16, 1998.

IPCC: Climate Change 2013, The Physical Science Basis. Contribution of Working Group I to the Fifth Assessment Report of the Intergovernmental Panel on Climate Change, edited by: Stocker, T. F., Qin, D., Plattner, G.-K., Tignor, M., Allen, S. K., Boschung, J., Nauels, A., Xia, Y., Bex, V., and Midgley, P. M., Cambridge University Press, Cambridge, United Kingdom and New York, NY, USA, 1535 pp., 2013.

Kasten F. and Young A. T., Revised optical air mass tables and approximation formula, Applied Optics 28: 47354738. Bibcode:1989ApOpt..28.4735K. doi:10.1364/AO.28.004735, 1989.

Kaufman, Y. J., Tanr, D., Holben, B. N., Mattoo, S., Remer, L. A., Eck, T. F., Vaughan, J., and Chatenet, B.: Aerosol radiative impact on spectral solar flux at the surface, derived from principal-plane sky measurements, J. Atmos. Sci., 59, 635646, doi:10.1175/1520-0469(2002)059¡0635:ARIOSS¿2.0.CO;2, 2002.

Kudo, R., Uchiyama, A., Yamazaki, A., Sakami, T., and Kobayashi, E.: From solar radiation measurements to optical properties: 19982008 trends in Japan, Geophys. Res. Lett., 37, L04805, doi:10.1029/2009GL041794, 2010.

Kudo, R., Uchiyama, A., Yamazaki, A., Sakami, T., and Ijima, O., Decadal changes in aerosol optical thickness and single scattering albedo estimated from ground-based broadband radiome- ters: A case study in Japan, J. Geophys. Res., 116, D03207, doi:10.1029/2010JD014911, 2011.

Kurucz, R. L., Synthetic infrared spectra, in Infrared Solar Physics, IAU Symp. 154, edited by D.M. Rabin and J.T. Jefferies, Kluwer, Acad., Norwell, MA, 1992.

Laszloa I., Cirenb P., Liub H., Kondraguntaa S., Tarpleya J. D., Goldberga M. D., Remote sensing of aerosol and radiation from geostationary satellites, Advances in Space Research, Volume 41, Issue 11, Pages 18821893, 2008.

Lenoble J., Remer L., and Tanre D., Aerosol remote sensing. Springer Science Business Media, 2013.

Li, S., Kahn, R., Chin, M., Garay, M. J., and Liu, Y., Improving satellite-retrieved aerosol microphysical properties using GOCART data, Atmos. Meas. Tech., 8, 1157-1171, doi:10.5194/amt-8-1157-2015, 2015 (a).

Li, J., Carlson, B. E. and Lacis, A. A., Using single-scattering albedo spectral curvature to characterize East Asian aerosol mixtures, Journal of Geophysical Research: Atmospheres 120 (5), 20372052 , 2015 (b).

Lindfors, A. V., Kouremeti, N., Arola, A., Kazadzis, S., Bais, A. F., and Laaksonen, A.: Effective aerosol optical depth from pyranometer measurements of surface solar radiation (global radiation) at Thessaloniki, Greece, Atmos. Chem. Phys., 13, 3733-3741, doi:10.5194/acp-13-3733-2013, 2013.

Liou, K. N., *An Introduction to Atmospheric Radiation*, 2nd ed., Academic Press, San Diego, USA, 2002.

Loeb, N. G. and Su, W.: Direct aerosol radiative forcing uncertainty based on a radiative perturbation analysis, J. Climate, 23, 52885293, doi:10.1175/2010JCLI3543.1, 2010.

Lohmann, U. and Feichter, J., Global indirect aerosol effects: a review, Atmos. Chem. Phys., 5, 715-737, doi:10.5194/acp-5-715-2005, 2005.

Löndahl, J., Swietlicki, E., Lindgren, E., and Loft, S.: Aerosol exposure versus aerosol cooling of climate: what is the optimal emission reduction strategy for human health?, Atmos. Chem. Phys., 10, 9441-9449, doi:10.5194/acp-10-9441-2010, 2010.

Mahowald N., D. S. Ward, S. Kloster, M. G. Flanner, C. L. Heald, N. G. Heavens, P. G. Hess, J.-F. Lamarque, and P. Y. Chuang, Aerosol Impacts on Climate and Biogeochemistry, Annual Review of Environment and Resources, Vol. 36: 45 -74, 2011.

Markowicz K. M., P. J. Flatau, J. Remiszewska, M. Witek, E. A. Reid, J. S. Reid, A. Bucholtz, and B. Holben, Observations and Modeling of the Surface Aerosol Radiative Forcing during UAE^2, American Meteorology Society, DOI: 10.1175/2007JAS2555.1, 2008.

Mayer B. and Kylling, A., Technical note: The LibRadtran software package for radiative transfer calculations - description and examples of use, Atmos. Chem. Phys., 5, 1855-1877, doi:10.5194/acp-5-1855-2005, 2005.

McComiskey A., Schwartz S. E., Schmid B., Guan H., Lewis E. R., Ricchiazzi P. and Ogren J. A., Direct aerosol forcing: Calculation from observables and sensitivities to inputs, Journal of Geophysical Research, Volume 113, Issue D9, 10.1029/2007JD009170, 2008.

Mielonen T., Evaluation and application of passive and active optical remote sensing methods for the measurement of atmospheric aerosol properties, Finnish Meteorological Institute Contributions No. 85, 2010.

Mishchenko, Michael I., Electromagnetic scattering by particles and particle groups : an introduction, NASA Goddard Institute of Space Studies, Cambridge, University Press, 2014.

Modest, Michael F. Radiative heat transfer. Academic press, 2013.

Moody E. G., King M. D., Schaaf C. B., Hall D. K. and Platnick S., Northern Hemisphere five-year average (20002004) spectral albedos of surfaces in the presence of snow: Statistics computed from Terra MODIS land products, Remote Sensing of Environment 111, 337-345, 2007.

Moody E., King M., Schaaf C., Platnick S., MODIS-Derived Spatially Complete Surface Albedo Products: Spatial and Temporal Pixel Distribution and Zonal Averages., J. APPL METEOROL CLIMATOL.,47, 11, 2879-2894, 2008.

Myhre, G., Consistency between satellite-derived and modeled estimates of the direct aerosol effect, Science, 325, 187190, doi:10.1126/science.1174461, 2009.

Remer L. A., Kleidman R. G., Levy R. C., Kaufman Y. J., Tanr D., Mattoo S., Martins J. V., Ichoku C., Koren I., Yu H. and Holben B. N., Global aerosol climatology from the MODIS satellite sensors, Journal of Geophysical Research: Atmospheres 113 (D14), DOI: 10.1029/2007JD009661, 2008.

Roger, J. C., Mallet, M., Dubuisson, P., Cachier, H., Vermote, E., Dubovik, O., and Despiau, S.: A synergetic approach for estimat- ing the local direct aerosol forcing: application to an urban zone during the Exprince sur Site pour Contraindre les Modles de Pollution et de Transport dEmission (ESCOMPTE) experiment, J. Geophys. Res., 111, D13208, doi:10.1029/2005JD006361, 2006.

Samset, B. H., Myhre, G., Schulz, M., Balkanski, Y., Bauer, S., Berntsen, T. K., Bian, H., Bellouin, N., Diehl, T., Easter, R. C., Ghan, S. J., Iversen, T., Kinne, S., Kirkevg, A., Lamarque, J.-F., Lin, G., Liu, X., Penner, J. E., Seland, ., Skeie, R. B., Stier, P., Takemura, T., Tsigaridis, K., and Zhang, K.: Black carbon vertical profiles strongly affect its radiative forcing uncertainty, Atmos. Chem. Phys., 13, 2423-2434, doi:10.5194/acp-13-2423-2013, 2013.

Satheesh S. K. and V. Ramanathan, Large differences in tropical aerosol forcing at the top of the atmosphere and Earth's surface, Nature, 405, 60-63, doi:10.1038/35011039, 2000.

Satheesh, S. K., Vinoj, V., and Krishna Moorthy, K.: Radiative effects of aerosols at an urban location in southern India: Observations vs. model, Atmos. Environ., 44, 52955304, doi:10.1016/j.atmosenv.2010.07.020, 2010.

Schulz, M., Textor, C., Kinne, S., Balkanski, Y., Bauer, S., Berntsen, T., Berglen, T., Boucher, O., Dentener, F., Guibert, S., Isaksen, I. S. A., Iversen, T., Koch, D., Kirkevåg, A., Liu, X., Montanaro, V., Myhre, G., Penner, J. E., Pitari, G., Reddy, S., Seland, ., Stier, P., and Takemura,

T. (2006): Radiative forcing by aerosols as derived from the AeroCom present-day and pre-industrial simulations, Atmos. Chem. Phys., 6, 5225-5246, doi:10.5194/acp-6-5225-2006, 2006.

Schuster G. L., O. Dubovik, and B. N. Holben, Angstrom exponent and bimodal aerosol size distributions, J. Geophys. Res., 111, D07207, doi:10.1029/2005JD006328, 2006.

Seinfeld J. and Pandis S., Atmospheric Chemistry and Physics: From Air Pollution to Climate Change, 2nd Edition, Wiley, 2006.

Stephens G. L., Vane D. G., Boain R. J., Mace G. G., Sassen K., Wang Z., Illingworth A. J., O'Connor E. J., Rossow W. B., Durden S. L., Miller S. D., Austin R. T., Benedetti A., Mitrescu C. and The CloudSat Science Team, The CloudSat mission and the A-Train: A new dimension of space-based observations of clouds and precipitation, Bulletin of the American Meteorological Society 83 (12), 1771-1790, 2002.

Sundström, A.-M., Remote Sensing of Aerosols: Applications for Air Quality and Climate Studies, Report Series in Aerosol Science, Finnish Association for Aerosol Research, No. 158, 2014.

Takemura T., Nakajima T., Dubovik O., Holben B. N. and Kinne S., Single-Scattering Albedo and Radiative Forcing of Various Aerosol Species with a Global Three-Dimensional Model, Journal of Climate 15, 4, 333-352, 2002.

Weitkamp C., Lidar: Range-Resolved Optical Remote Sensing of the Atmosphere, 102, Springer Series in Optical Sciences, Springer Science Business, ISBN 0387251014, 9780387251011, 2006.

Yu, H., M. Chin, D. M. Winker, A. H. Omar, Z. Liu, C. Kittaka, and T. Diehl, Global view of aerosol vertical distributions from CALIPSO lidar measurements and GOCART simulations: Regional and seasonal variations, J. Geophys. Res., 115, D00H30, doi:10.1029/2009JD013364, 2010.

Ångström, A., On the atmospheric transmission of Sun radiation and on dust in the air, Geografiska Annaler, 11, 156-166, 1929.

Atmos. Chem. Phys., 13, 2347–2379, 2013
www.atmos-chem-phys.net/13/2347/2013/
doi:10.5194/acp-13-2347-2013

Atmospheric Chemistry and Physics Open Access

Intercomparison of shortwave radiative transfer schemes in global aerosol modeling: results from the AeroCom Radiative Transfer Experiment

C. A. Randles[1,2], S. Kinne[3], G. Myhre[4], M. Schulz[5], P. Stier[6], J. Fischer[7], L. Doppler[7,8], E. Highwood[9], C. Ryder[9], B. Harris[9], J. Huttunen[10], Y. Ma[11], R. T. Pinker[11], B. Mayer[12], D. Neubauer[13,14], R. Hitzenberger[13,14], L. Oreopoulos[15], D. Lee[15,16], G. Pitari[17], G. Di Genova[17,18], J. Quaas[19], F. G. Rose[20,21], S. Kato[21], S. T. Rumbold[22], I. Vardavas[23], N. Hatzianastassiou[24], C. Matsoukas[25], H. Yu[26,15], F. Zhang[26], H. Zhang[27], and P. Lu[27]

[1]GESTAR/Morgan State University, Baltimore, Maryland, USA
[2]NASA Goddard Space Flight Center (GSFC) Atmospheric Chemistry and Dynamics Lab, Greenbelt, MD, USA
[3]Max Plank Institute for Meteorology, Hamburg, Germany
[4]Center for International Climate and Environmental Research-Oslo (CICERO), Oslo, Norway
[5]Meteorologisk Institutt, Oslo, Norway
[6]Department of Physics, University of Oxford, Oxford, UK
[7]Institut für Weltraumwissenschaften, Freie Universität, Berlin, Germany
[8]LATMOS-IPSL, Paris, France
[9]Department of Meteorology, University of Reading, Reading, UK
[10]Finnish Meteorological Institute, Kuopio, Finland
[11]University of Maryland, Department of Atmospheric and Oceanic Science, Maryland, USA
[12]Ludwig-Maximilians-Universitaet, Munich, Germany
[13]Research Platform: ExoLife, University of Vienna, Vienna, Austria
[14]Faculty of Physics, University of Vienna, Vienna, Austria
[15]NASA GSFC Climate and Radiation Laboratory, Greenbelt, Maryland, USA
[16]Seoul National University, Seoul, Republic of Korea
[17]Department of Physical and Chemical Sciences, University of L'Aquila, L'Aquila, Italy
[18]Space Academy Foundation, Fucino Space Center, Ortucchio, Italy
[19]Institut für Meteorologie, Universität Leipzig, Leipzig, Germany
[20]SSAI, Hampton, VA, USA
[21]NASA Langley Research Center (LaRC), Hampton, Virginia, USA
[22]UK Met Office (UKMO) Hadley Center, Exeter, UK
[23]Department of Physics, University of Crete, Crete, Greece
[24]Laboratory of Meteorology, Department of Physics, University of Ioannina, Ioannina, Greece
[25]Department of Environment, University of the Aegean, Aegean, Greece
[26]Earth System Science Interdisciplinary Center (ESSIC), University of Maryland, College Park, Maryland, USA
[27]Laboratory for Climate Studies, CMA, National Climate Center, Beijing, China

Correspondence to: C. A. Randles (cynthia.a.randles@nasa.gov)

Received: 31 July 2012 – Published in Atmos. Chem. Phys. Discuss.: 19 December 2012
Revised: 15 February 2013 – Accepted: 22 February 2013 – Published: 1 March 2013

Published by Copernicus Publications on behalf of the European Geosciences Union.

Abstract. In this study we examine the performance of 31 global model radiative transfer schemes in cloud-free conditions with prescribed gaseous absorbers and no aerosols (Rayleigh atmosphere), with prescribed scattering-only aerosols, and with more absorbing aerosols. Results are compared to benchmark results from high-resolution, multi-angular line-by-line radiation models. For purely scattering aerosols, model bias relative to the line-by-line models in the top-of-the atmosphere aerosol radiative forcing ranges from roughly −10 to 20 %, with over- and underestimates of radiative cooling at lower and higher solar zenith angle, respectively. Inter-model diversity (relative standard deviation) increases from ∼10 to 15 % as solar zenith angle decreases. Inter-model diversity in atmospheric and surface forcing decreases with increased aerosol absorption, indicating that the treatment of multiple-scattering is more variable than aerosol absorption in the models considered. Aerosol radiative forcing results from multi-stream models are generally in better agreement with the line-by-line results than the simpler two-stream schemes. Considering radiative fluxes, model performance is generally the same or slightly better than results from previous radiation scheme intercomparisons. However, the inter-model diversity in aerosol radiative forcing remains large, primarily as a result of the treatment of multiple-scattering. Results indicate that global models that estimate aerosol radiative forcing with two-stream radiation schemes may be subject to persistent biases introduced by these schemes, particularly for regional aerosol forcing.

1 Introduction

In order to understand climate and climate change, it is essential to have an accurate understanding of the Earth's radiation budget and how this budget has changed over time. Atmospheric aerosols have a direct effect on the radiation budget through scattering and absorption of primarily solar radiation, and this radiative forcing can be quantified as the net difference in flux at a given level with and without aerosol. Mainly scattering aerosols such as sulphate generally have a negative or cooling radiative effect at the top of the atmosphere (TOA). More absorbing aerosols such as black carbon can have a radiative cooling or warming effect on the climate system depending on the brightness of the surface or clouds beneath them (Chýlek and Coakley, 1974). Aerosols may also have indirect and semi-direct effects on climate, which are due to microphysical and thermodynamic interactions with clouds, respectively, that impact cloud radiative forcing.

There has been considerable progress in the global modeling of aerosols (e.g. Textor et al., 2006; Koch et al., 2009); however, the uncertainty in estimates of direct aerosol radiative forcing, often measured by the diversity in global model estimates, remains high (Forster et al., 2007; Myhre et al., 2013). In cloud-free conditions, quantification of the direct aerosol radiative effect in atmospheric models depends on knowledge of aerosol optical properties (aerosol optical depth, single scattering albedo, asymmetry parameter, and their wavelength dependence) and wavelength dependent surface albedo. While uncertainties in estimates of aerosol radiative forcing are primarily due to uncertainties in the knowledge of these properties and how they are parameterized (e.g. Boucher et al., 1998), the treatment of radiative transfer in global models, including the accuracy of the method, its spectral resolution, and the treatment of molecular and multiple-scattering, also contribute to the multi-model diversity in estimates of direct aerosol radiative forcing (e.g. Halthore et al., 2005; Oreopoulos et al., 2012).

The aerosol model intercomparison initiative (AeroCom) was created in 2002 with the goal of providing a platform for detailed evaluations of aerosol simulations in global models (http://aerocom.met.no/), focusing in particular on the diversity in global estimates of anthropogenic aerosol direct radiative forcing. AeroCom Phase I explored the inter-model diversity in aerosol processes and properties that contribute to differences in the aerosol optical properties used to quantify radiative forcing (Textor et al., 2006, 2007). Despite the diversity in aerosol properties simulated by the AeroCom models, there was surprisingly good agreement in global, annual total aerosol optical depth. However, this agreement did not extend to the sub-component level as there were large differences in the compositional mixture of the aerosol dry mass and water uptake, both of which influence aerosol absorption and radiative forcing (Kinne et al., 2006). After harmonizing emissions, the global, annual mean pre-industrial to present-day direct aerosol radiative forcing (RF) was $-0.22\,\mathrm{W\,m^{-2}}$ with a range of -0.41 to $+0.04\,\mathrm{W\,m^{-2}}$ and standard deviation (SD) of $\pm 0.16\,\mathrm{W\,m^{-2}}$ (or $\pm$ 73 % of the mean; Schulz et al., 2006). Considerable diversity in aerosol residence times, mass extinction coefficients, forcing per unit optical depth (forcing efficiency) and the ratio of all-sky to clear-sky forcing contributed to the diversity in RF with harmonized emissions (Schulz et al., 2006).

Prior to AeroCom Phase I, the large inter-model diversity in aerosol models was not recognized by the community at large; however, reasons for this diversity required more investigation. As a result of this and the increasing complexity of aerosol models and their coupling to transport and climate models, investigators have proposed numerous experiments for AeroCom Phase II (Schulz et al., 2009). Three additional Phase II experiments have been proposed to investigate the model diversity in aerosol radiative forcing. Myhre et al. (2013) examines the pre-industrial to present-day anthropogenic aerosol direct radiative forcing in 16 global aerosol models of various complexity. The remaining two studies aim to understand inter-model diversity by removing host model uncertainties that arise during the simulation of aerosol distributions and aerosol optical properties. In the AeroCom Prescribed Experiment (Stier et el., 2012),

aerosol optical properties (aerosol optical depth, Ångström exponent, single scattering albedo, and asymmetry parameter) are prescribed to examine the inter-model diversity in non-aerosol related host-model process and assumptions that impact RF calculations (e.g. surface albedo and clouds). As a subset and simplification of the Prescribed Experiment, the offline AeroCom Radiative Transfer Experiment presented here examines the diversity in aerosol radiative forcing due to differences in global model radiation schemes.

There have been numerous intercomparisons of shortwave radiation codes in the past. Fouquart et al. (1991) examined 26 radiation schemes ranging from high to low spectral resolution and found substantial discrepancies in computed fluxes for even the simplest prescription of only pure water vapor absorption. When including highly scattering aerosols and a fixed surface albedo, the relative standard deviation for the eleven models considered ranged from 23 to 114 % as the solar zenith angle (SZA) decreased from 75° to 30° (Fouquart et al., 1991; Boucher et al., 1998). Boucher et al. (1998) found that the relatively high (8 %) standard deviation in zenith angle-average broadband forcing due to prescribed non-absorbing sulfate aerosols was due to differences in the treatment of Mie scattering, multiple scattering, phase functions, and spectral and angular model resolution. Even higher diversity was found for radiative forcing calculated at specific solar zenith angles (i.e. 7.8°, 71.6°, and 83.4°). A more recent and extensive study by Halthore et al. (2005) found substantial differences in TOA RF with prescribed aerosol optical properties and surface albedo that was higher at lower solar zenith angles (30° vs. 75°) and decreased with increased aerosol optical depth.

In this study we adapt the protocol from Halthore et al. (2005), which itself was inspired by Fouquart et al. (1991). We first focus on inter-model differences in Rayleigh scattering in cloud- and aerosol-free conditions with prescribed standard atmospheres (i.e. prescribed ozone and water vapor distributions) and surface albedo. We also consider two simple cases with prescribed aerosol optical properties, including both scattering-only and absorbing aerosols separately, to examine inter-model differences in clear-sky (cloud-free) aerosol radiative forcing. Only solar wavelengths are examined in this study because AeroCom is primarily interested in anthropogenic aerosol radiative forcing rather than longwave aerosol effects that are strongly influenced by natural (e.g. dust) aerosol. We examine the clear-sky fluxes and aerosol radiative forcing as a function of solar zenith angle (SZA). Where possible and appropriate, we make comparisons to earlier intercomparison studies. It should be noted that the conditions specified in this study are not meant to reflect actual atmospheric conditions, which may vary considerably from those considered here. For climate studies, it is not the error in calculating radiative fluxes under a given set of conditions, but the systematic error that occurs over large time and spatial scales, that is of primary importance (Arking, 2005). However, it is important to understand how forcing varies with SZA because zenith-angle averaged forcing assumes the uniform geographic distribution of aerosol optical properties, surface albedo, and clouds – conditions never achieved in the actual climate system (Boucher et al., 1998).

2 Protocol

Table 1 provides a brief description of the participating models, including their spectral resolution and multiple-scattering and gaseous transmission schemes. More detailed descriptions and references are given in Appendix A and Appendix Table A1. The data used in this study are made publicly available via the AeroCom server (http://aerocom.met.no/). We have submissions from 31 radiation schemes. Two high-spectral resolution line-by-line (LBL) models (Models #1 and 2), where transmittance is treated explicitly, serve as benchmarks for comparison. Models #1–3, 5–9, and 30–31 use multi-stream (i.e. >2-stream) approximations to the solution of the radiative transfer equation while the remaining models use the two-stream approximation. Multiple-scattering schemes include the discrete-ordinate method (DISORT; Stamnes et al., 1988, Models #1–7), variations of the Eddington approximation (e.g. Joseph et al., 1976, Models #8–29), and the matrix-operator method (MOM; Plass et al., 1973, Models #30–31). For the lower spectral resolution band-models, gaseous transmittance is generally achieved using either the correlated-*k* method (*ck*-D; e.g. Lacis and Oinas, 1991; Fu and Liou, 1992; Kato et al., 1999) or the exponential sum fit transmission scheme (ESFT; e.g. Wiscombe and Evans, 1977; Sun and Rikus, 1999). A number of these schemes are currently in use in global climate models, some are used for offline calculation of aerosol radiative forcing, and still others are used, for example, to perform detailed calculations of photolysis rates in coupled climate-chemistry models (see Appendix A).

Table 2 gives an overview of the experiment protocol and the cases considered. Fluxes were reported at two nominal wavelength bands: broadband (0.2–4.0 µm) and UV-visible (UV-VIS; 0.2–0.7 µm). However, due to the difficulty in configuring some models to these exact bands, we accepted variations in these wavelength ranges. To facilitate intercomparison, we normalized all flux components by the model-specific downwards irradiance at the top-of-the-atmosphere (TOA) in the appropriate band (broadband or UV-VIS) and then scaled these normalized fluxes by the inter-model median TOA downwards irradiance (such that all flux quantities examined are in $\mathrm{W\,m^{-2}}$; see Fig. 2). We requested the following flux fields: total (direct + diffuse) down at the surface broadband, diffuse flux down at the surface broadband, total diffuse up at TOA broadband, and total down at surface UV-visible. These flux (F) quantities allow us to calculate TOA aerosol radiative forcing (RF) and absorptance (A) in the broadband. Absorptance is calculated as in

Table 1. Models, investigators, and description[a]

Model	Name	Investigator(s)	Description[b,c]
1	GENLN2-DISORT	Myhre	16-streams DISORT, LBL (HITRAN2008) 0.02 cm^{-2} resolution, 0.2–5.0 µm, AFGL
2	RFM DISORT (RFMD)	Highwood, Ryder, Harris	4-streams DISORT (HITRAN 2004), LBL 1 cm^{-1} resolution, 0.2–10 µm, AGFL
3	Oslo-DISORT	Myhre	8-stream DISORT, ESFT (HITRAN92 + GENLN2 for H_2O), 4 (2/1), 0.3–4.0 µm, AFGL
4	Oslo-2Stream	Myhre	2-stream DISORT, ESFT (HITRAN92 + GENLN2 for H_2O), 4 (2/1), 0.3–4.0 µm, AFGL
5	UNIVIE-Streamer	Neubauer, Hitzenberger	8-stream DISORT, ESFT (LOWTRAN7 + LBLRTM), 24 (10/14), 0.2–5.0 µm, AFGL
6	FMI-libRadtran	Huttunen	8-stream DISORT2 δ-M scaling on, *ck*-D (HITRAN92), 32 (16/16), 0.24–4.61 µm, AFGL
7	LMU-libRadtran	Mayer	6-stream DISORT2, *ck*-D (HITRAN92), 32 (16/16), 0.2401–4.6057 µm, AFGL
8	GSFC-FL	Yu	4-stream δ-Ed, *ck*-D (HITRAN82), 15 (10/5), 0.2–4.0 µm, AFGL
9	CAR-FLG	F. Zhang	4-stream δ-Ed, *ck*-D (1982AGFL + HITRAN2*k*), 6 (1/5), 0.2–4.0 µm, AFGL
10	LaRC-FL	Rose, Kato	2-stream δ-Ed, *ck*-D (HITRAN2*k*), 18 (10/8), 0.17–4.0 µm, 32-layers
11	CAR-RRTMG	F. Zhang	2-stream δ-Ed, *ck*-D (LBLRTM), 14 (5/9), 0.2–12.196 µm, AFGL
12	RRTMG-SW	Oreopoulos, Lee	2-stream δ-Ed, *ck*-D (LBLRTM), 14 (4–5/10–9), 0.2–12.196 µm, AFGL
13	LMU-2stream	Mayer	2-stream δ-Ed, *ck*-D (HITRAN92), 32 (16/16), 0.2401–4.6057 µm, AFGL
14	MPI-2stream	Kinne	2-stream δ-Ed, *ck*-D (LOWTRAN5+Vigroux), 8 (4/4), µm, 20-layers
15	CAR-GSFC	F. Zhang	2-stream δ-Ed+adding (CS), *k*-distribution (HITRAN96), 11 (8/3), 0.175-10 µm, AFGL
16	BCC-RAD	H. Zhang, P. Lu	2-stream δ-Ed (ES96), *ck*-D (HITRAN2*k*), 9 (7/2), 0.2–3.73 µm, AFGL
17	CAR-CCCMA	F. Zhang	δ-Ed+adding, *ck*-D (HITRAN96), 4 (9-sub/3), 0.2–4.0 µm, AFGL
18	ECHAM5.5	Quaas, Kinne, Stier	2-stream δ-Ed, Padé approx., 6 (3/3), 0.185–4.0 µm, AFGL
19	UMD-SRB	Ma, Pinker	2-stream δ-Ed, *k*-distribution for H_2O and Lacis and Hansen (1974) for O_3 (HITRAN-96), 7 (4/3), 0.2–4.0 µm, 31-layers (Clear-Sky) otherwise variable
20	ES96-6	Highwood, Ryder, Harris	2-stream PIFM, *ck*-D (H_2O: HITRAN 2003, O_3:HITRAN92), 6 (2/3), 0.2–10 µm, AFGL
21	ES96-220	Highwood, Ryder, Harris	2-stream PIFM, *ck*-D (H_2O: HITRAN 2003, O_3:HITRAN92), 220 (118/102), 0.2–10 µm, AFGL
22	ES96-6-D	Highwood, Ryder, Harris	2-stream PIFM + δ-scaling, *ck*-D (H_2O: HITRAN 2003, O_3:HITRAN92), 6 (2/3), 0.2–10 µm, AFGL
23	ES96-220-D	Highwood, Ryder, Harris	2-stream PIFM + δ-scaling, *ck*-D (H_2O: HITRAN 2003, O_3:HITRAN92) 220 (118/102), 0.2–10 µm, AFGL
24	UKMO-HadGEM2	Rumbold	2-stream PIFM + δ-scaling (ES96), *ck*-D (H_2O: HITRAN 2003, O_3:HITRAN92), 6 (2/3), 0.2–10 µm, AGFL
25	CAR-CAWCR	F. Zhang	2-stream δ-Ed (SES), ESFT (GENLN2), 9 (4/5) 0.2–5.0 µm, AFGL
26	CAR-CAM	F. Zhang	2-stream δ-Ed, ESFT (HITRAN2*k*), 19 (8/11), 0.2–5.0 µm, AFGL
27	ULAQ	Pitari, Di Genova	2-stream δ-Ed, ESFT (MPI-MAINZ + HITRAN92 for H_2O), 235 (150/85), 0.1216–7 µm, 570 m
28	FORTH	Vardavas, Hatzianastassiou Matsoukas	2-stream δ-Ed, ESFT, 128 (115/13), 0.2–9.52 µm, 100-layers
29	CAR-GFDL	F. Zhang	δ-Ed+adding, ESFT (HITRAN92), 18 (13/5) 0.173–20 µm, AFGL
30	MPI-MOM	Kinne	10-streams Matrix-Operator adding-doubling, *ck*-D (LOWTRAN5+Vigroux), 8 (4/4), µm, 20-layers
31	MOMO	Doppler, Fischer	Matrix-Operator adding-doubling, non-correlated *k* (HITRAN-2008), 97 (67/30), 0.2–100 µm, AFGL

[a] See Appendix A for further model details. Appendix Table A1 provides additional information on gaseous transmission.
[b] Format: #-streams and multiple-scattering scheme, gaseous transmittance scheme (transmission database), total # bands (# UV-Vis/# Near-IR), full λ-range [µm], vertical resolution.
[c] Abbreviations: RT = radiative transfer, LBL = line-by-line, DISORT = discrete-ordinate method, PIFM = Practical Improved Flux Method, Ed = Eddington, δ-Ed = delta Eddington, ES96 = Edwards and Slingo (1996), SES = Sun-Edwards-Slingo, CS = Chou and Suarez, FL = Fu-Liou, FLG = Fu-Liou-Gu, ESFT = exponential sum fit transmission, *ck*-D = correlated *k*-distribution, AFGL = Air Force Geophysical Laboratory vertical resolution.

Halthore et al. (2005) and represents the fraction of TOA irradiance absorbed in the atmosphere:

$$A = \frac{(F^{\downarrow}_{\mathrm{TOA}} - F^{\uparrow}_{\mathrm{TOA}}) - (F^{\downarrow}_{\mathrm{SFC}} - F^{\uparrow}_{\mathrm{SFC}})}{F^{\downarrow}_{\mathrm{TOA}}} \quad (1)$$

where arrows indicate the direction of the flux (positive down). Additionally, the surface albedo (α) is fixed to the same value for all wavelengths, allowing for the calculation of surface (SFC) aerosol RF ($F^{\uparrow}_{\mathrm{SFC}} = \alpha F^{\downarrow}_{\mathrm{SFC}}$). Flux in the near-IR is computed as the difference between broadband and UV-VIS.

2.1 Case 1: Rayleigh scattering atmosphere

Only molecular scattering and absorption (Rayleigh atmosphere) occur in the aerosol- and cloud-free Case 1. Following Halthore et al. (2005), shortwave flux components were computed using two different standard atmospheric profiles for ozone (O_3) and water vapor (H_2O): the Air Force Geophysics Laboratory (AFGL; Anderson et al., 1986) subarctic winter (SAW, lower humidity) and tropical atmospheres (TROP, higher humidity). Figure 1 shows the prescribed O_3 and H_2O profiles. Modelers were given the standard atmospheres at 1-km resolution from 0–26 km and 2-km from 26–120 km (corresponding pressure levels were also provided); it was up to the individual contributor to vertically interpolate these fields if needed (see Appendix A). Fluxes are analyzed at two solar zenith angles (SZA), ranging from low (30°) to high (75°), to provide a range of conditions that representative of tropical and high-latitude conditions, respectively. The wavelength-independent Lambertian surface albedo (α) was prescribed as 0.2. This case only considers cloud- and aerosol-free conditions; it thus highlights the transmittance of the radiation schemes considered. Results from Case 1 are presented in Sect. 3.1.

Table 2. Protocol summary.

Experiment	Case 1	Case 2a	Case 2b
Aerosol	None (Rayleigh)	Fixed	Fixed
AOD (0.55 µm)	0	0.2	0.2
Ångström Parameter	Spectral dependence of AOD: $AOD = \exp(-1.0 \times \ln(\lambda/0.55) + \ln(0.2))$		
Asymmetry (g) Parameter[a]	N/A	0.7	0.7
SSA[a]	N/A	1.0	0.8
Surface Albedo[a]	0.2, globally, spectrally uniform		
Atmosphere[b]	AFGL "Tropical" (TROP) and "Sub-Arctic Winter" (SAW) (O_3 and H_2O profiles w/1-km resolution)		
Clouds	NONE		
Solar Zenith Angle	30°, 75° for each atmosphere		

[a] Solar-spectrally invariant.
[b] TROP has higher humidity (H_2O mixing ration) and ozone (see Fig. 1).

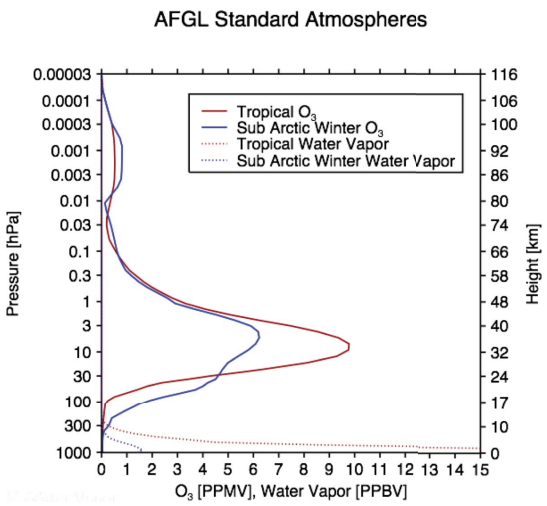

Fig. 1. Prescribed AFGL profiles of Ozone (O_3) and Water Vapor (H_2O).

2.2 Case 2a and 2b: cloud-free atmosphere with aerosols

Case 2a (Scattering Aerosols) augments Case 1 by considering a simple prescription of purely scattering aerosols. AOD at 550 nm is prescribed at 0.2 and linearly distributed in the lowest 2 km of the host model. This corresponds roughly to the "high AOD" case considered by Halthore et al. (2005). The Ångström exponent is given as 1.0 at 550 nm such that at other wavelengths (λ; µm), $AOD = \exp(-1.0 \times \ln(\lambda/0.55) + \ln(0.2))$. The single scattering albedo (SSA) is solar-spectrally invariant and set equal to 1.0 for scattering aerosols. The asymmetry parameter (g) is prescribed at 0.7 (forward-scattering) and is also solar-spectrally invariant. In Case 2b (Absorbing Aerosols), we consider a simple prescription of more absorbing aerosols. Aerosol properties are as in Case 2a, however the single scattering albedo is prescribed at 0.8 (solar-spectrally invariant SSA). Note that in Case 2b the aerosols *both* scatter and absorb solar radiation. These cloud-free aerosol cases shows how the models handle multiple scattering and atmospheric absorption by aerosols. Flux results from Case 2a and 2b are presented in Sect. 3.2.

2.3 Case 2a and 2b: aerosol direct radiative forcing

The fluxes considered in Cases 1 and 2 provide the necessary information to calculate broadband aerosol direct radiative forcing (RF). Here, RF [W m^{-2}] is defined as the difference (down ↓ – up ↑) in flux (F) with and without aerosols present in the atmosphere:

$$\mathrm{RF} = (F^{\downarrow} - F^{\uparrow})_{\mathrm{Case\_2}} - (F^{\downarrow} - F^{\uparrow})_{\mathrm{Case\_1}} \quad (2)$$

Defined in this way (positive down), negative values imply aerosol radiative cooling and positive values imply aerosol radiative warming of the climate system. We compute RF at the top-of-the-atmosphere (TOA) and the surface (SFC). The atmospheric forcing (ATM) is the difference between the two: ATM = TOA–SFC. Because aerosol RF is calculated as a difference in fluxes with and without aerosols holding atmospheric state constant, errors in the treatment of the Rayleigh atmosphere (Case 1) tend to be cancelled to first order. However, we examine aerosol RF because it is of primary interest to the AeroCom community and remains a major source of uncertainty in our understanding of anthropogenic climate change (Solomon et al., 2007). Because we consider harmonized surface and aerosol optical properties, these RF calculations should indicate differences in how models treat multiple-scattering, rather than how an individual model simulates aerosol properties (mass, lifetime, etc.) and their resulting direct RF. Note that global, diurnally-averaged results from the AeroCom Prescribed Experiment FIX2–FIX0 in clear-sky (cloud-free) conditions are comparable to Case 2a. However, in the Prescribed Experiment the surface albedo and gaseous absorbers are not fixed (Stier et el., 2012). Similarly, results from Case 2b are analogous to the global average FIX3–FIX0 clear-sky results in Stier et el. (2012). We examine aerosol RF in Sect. 3.3 and draw comparisons to other Phase II AeroCom studies in Sect. 3.4.

3 Results

Recall that results from each case are first normalized to the model-specific TOA downwards flux in the appropriate band (broadband or UV-VIS); the normalized fluxes are then scaled by the multi-model median TOA flux (see Fig. 2). We

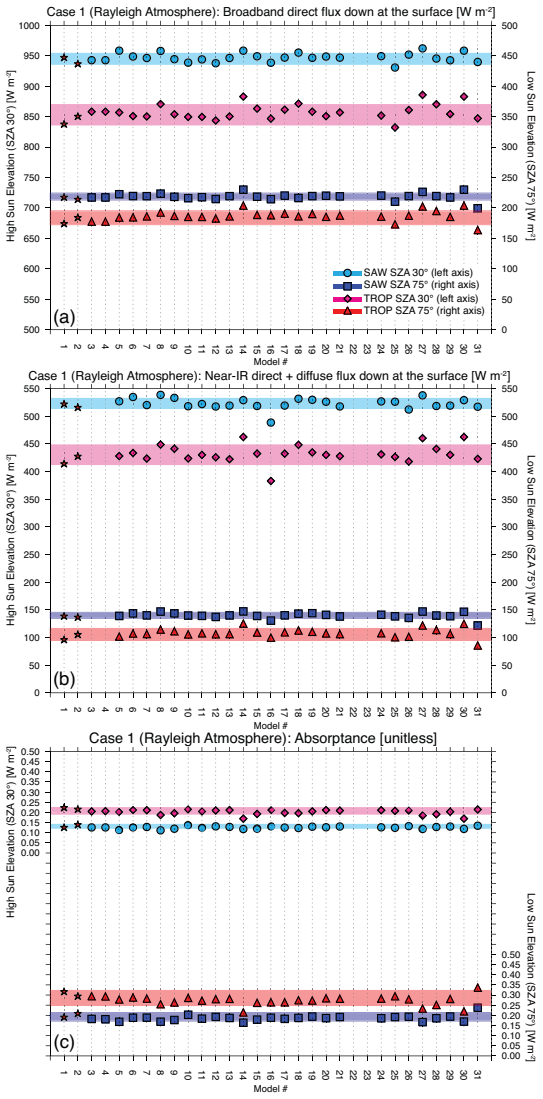

Fig. 2. Summary of results for Case 1 (Rayleigh Atmosphere) in $W\,m^{-2}$: **(a)** direct broadband flux down at the surface, **(b)** total (direct plus diffuse) near-IR down at the surface (calculated as the difference between broadband and UV-VIS), and **(c)** broadband absorptance calculated as in Eq. (1). Line-by-line results (stars) and non-LBL results (non-stars) are given as a function of Model # (Table 1). Shading represents the greater of ± 1 standard deviation from the LBL or non-LBL mean. Normalized results were scaled by the following broadband (UV-VIS) TOA downwards fluxes: 1189.28 (563.38) $W\,m^{-2}$ for SZA 30° and 355.43 (168.37) $W\,m^{-2}$ for SZA 75°. Note that the mean bias of TOA downward fluxes for non-LBL models relative to the LBL models was 2% in the broadband and 2.4 % in the UV-VIS. Models 22–23 are omitted because they are the same as Models 20–21 in the clear-sky case. Models 3–4 did not provide UV-VIS fluxes.

tabulate results separately for the line-by-line (LBL) benchmark codes (Models #1 and 2) and the remaining non-LBL models. We calculate the relative standard deviation (RSD) in order to evaluate overall model diversity, where RSD = $|\frac{\sigma}{\mu}|$, σ is the standard deviation, and μ the mean value of the respective parameter. The RSD is calculated separately for the two LBL models and the non-LBL models. The average bias of the non-LBL models relative tho the average benchmark LBL results is expressed as a percent difference from the LBL-mean (i.e. $100 \times (\mu_{\text{models}} - \mu_{\text{LBL}})/\mu_{\text{LBL}}$). To visualize non-LBL model diversity, we examine the individual model bias relative to the non-LBL model mean.

3.1 Case 1 (Rayleigh atmosphere)

Figure 2a shows the direct downwards broadband flux in cloud- and aerosol-free conditions for each solar zenith angle and standard atmosphere combination. While most models fall within the inter-model diversity (the greater of ± 1 standard deviation from the LBL or non-LBL model mean; shading), models 14, 25, 27, 30, and 31 are often outliers and are not included in the summary statistics for the Rayleigh atmosphere case in Table 3. (Appendix Table A2 provides statistics including all models). Of these models, models 14 and 30 use the same gaseous transmission scheme (Appendix A). Note that models 22 and 23 are identical to models 20 and 21 for the Rayleigh atmosphere case and are thus omitted for Case 1; however they are included in Case 2 because they use different multiple-scattering schemes (Table 1).

The low value of RSD for both LBL and non-LBL models (Table 3) indicates the best agreement in direct broadband flux down at the surface when the water vapor slant path is at its lowest (30° in the sub-Arctic winter). Inter-model differences increase both with increased solar zenith angle and increased water vapor (i.e. the tropical AFGL profile), with the former having a stronger impact on the RSD. This pattern of inter-model difference agrees with the findings of Halthore et al. (2005), and the agreement between models in this study is also generally better than 2 %. Our model diversity is within ~30 % of the broadband direct flux results for the 16 models considered in Halthore et al. (2005).

Relative to the LBL models, models in this study tend to overestimate the direct broadband radiation at the surface by <2 % under most conditions (Table 3). We note that in addition to prescribing the AFGL ozone and water vapor profiles, Halthore et al. (2005) also specified N_2 and O_2 abundances as a function of height from MODTRAN and fixed the CO_2 mixing ratio at 360 ppm. In our results, individual modelers choose the specification of trace gasses excluding O_3 and H_2O. A sensitivity study to the inclusion of additional gaseous absorbers was performed using the CAR ensemble modeling system (Liang and Zhang, 2012; Zhang et al., 2013), which provided results for seven of the radiation schemes considered here (Table 1). Addition of N_2O, CH_4, and CO_2 contributed to an additional 1 % decrease in

Table 3. Case 1: Summary of Statistics for the Rayleigh Atmosphere[a,b,c]

	SAW		TROP	
	30° SZA	75° SZA	30° SZA	75° SZA
Direct Broadband Downwards Flux at Surface				
LBL Avg	942.4	216.2	844.5	179.6
LBL RSD	0.8 %	1.1 %	1.1 %	3.9 %
Model Avg.	946.8	218.6	856.3	186.3
Avg. Bias	0.5 %	1.1 %	1.4 %	3.7 %
Model RSD	0.6 %	1.0 %	0.9 %	2.1 %
Diffuse Broadband Downwards Flux at Surface				
LBL Avg	64.4	37.2	64.0	36.8
LBL RSD	0.9 %	1.5 %	0.4 %	0.5 %
Model Avg.	63.4	38.0	63.3	37.9
Avg. Bias	−1.5 %	2.1 %	−1.1 %	3.0 %
Model RSD	7.0 %	4.8 %	6.8 %	4.6 %
Diffuse Broadband Flux Up at TOA				
LBL Avg	227.6	82.6	204.7	75.2
LBL RSD	1.3 %	1.5 %	1.3 %	1.8 %
Model Avg.	230.5	83.9	210.1	77.8
Avg. Bias	1.3 %	1.6 %	2.6 %	3.5 %
Model RSD	1.1 %	1.9 %	1.4 %	2.1 %
Total (Direct + Diffuse) UV-VIS Downwards Flux at Surface				
LBL Avg	489.2	115.8	489.1	115.7
LBL RSD	0.7 %	1.3 %	0.2 %	0.3 %
Model Avg.	489.3	116.7	490.3	117.5
Avg. Bias	0.0 %	0.8 %	0.3 %	1.6 %
Model RSD	1.1 %	2.6 %	1.0 %	2.4 %
Total near-IR Downwards Flux at Surface[d]				
LBL Avg	519.1	138.0	421.1	101.1
LBL RSD	0.8 %	1.0 %	2.3 %	6.5 %
Model Avg.	521.7	139.9	429.1	107.3
Avg. Bias	0.5 %	1.4 %	1.9 %	6.1 %
Model RSD	2.0 %	2.5 %	3.2 %	3.6 %
Broadband Absorptance[e]				
LBL Avg	0.134	0.201	0.221	0.307
LBL RSD	7.2 %	6.4 %	2.5 %	5.1 %
Model Avg.	0.126	0.186	0.204	0.276
Avg. Bias	−5.7 %	−7.6 %	−7.5 %	−10.1 %
Model RSD	4.7 %	4.3 %	3.8 %	4.2 %

[a] Flux units W m^{-2}; scaled normalized results as described in the text and Fig. 2. Statistics for non-LBL models excludes models 14, 25, 27, 30, and 31. Models 22 and 23 are excluded because they are the same as models 20 and 21 in the Rayleigh atmosphere. Table A2 gives statistics excluding models 22–23 only.
[b] Line-by-line (LBL) benchmarks (Avg. of models #1 and #2) and non-LBL model results.
[c] Avg. Bias is expressed as a percentage of the LBL Avg. RSD = standard deviation as a percentage of mean.
[d] Near-IR is calculated as a difference between broadband and UV-VIS.
[e] Absorptance (Eq. 1) is derived assuming $F^{\uparrow}_{SFC} = \alpha F^{\downarrow}_{SFC}$ and surface albedo $\alpha = 0.2$.

Table 4. Statistics for diffuse flux down at surface with aerosols[a]

ATM and SZA	Group 1[b] Bias (RSD)	Group 2[c] Bias (RSD)
Case 2a: Scattering Aerosols		
SAW 30	−0.9 % (3.5 %)	−36.6 % (5.8 %)
SAW 75	2.3 % (5.2 %)	−30.4 % (3.7 %)
TROP 30	0.2 % (3.7 %)	−35.3 % (5.6 %)
TROP75	4.3 % (5.4 %)	−27.1 % (4.4 %)
Case 2b: Absorbing Aerosols		
SAW 30	−0.3 % (3.6 %)	−33.8 % (4.4 %)
SAW 75	3.4 % (5.5 %)	−26.5 % (2.6 %)
TROP 30	1.0 % (3.9 %)	−32.4 % (4.4 %)
TROP 75	5.2 % (5.8 %)	−23.1 % (2.8 %)

[a] Bias = $100 \times \frac{\mu_{Group} - \mu_{LBL}}{\mu_{LBL}}$, RSD = $100 \times \mid \frac{\sigma_{Group}}{\mu_{Group}} \mid$, μ = mean, σ = standard deviation.
[b] Group 1: Model # 3–14, 19–21, and 30–31.
[c] Group 2: Model # 15–18 and 22–29.

broadband downwards flux at the surface, with most of that due to carbon dioxide (F. Zhang, personal communication, 2012). We thus note that diversity in the treatment of other trace gas absorbers may contribute to some of the bias and diversity in our results.

Figure 2b shows the total (direct plus diffuse) downwards flux in the near-IR (i.e. broadband minus UV-VIS). Deficiencies in the near-IR band indicate that models may not adequately treat absorption by water vapor. The statistics in Table 3 indicate increased model diversity (larger RSD) and increased bias relative to the LBL results as the slant-path of water vapor increases. Broadband absorptance calculated according to Eq. (1) is shown in Fig. 2c. Model diversity expressed as RSD is roughly 4 % for broadband absorptance. In the tropical atmosphere, broadband absorptance RSD is slightly higher compared to the ∼3 % diversity found in Halthore et al. (2005). This difference, however, is small considering that the spectral resolution of the models considered in Halthore et al. (2005) was generally much greater than the models in this study.

In the UV-VIS where gaseous absorption is influenced by the amount of ozone, the LBL models show good agreement (RSD $\lesssim$ 1 %; Table 3). However, the non-LBL RSD is higher by about a factor of ∼2 for SAW (less O_3) and a factor of 5–8 for TROP (more O_3). The bias relative to the LBL calculations is low at 30° and increases at 75°. Figure A1a shows the UV-VIS down at the surface expressed as a percent deviation from the non-LBL model mean (i.e. μ excluding only models 1–2 and 22–23). Models that performed well for the broadband may have deficiencies in the UV-VIS range, as exhibited by models such as 5 and 25, which over and underestimate the UV-VIS flux relative to the LBL results (see Fig. A2). Note that Model #5 uses a one-parameter scaling approach to scale the absorption by atmospheric gases

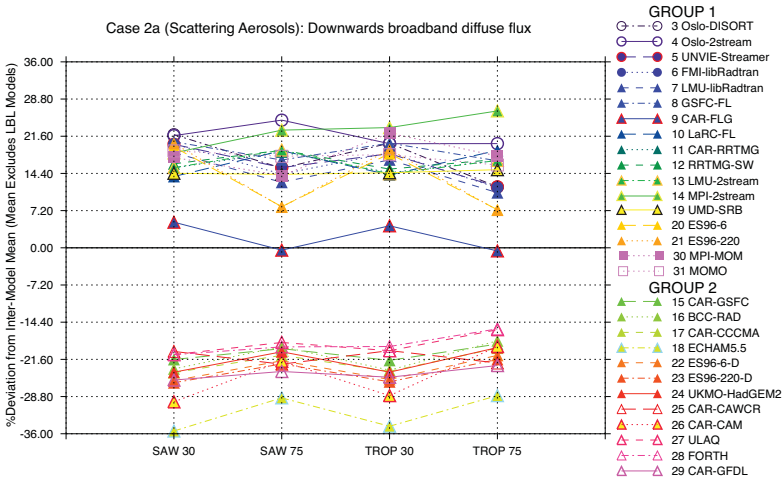

Fig. 3. As a function of standard atmosphere and solar zenith angle, the inter-model diversity in broadband diffuse flux down at the surface for Case 2a (Scattering Aerosols), expressed as a percent deviation from the non-LBL model mean (i.e. all models excluding #1 and 2). Figure A4 shows the inter-model differences in broadband direct and diffuse flux down at the surface for Case 2a and 2b.

to different temperatures and pressures; this reduces the O_3 absorption in the Rayleigh atmosphere case but is less important when calculating aerosol direct and indirect forcing as well as exoplanetary surface temperatures, the primary applications of this model.

The largest inter-model flux differences occur for broadband diffuse flux to the surface (Table 3, Figs. A1b and A3). The RSD is roughly equal for each SZA regardless of prescribed atmosphere, and it is greatest at 30°. Relative to LBL calculations, models generally under- and overestimate broadband diffuse flux at the surface at lower and higher solar zenith angle, respectively. Because much of the diffuse flux occurs in the UV-VIS, deficiencies in the broadband diffuse flux may point to issues in the treatment of ozone absorption. The model diversity for the diffuse flux down at the surface is comparable to Halthore et al. (2005) in the sub-Arctic winter; however, it is considerably (∼5 times) less in the tropical atmosphere. The relatively good agreement in upwards broadband flux at the top-of-the atmosphere (RSD ∼2 %) is similar to the agreement found for the direct broadband flux to the surface as expected due to the prescribed surface albedo.

3.2 Case 2 (fluxes with aerosols)

Flux results for Case 2a (Scattering Aerosols) and Case 2b (Absorbing Aerosols) are summarized in Appendix Tables A3 and A4, respectively. For all flux quantities, model disagreement (RSD) increases with solar zenith angle and, with the exception of downwards UV-VIS flux, is higher in the tropical atmosphere compared to the sub-Arctic winter. In both aerosol cases, models agree within $\lesssim$3 % for all total (direct plus diffuse) flux quantities. For comparison, Halthore et al. (2005) found that model diversity with inclusion of non-absorbing aerosols at high AOD (0.24) as generally within 1–2 %. Model diversity is similar with increased aerosol absorption (decreased SSA), but the magnitude of the bias relative to the LBL-benchmark is generally slightly higher for absorbing aerosols.

The worst model agreement for Case 2 occurs for the components of the total irradiance down at the surface, a finding in accord with Phase I of the Continual Intercomparison of Radiation Codes (CIRC; Oreopoulos et al., 2012). Figures 3 and A4 illustrate the inter-model differences in the diffuse and direct components of the downwards broadband flux. The models tend to fall into two separate groups: those which are approximately equal to the LBL-benchmark (Group 1, Models #3–14, 19–21, 30–31), and those that underestimate it (Group 2; Models #15–18, 22–29). Table 4 gives the statistics for each group relative to the LBL-mean. Despite the different biases in the two groups relative to the LBL-benchmark, the RSD shows that the model diversity is similar for each group (∼3–6 %). Most multi-stream models (#3, 5–9), which include all models that employ the DISORT algorithm for multiple-scattering (#3–7), agree the best with the LBL-benchmarks (see the Appendix Fig. A5 and A6). Both LBL schemes also use DISORT and multiple streams (Table 1).

A sensitivity study using both a delta 2-stream and delta 4-stream approximation was performed using Model #9 (CAR-FLG; F. Zhang, personal communication, 2012). While Model #9 is in Group 1 (Table 4) when run with a delta 4-stream method, using only a delta 2-stream method largely reduces the broadband diffuse flux to the surface such that it

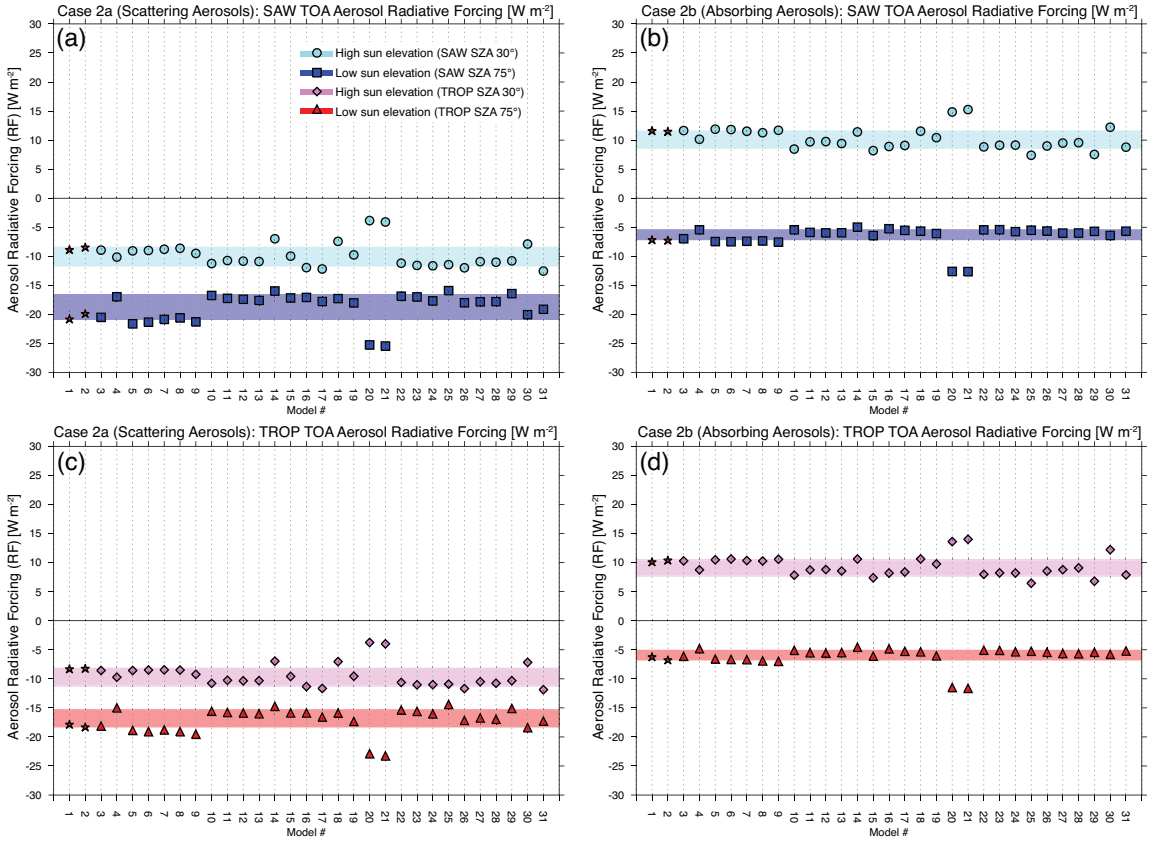

Fig. 4. Summary of results for top of the atmosphere aerosol radiative forcing (TOA RF) in W m^{-2}: **(a)** Case 2a (Scattering Aerosols) SAW, **(b)** Case 2b (Absorbing Aerosols) SAW, **(c)** Case 2a (Scattering Aerosols) TROP, and **(d)** Case 2b (Absorbing Aerosols) TROP. Line-by-line results (stars) and non-LBL results (non-stars) are given as a function of Model # (Table 1). Shading represents the greater of ± 1 standard deviation from the LBL or non-LBL mean (excluding Models 20–21). RF was calculated from Eq. (2) using normalized flux results that were scaled by the broadband downwards fluxes given in Fig. 2.

is closer to the mean flux for Group 2. In the delta-rescaling, the fraction of scattered energy residing in the forward peak (f) for the delta 2-stream and delta 4-stream approximations are $f = \tilde{\omega}_2/5$ and $f = \tilde{\omega}_4/9$, respectively, where $\tilde{\omega}_2$ and $\tilde{\omega}_4$ are the second and fourth coefficients of the phase function. Using the Henyey-Greenstein phase function, $\tilde{\omega}_2 = 5g^2$ and $\tilde{\omega}_4 = 9g^4$ where g is the asymmetry factor. When f decreases, more scattered energy is kept and there is an increase in diffuse flux at the surface. As the number of streams increase from two ($f \sim g^2$) to four ($f \sim g^4$), f decreases, and the diffuse flux down to the surface increases.

Models #20–23, which employ the Practical Improved Flux Method (PIFM) for multiple scattering (Zdunkowski et al., 1980), illustrate that the same 2-stream method can be configured to either more accurately represent diffuse or total flux. In models #22 and 23, δ-rescaling provides more accurate total flux at the expense of the partitioning between the direct and diffuse fluxes because it increases the flux in the direct beam to account for strong forward aerosol scattering. However, while omitting δ-rescaling (models #20 and 21) improves the accuracy of the diffuse beam relative to the LBL-results (Figs. A5 and A6), as shown in Sect. 3.3, it impacts RF estimates.

3.3 Aerosol direct radiative forcing from Case 2a and 2b

Figure 4 shows the top of the atmosphere aerosol radiative forcing. Surface and atmospheric aerosol radiative forcing are shown in Fig. 5. Table 5 gives the multi-model statistics for the aerosol radiative forcing. Note that Models #20-21 are outliers (see Fig. 4). Recall from Section 3.2 that these models are the same as Models #22-23 except that they do not

Table 5. Summary of statistics for aerosol radiative forcing[a, b, c, d]

	Case 2a: Scattering Aerosols		Case 2b: Absorbing Aerosols	
	TOA RF	SFC RF	TOA RF	SFC RF
Sub-Arctic Winter 30° SZA				
LBL Avg.	−8.6	−9.7	11.6	−42.1
LBL RSD	3.4 %	4.2 %	0.7 %	1.4 %
Model Avg.	−10.2 (−10.6)	−11.0 (−11.2)	9.9 (9.4)	−41.8 (−41.6)
Avg. Bias	18.9 % (23.2 %)	13.0 % (15.9 %)	−14.2 % (−18.5 %)	−0.7 % (−1.2 %)
Model RSD	14.7 % (14.3 %)	13.3 % (13.8 %)	14.3 % (12.9 %)	4.1 % (4.3 %)
Sub-Arctic Winter 75° SZA				
LBL Avg.	−20.3	−21.5	−7.2	−37.8
LBL RSD	3.2 %	3.8 %	0.7 %	2.9 %
Model Avg.	−18.2 (−17.4)	−18.6 (−17.5)	−6.1 (−5.7)	−34.7 (−33.5)
Avg. Bias	−10.3 % (−14.2 %)	−13.8 % (−18.7 %)	−15.0 % (−20.1 %)	−8.1 % (−11.2 %)
Model RSD	9.6 % (5.4 %)	11.8 % (5.9 %)	12.6 % (6.3 %)	7.3 % (4.2 %)
Tropics 30° SZA				
LBL Avg.	−8.2	−10.0	10.3	−40.6
LBL RSD	0.7 %	5.1 %	2.0 %	0.5 %
Model Avg.	−9.8 (−10.2)	−10.9 (−11.0)	9.0 (8.7)	−40.4 (−40.1)
Avg. Bias	19.2 % (23.3 %)	8.3 % (10.1 %)	−12.0 % (−15.9 %)	−0.6 % (−1.2 %)
Model RSD	14.5 % (14.2 %)	12.2 % (13.3 %)	15.2 % (15.1 %)	4.0 % (4.2 %)
Tropics 75° SZA				
LBL Avg.	−18.0	−18.9	−6.5	−33.6
LBL RSD	1.8 %	0.1 %	5.8 %	0.8 %
Model Avg.	−16.7 (−16.1)	−16.6 (−15.7)	−5.7 (−5.4)	−31.6 (−30.7)
Avg. Bias	−7.4 % (−10.9 %)	−12.3 % (−17.0 %)	−12.4 % (−16.9 %)	−5.8 % (−8.6 %)
Model RSD	8.9 % (6.1 %)	11.8 % (7.5 %)	11.6 % (7.1 %)	8.3 % (7.3 %)

[a] Forcing units $\mathrm{W\,m^{-2}}$ calculated as in Eq. (2). We exclude Model # 20 and 21 as described in the text.
In parenthesis, we also exclude the multi-stream models (Models # 3 and 5–9) that agree well with LBL results.
[b] Line-by-line (LBL) benchmarks (Avg. of Models #1 and #2) and non-LBL model results.
[c] Avg. Bias is expressed as a percentage of the LBL Avg. Positive values imply that models overestimate radiative cooling or radiative warming. RSD = standard deviation as a percentage of mean.
[d] Unless given, assumed $F^{\uparrow}_{SFC} = \alpha F^{\downarrow}_{TOA}$ and $\alpha = 0.2$ to calculate SFC RF.

include δ-rescaling (and thus sacrifice accuracy in total flux to gain accuracy in diffuse flux). Models #20-21 significantly over- and underestimate both the LBL-mean and the mean of all other models at 30° and 75°, respectively; we thus exclude them from the RF statistics in Table 5. Models using multiple streams (#3, 5–9, 30–31) generally show the best agreement with benchmark LBL calculations of TOA radiative forcing. If we exclude multi-stream models from the statistics in Table 5 (shown in parenthesis), the model bias gets larger but there is an improvement in model diversity (i.e. a reduction in RSD).

For scattering-only aerosols (Case 2a), the magnitude of aerosol cooling increases with solar zenith angle (Table 5). This is expected for an optically thin atmosphere; as the solar zenith angle increases so does the upscatter fraction, and decreases in incident irradiance are compensated by increased optical path length (Nemensure et al., 1995; Halthore et al., 2005). Compared to benchmark LBL calculations (Table 5), models tend to overestimate top of the atmosphere radiative cooling at low SZA and underestimate radiative cooling at high SZA. The magnitude of this bias is less sensitive to the prescribed atmosphere than to solar zenith angle, and is on the order of 20 % at 30 degrees and 10 % at 75 degrees. Model diversity is largest at the lower zenith angle (∼15 % RSD at 30° compared to ∼9 % at 75°). As expected for non-absorbing aerosols, the behavior of the surface radiative forcing in terms of bias and RSD is similar to the results at the TOA.

For more absorbing aerosols (Case 2a, SSA = 0.8), TOA aerosol radiative forcing switches sign from positive to negative (radiative warming to cooling) as solar zenith angle increases. Models underestimate TOA radiative warming by ∼12–14 % at 30° and underestimate radiative cooling at 75° by about 12–15 % relative to the LBL benchmark. Model

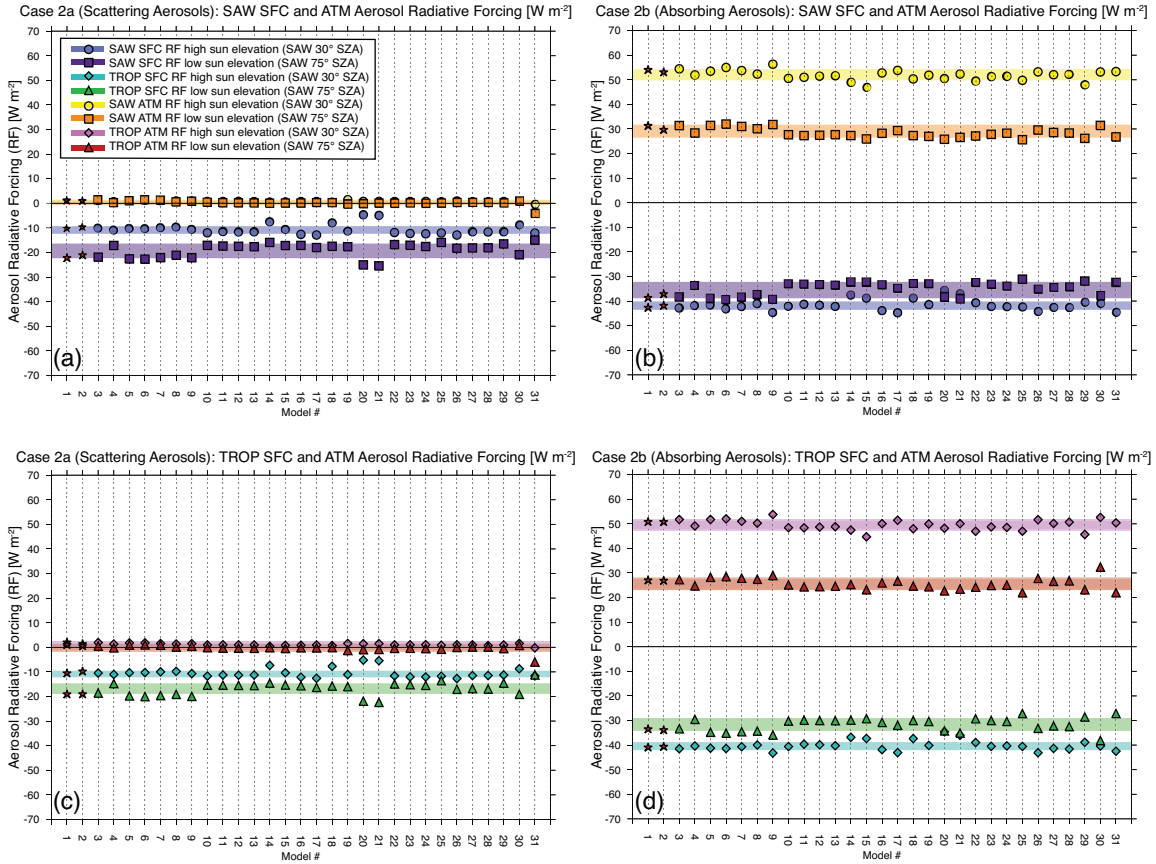

Fig. 5. Summary of results for surface and atmospheric aerosol radiative forcing (SFC and ATM RF) in $\mathrm{W\,m^{-2}}$: **(a)** Case 2a (Scattering Aerosols) SAW, **(b)** Case 2b (Absorbing Aerosols) SAW, **(c)** Case 2a (Scattering Aerosols) TROP, and **(d)** Case 2b (Absorbing Aerosols) TROP. Line-by-line results (stars) and non-LBL results (non-stars) are given as a function of Model # (Table 1). Shading represents the greater of ± 1 standard deviation from the LBL or non-LBL mean. RF was calculated from Eq. (2) using normalized flux results that were scaled by the broadband TOA downwards fluxes given in Fig. 2. The ATM forcing is calculated as a residual from the TOA and SFC RF (i.e. ATM RF = TOA RF − SFC RF).

biases are slightly larger in magnitude for the sub-Arctic winter (lower humidity) compared to the tropics (higher humidity). Model diversity (RSD) is roughly 12–15 % for all conditions considered. Surface radiative forcing for absorbing aerosols shows the least bias compared to the LBL-benchmark as well as the lowest model diversity.

Figure 6 shows bi-variate probability density functions (PDFs) of TOA aerosol radiative forcing for Case 2a (a–d) and Case 2b (e–h). As a function of SZA for either the SAW (Fig. 6a and e) or TROP (Fig. 6b and f) atmospheric profile, the PDF indicates two main groups. Group M1 includes the LBL-models and most of the multi-stream models (#3, 5–9) and group M2 includes the majority of the other models. The near-linear shape of the TOA RF PDFs as a function of atmosphere for SZA 30° (Fig. 6c and g) and SZA 75° (Fig. 6d and h) indicate that the inter-model diversity in TOA RF has a stronger dependence on SZA than on trace-gas absorption, as expected. For absorbing aerosols (Case 2b), inter-model diversity decreases, and this results in less spread in the TOA RF PDF as a function of solar zenith angle for a given atmosphere (Fig. 6e–f). In Fig. 6i–l we show bi-variate PDFs of TOA aerosol RF for each atmosphere-SZA combination for Case 2a (Scattering Aerosols) relative to Case 2b (Absorbing Aerosols). The PDFs are generally fairly linear but appear somewhat bi-modal, with the different modes corresponding to groups M1 and M2. Models 20–21 form a separate mode.

In Fig. 7 we show PDFs of the TOA, SFC, and ATM radiative forcing relative bias compared to the LBL-mean benchmark for all conditions. We see a strong dependence of model bias on solar zenith angle, which is somewhat stronger for

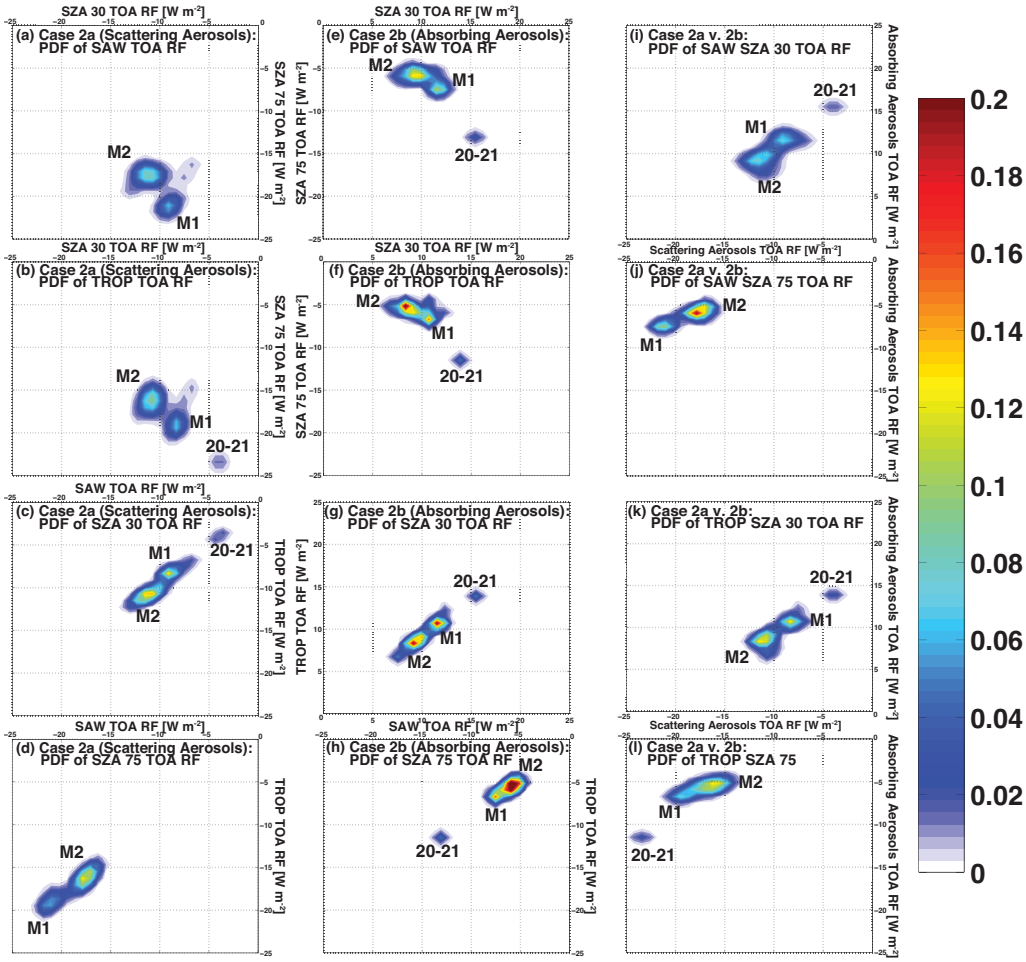

Fig. 6. Bi-variate probability density function (PDF) of TOA aerosol radiative forcing for Case 2a (Scattering Aerosols): **(a)** sub-Arctic winter as a function of solar zenith angle, **(b)** the tropics as a function of solar zenith angle, **(c)** SZA 30° as a function of prescribed atmosphere, and **(d)** SZA 75° as a function of prescribed atmosphere. PDFs of TOA RF for Case 2b (Absorbing Aerosols): **(e)** sub-Arctic winter as a function of solar zenith angle, **(f)** the tropics as a function of solar zenith angle, **(g)** SZA 30° as a function of prescribed atmosphere, and **(h)** SZA 75° as a function of prescribed atmosphere. PDFs of the effect of aerosol absorption (i.e. Case 2a vs. Case 2b) for given conditions: **(i)** SAW SZA 30°, **(j)** SAW SZA 75°, **(k)** TROP SZA 30°, and **(l)** TROP SZA 75°. The PDFs are calculated such that the volume is normalized to unity. Red shading indicates a large concentration of models. Group M1 includes Models #1–3, and 5–9. Group M2 includes most other models (except Models #20–21).

non-absorbing aerosols. Compared to scattering aerosols, absorbing aerosols reduce model biases, particularly for SFC and ATM forcing at lower SZA. Note that the large biases for atmospheric forcing due to scattering aerosols are a consequence of the small value of this quantity ($<1\,\mathrm{W\,m^{-2}}$).

3.4 Comparison to other AeroCom Phase II experiments

As noted in the introduction, two other Phase II AeroCom experiments examine the diversity in aerosol radiative forcing estimates in global models. Myhre et al. (2013) reports the direct aerosol RF for 16 global aerosol models, 8 of which use radiation schemes similar or identical to radiative transfer schemes examined in this work. Results from

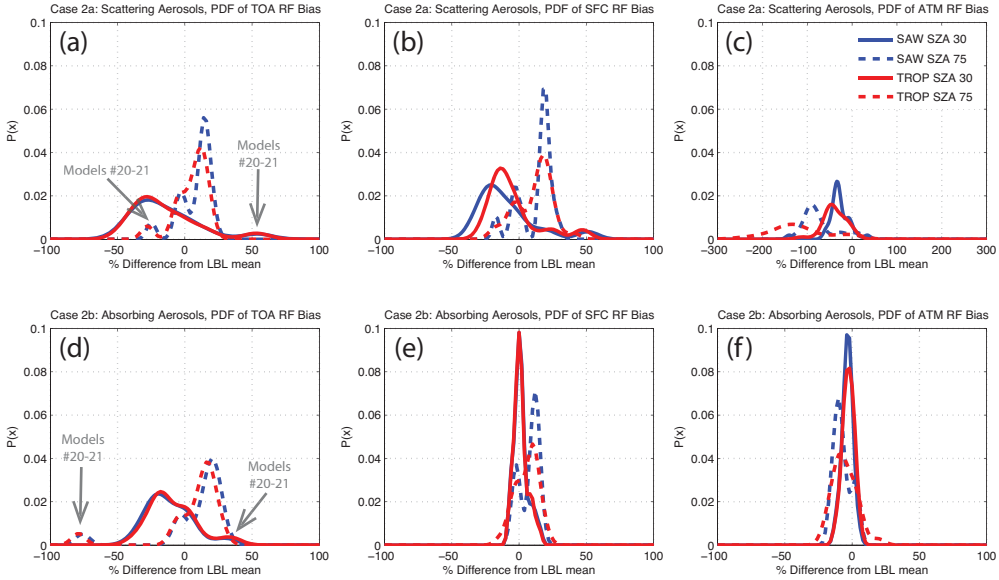

Fig. 7. For each solar zenith angle and prescribed atmosphere combination, the probability density function P(x) for **(a)** scattering aerosol (Case 2a) TOA RF bias, **(b)** scattering aerosol (Case 2a) SFC RF bias, **(c)** scattering aerosol (Case 2a) ATM RF bias, **(d)** absorbing aerosol (Case 2b) TOA RF bias, **(e)** absorbing aerosol (Case 2b) SFC RF bias, and **(f)** absorbing aerosol (Case 2b) ATM RF bias. Biases are calculated as the percent deviation of each non-LBL model from the LBL mean: Bias = $100 \times \frac{\mu_{\text{model}} - \mu_{\text{LBL}}}{\mu_{\text{LBL}}}$ where μ is the mean. Negative biases imply too much radiative cooling or too little radiative warming; positive biases imply too little radiative cooling (too much radiative warming). The small peaks in the PDF are from Models #20 and 21 which use the Eddington approximation (as opposed to the δ-Eddington approximate used in the counterpart Models #22 and 23).

Myhre et al. (2013), reported as clear-sky (cloud-free) TOA and ATM normalized radiative forcing efficiency (NRF), can be compared to the results from this study for the absorbing aerosol case. Note that the results from Myhre et al. (2013) (a) are global averages (diurnal and zenith-angle averaged) and (b) have varying host-model treatment of, for example, surface albedo and atmospheric gases. The NRF is defined as TOA and SFC radiative forcing divided by AOD or the ATM radiative forcing divided by the absorption optical depth (AAOD = (1 − SSA) × AOD). Clear-sky global average results from the AeroCom Prescribed Experiment (Stier et el., 2012), which included 8 models using similar or identical radiation schemes to those included in this study, are even more comparable to results reported here. Specifications for aerosol properties in FIX2–FIX0 and FIX3–FIX0 are identical to Case 2a (Scattering Aerosols) and Case 2b (Absorbing Aerosols), respectively. However, in Stier et el. (2012) surface albedo and Rayleigh scattering are different for each model, and results are for global average conditions (diurnal, solar-zenith angle averaged). Note that in both this study and Stier et el. (2012) AOD is 0.2 and and AAOD is 0.04; these optical properties varied by model in Myhre et al. (2013).

Figure 8 summarizes overlapping aerosol radiative forcing results from the AeroCom Phase II experiments. Models that use similar radiation schemes have the same colored bar, and the benchmark average LBL radiative forcing (black bars with ± 1 standard deviation error bars) is given for this study. Table A5 gives the model name and number from this study and the corresponding model names from Stier et el. (2012) and Myhre et al. (2013).

Figure 8a and c summarize the TOA and SFC NRF for Case 2a (Scattering Aerosols) and its analog (FIX2–FIX0) from the Prescribed Experiment. The mean (RSD) of the eight models from the Prescribed Experiment (FIX2–FIX0) are $-36.6\,\mathrm{W\,m^{-2}}$ (6.0 %) and $-37.7\,\mathrm{W\,m^{-2}}$ (8.4 %) for TOA and SFC NRF, respectively. For these same radiation schemes in the current study, the mean TOA NRF ranges from ∼-47 to $-84\,\mathrm{W\,m^{-2}}$, increasing in magnitude with increased SZA. The RSD ranges from ∼8 to 18 %, increasing with decreased SZA. As solar zenith angle increases, surface NRF increases in magnitude by a factor of 1.7, and the RSD ranges are roughly the same as the TOA NRF.

For the scattering aerosol case, note that Fig. 8b shows the ATM RF, rather than the normalized atmospheric radiative forcing because AAOD = 0. Though aerosol absorption is defined as zero for the simulations considered here (SSA = 1.0), aerosol scattering can enhance molecular absorption by increasing the photon path-length (Stier et el., 2012). For both

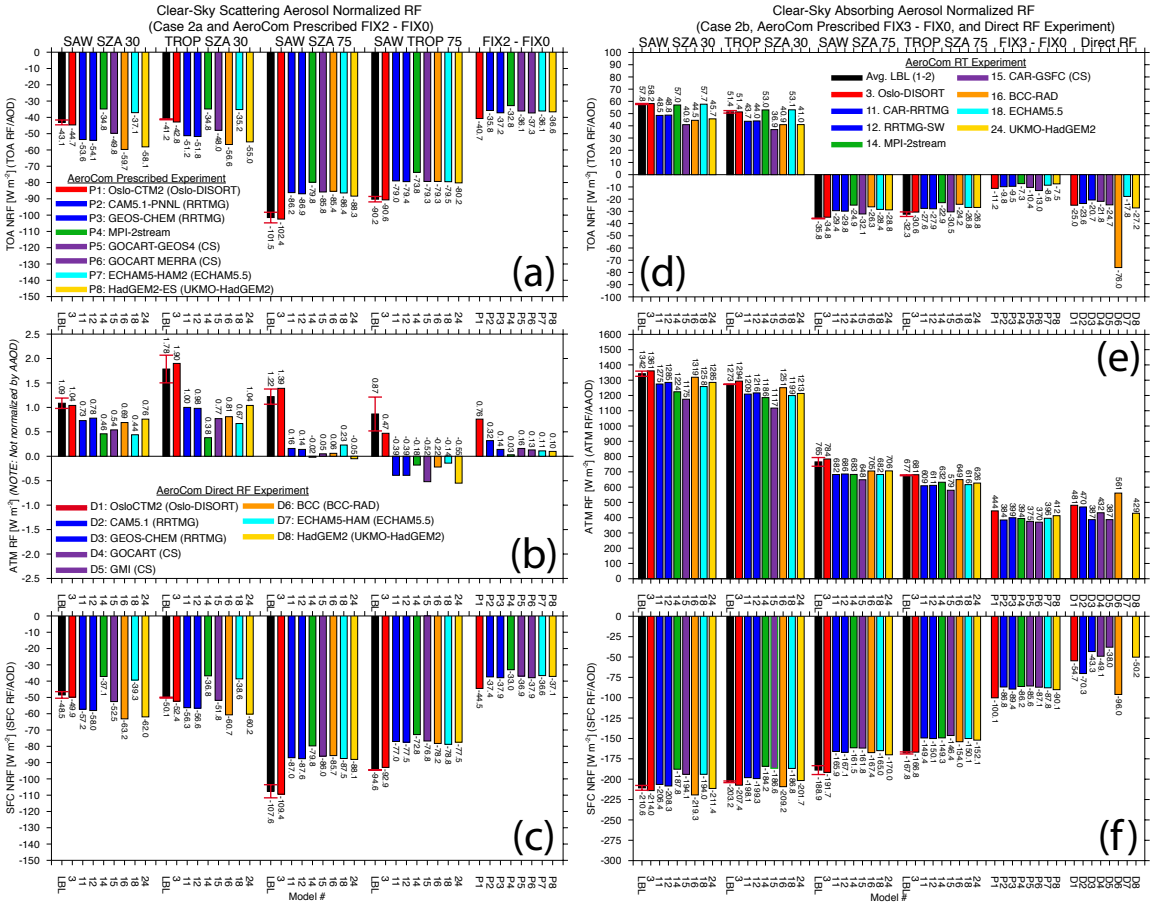

Fig. 8. Summary of clear-sky (cloud-free) aerosol direct normalized radiative forcing (NRF) from the present study (AeroCom Radiative Transfer Experiment), the AeroCom Prescribed Experiment (Stier et el., 2012), and the AeroCom Direct Radiative Forcing Experiment (Myhre et al., 2013). NRF is defined as the TOA and SFC RF divided by the AOD and the ATM RF divided by the absorption optical depth (AAOD = (1−SSA)×AOD). Results from Stier et el. (2012) and Myhre et al. (2013) are from Table 3 of each study. Models which use similar radiative transfer schemes have the same color bar. **(a)** Comparison of TOA NRF results from Case 2a (Scattering Aerosols) versus the FIX2–FIX0 (Stier et el., 2012); aerosol properties in these two studies are identical (AOD = 0.2, SSA = 1.0) except in Stier et el. (2012) host models simulate their own surface albedo and gaseous absorbers. Also, the results for FIX2–FIX0 are global and diurnal average results. **(b)** Comparison of ATM RF results from Case 2a (Scattering Aerosols) versus FIX2–FIX0. Note: We do not show normalized atmospheric radiative forcing because the AAOD is zero in the scattering aerosol case. Non-zero ATM RF in the scattering case results from enhanced molecular absorption due to aerosol scattering as described in the text. **(c)** Comparison of SFC NRF from Case 2a and FIX2-FIX0. **(d–f)** Comparison of TOA, ATM, and SFC NRF results from Case 2b (Absorbing Aerosols) versus the global average result from FIX3-FIX0 (Stier et el., 2012), which also has the same specified aerosol optical properties (but not the same albedo or gaseous absorbers; AOD = 0.2, AAOD = 0.04). We also include results from the AeroCom Direct Radiative Forcing Experiment (Myhre et al., 2013). Note that in the global and diurnally averaged results in Myhre et al. (2013), models are run in their standard configuration, simulating all included aerosol processes. The mean SSA for the eight models here was 0.941 with a standard deviation of 0.02, and the mean global AOD was 0.0245 with a standard deviation of 0.008 (Table 3; Myhre et al., 2013).

studies, the RSD in atmospheric radiative forcing is largest (e.g. 47 % at 30°). In this study, the mean ATM RF is slightly positive (more positive at lower SZA) for the eight models overlapping with Stier et el. (2012). Stier et el. (2012) indicates a mean ATM RF of 0.2 $W m^{-2}$ with a large RSD.

In both this study and the Prescribed Experiment, Oslo-DISORT (Model #3, OsloCTM2 in Stier et el., 2012) exhibits the strongest absorption enhancement in the scattering-only aerosol case. However, the ATM RF of Model #3 (a multi-stream model) has the best agreement with the mean LBL result. In the two-stream version of this model (Oslo-2stream, Model #4; see Fig. 5), the ATM NRF is reduced by roughly 30 to 110 % at lower and higher SZA, respectively. We also note that Oslo-DISORT has a low spectral resolution (4 shortwave bands, Table 1), and enhanced molecular absorption due to O_3 may be larger as a result (Stier et el., 2012).

The mean (RSD) of the eight models from the Prescribed Experiment (FIX3–FIX0) are $-9.7\,W m^{-2}$ (19.7 %), $397\,W m^{-2}$ (5.9 %), and $-89.1\,W m^{-2}$ (5.3 %) for TOA, ATM, and SFC NRF, respectively. Note that in Stier et el. (2012), models can have different surface albedos, and differences in the resulting path-length can contribute to the diversity in atmospheric absorption at the TOA. For the analog Case 2b (Absorbing Aerosols; Fig. 8d–f), the TOA NRF RSD for these same eight radiation schemes ranges 10 to 14 %, increasing with decreased SZA. The mean TOA NRF is $48.6\,W m^{-2}$ at 30° and $-28.7\,W m^{-2}$ at 75°. In this study, atmospheric NRF averages $659\,W m^{-2}$ at 75° and $1236\,W m^{-2}$ at 30°. The RSD for ATM NRF (8 and 5 % at each of these solar zenith angles, respectively) is lower compared to the scattering-only case, consistent with the results of Stier et el. (2012). The RSD for SFC NRF in Case 2b is roughly equivalent to the atmospheric values.

We now consider radiation schemes that were also involved in the AeroCom Direct Radiative Forcing Experiment (Myhre et al., 2013). While it is generally difficult to scale the uncertainties in aerosol radiative forcing under idealized conditions to uncertainties in diurnal-averaged global estimates of aerosol radiative effects, this comparison allows us to examine how these radiation schemes perform at given solar zenith angles and atmospheric conditions that may be representative of daily averaged forcing for a given region. Considering schemes also used in Myhre et al. (2013), the TOA normalized forcing diversity (RSD) is roughly 10 to 14 % for Case 2b (Absorbing Aerosols) and the mean TOA NRF is ~ 47 and $-29\,W m^{-2}$ at lower and higher SZA, respectively. SFC and ATM NRF model diversity ranges between 5 and 8 % (increasing with SZA). We compare Case 2b results to clear-sky results from the Direct RF experiment, which have an average SSA of 0.94 (i.e. less absorbing than Case 2b). After having first simulated the full aerosol life-cycle, the Direct RF models exhibits relatively good agreement in atmospheric normalized radiative forcing (RSD$\sim$14 %; mean $450\,W m^{-2}$). However, there is a large range in TOA NRF ($\sim$-18 to $-76\,W m^{-2}$; mean $-29.6\,W m^{-2}$; RSD 64 %) and SFC NRF (~ -38 to $-96\,W m^{-2}$; mean $-57.4\ W m^{-2}$; RSD 35 %). Thus all three AeroCom studies indicate lower inter-model diversity in simulating atmospheric absorption when more absorbing aerosols are considered. The higher RSD in surface NRF in Myhre et al. (2013) may reflect the use of geographic and model-dependent surface albedo.

4 Conclusions

In this study we examine the performance of multi- and two-stream radiative transfer schemes used in global climate models relative to reference data from high spectral resolution multi-angular methods. We examine the models in a controlled sense by prescribing both gaseous absorbers (water vapor and ozone) and simple aerosol optical properties (separately, scattering-only and more absorbing aerosols) with fixed surface albedo. Results are compared as a function of solar zenith angle and increasing trace gas amount.

Comparisons in clear-sky (aerosol- and cloud-free) Rayleigh atmosphere conditions of solar atmospheric transmissions indicate significant model bias from the reference line-by-line calculation (up to 6 % at high solar zenith angle in humid conditions for the near-IR). This identifies deficiencies particularly in the representation of absorption by atmospheric water vapor. Diversity amongst models, quantified as the standard deviation as a percentage of the mean or relative standard deviation, is on the order of 2 to 4 % for wavelengths where gaseous absorption is prominent (near-IR), and this diversity increases as water vapor slant path increases (or, as SZA increases). In the Rayleigh atmosphere case, the largest model diversity occurs in the partitioning of total flux into direct and diffuse components.

In order to isolate the treatment of multiple scattering and absorption by aerosols, we computed the broadband solar top of the atmosphere aerosol radiative forcing. In the computation of forcing, a second call is made to the radiation models, now with prescribed aerosol optical properties, and fluxes at the TOA are differenced relative to the Rayleigh atmosphere case. The diversity amongst models in the TOA forcing is largest for purely scattering aerosols at low SZA (15 %) and decreases with increasing SZA. Increased aerosol absorption decreases the diversity in atmospheric and surface radiative forcing. This indicates that the treatment of multiple scattering contributes to the large inter-model diversity in top of the atmosphere aerosol radiative forcing, and this diversity may be important given the regionally diverse absorption characteristics of global aerosols.

When considering solar top of the atmosphere (TOA) radiative forcing by aerosols, deficiencies in gaseous transmission are less important than the treatment of multiple scattering. Relative to benchmark multi-directional line-by-line results, when scattering-only aerosols are considered, simpler two stream models over- and underestimate TOA aerosol

radiative cooling as SZA increases. Two-stream models underestimate the magnitude of radiative warming and cooling at lower and higher SZA when absorbing aerosols are considered. The bias in aerosol radiative forcing for the models in this study is on the order of 10-20 %, with the highest bias occurring when considering scattering aerosols at lower SZA.

We considered solar zenith angles more representative of the tropics (30°) and high latitudes (75°) following Halthore et al. (2005). A previous study (Russell et al., 1997) indicated that aerosol radiative forcing may peak somewhere in between these angles (specifically, around 60° for mostly scattering aerosol due to the competition between path length and available sun energy). Thus, biases reported in this study may be mitigated in the global average. Indeed, the inter-model diversity reported in this study for the two specific zenith angles is generally higher than those reported for global, diurnally-averaged conditions (Myhre et al., 2013) even when the same aerosol optical properties are prescribed (Stier et el., 2012). Though biases may be larger when considering specific zenith angles, we note that all three AeroCom studies indicate decreased inter-model diversity in atmospheric radiative forcing as aerosol absorption increases. Further, both Stier et el. (2012) and this work show that atmospheric absorption is enhanced when considering scattering-only aerosol because the increased photon path-length increases molecular absorption, particularly by ozone.

For daily forcing simulations, biases in radiative forcing indicate that there is a tendency by the two-stream models to under- and overestimate the magnitude of aerosol forcing for absorbing and scattering-only aerosols, respectively, at low latitudes (with predominantly low solar zenith angles during the day). At high latitudes (with predominantly high solar zenith angles during the day), scattering-only and absorbing aerosols both underestimate the magnitude of aerosol radiative cooling. It is important to note that computational limitations often prevent the use of multi-stream radiative transfer schemes in global aerosol modeling. Delta-scaling serves to somewhat mitigate the accuracy sacrificed by two-stream models in their representation of the phase function. Furthermore, from a climatological perspective, daily biases introduced by two-stream schemes may partially compensate one another when computing a global average radiative forcing. However, regionally and seasonally they may introduce systematic errors that can significantly impact aerosol climate effects.

This study has presented an intercomparison of global aerosol model radiative transfer schemes using common idealized aerosol properties. We have shown that, assuming aerosol properties are perfectly known, the bias in aerosol radiative forcing is sensitive to the solar zenith angle. Yet, it is expected that inter-model differences in simulating aerosol properties (e.g. AOD, SSA) would likely introduce biases in radiative forcing of greater magnitude than presented here. Global observations of AOD have served to reduce inter-model diversity in simulated AOD (e.g. Textor et al., 2006, 2007). An observing system that helps to better constrain the diurnal variation of aerosol optical properties would enable global aerosol models to converge to a better representation of these properties as a function of zenith angle and hence a better estimate of aerosol radiative forcing. The smaller biases introduced by the use of two-stream radiation schemes can be mitigated by future advances in computational power that will allow multi-stream schemes to operate on-line within global aerosol models.

Appendix A

Radiative transfer scheme descriptions

We provide brief descriptions of the models used in this intercomparison; model characteristics are summarized in Table 1 and Appendix Table A1. We refer the reader to seminal works for details on radiative transfer theory and methods for solving the transfer equation (e.g., Chandrasekhar, 1960; van de Hulst, 1980; Lenoble, 1985; Liou, 1992). Models in the appendix are arranged by model # from Table 1 with the names of contributing investigators given in parenthesis.

A1 Models #9, 11, 15, 17, 25, 26 and 29: Cloud-Aerosol-Radiation model (CAR; *F. Zhang*)

The Cloud-Aerosol-Radiation (CAR) Ensemble Modeling System currently incorporates 7 major cloud-aerosol radiation packages used in major research institutions worldwide: CAM (NCAR), RRTMG (NCEP, ECMWF, and future NCAR), GFDL (NOAA), GSFC (NASA), CCCMA (Canada), CAWCR (Australia), and FLG (popular for DOE/ARM). A general model description and basic skill evaluation of the CAR system is found in Liang and Zhang (2012); Zhang et al. (2013) and can also be found at http://car.umd.edu. For each radiative transfer code, radiative processes such as gaseous absorption and absorption and scattering by clouds and aerosol particles can be easily included or excluded depending on the aim of the study. Strikingly, cloud and aerosol properties can be decoupled from the radiative transfer calculation, making CAR a useful tool for the intercomparison of different cloud, aerosol and radiation schemes. See additional descriptions of each radiation scheme in CAR used in this intercomparison according to model number from Table 1.

A2 Model #1 GENLN2-DISORT (*G. Myhre*)

GENLN2-DISORT is the GENLN2 (Edwards, 1992) line-by-line (LBL) model coupled to a discrete-ordinate method (DISORT; Stamnes et al., 1988) for calculation of radiative fluxes. The model has been used for radiative transfer calculation in the solar spectrum previously (Myhre et. al., 2002) and in an intercomparison study (Forster et al., 2011). The

Table A1. Gaseous transmission schemes: #*k*- or ESFT terms for ozone and water vapor[a]

Model #	Model Name	Type	# O_3	# H_2O
1	GENLN2-DISORT	LBL	–	–
2	RFM DISORT (RFMD)	LBL	–	–
3	Oslo-DISORT	ESFT	2	2–3
4	Oslo-2Stream	ESFT	2	2–3
5	UNIVIE-Streamer	ESFT	0–30 terms/band	0-30 terms/band
6	FMI-libRadtran	*ck*-D	123	30
7	LMU-libRadtran	*ck*-D	123	30
8	GSFC-FL	*ck*-D	10	54
9	CAR-FLG	*ck*-D	10	44
10	LaRC-FL	*ck*-D	10	60
11	CAR-RRTMG	*ck*-D	28	92
12	RRTMG-SW	*ck*-D	28	92
13	LMU-2stream	*ck*-D	123	30
14	MPI-2stream	*ck*-D	9	41
15	CAR-GSFC	*k*-distribution	8	31
16	BCC-RAD	*ck*-D	15	13
17	CAR-CCCMA	*ck*-D	9	23
18	ECHAM5.5	Padé approximation	1	1
19	UMD-SRB	*k*-distribution for H_2O Lacis and Hansen (1974) for O_3	–	40
20	ES96-6	*ck*-D	6	15
21	ES96-220	*ck*-D	0–24/band	0–25/band
22	ES96-6-D	*ck*-D	6	15
23	ES96-220-D	*ck*-D	0–24/band	0–25/band
24	UKMO-HadGEM2	*ck*-D	6	15
25	CAR-CAWCR	ESFT	8	13
26	CAR-CAM	ESFT	7	7
27	ULAQ	ESFT	150	85
28	FORTH	ESFT	high spectral resolution for O_3 photolysis rates	67
29	CAR-GFDL	ESFT	14	25
30	MPI-MOM	*ck*-D	9	41
31	MOMO	non-correlated *k*	120	3000

[a] Abbreviations: LBL = line-by-line, DISORT = discrete-ordinate method, ES96 = Edwards and Slingo (1996), ESFT = exponential sum fit transmission, *ck*-D = correlated *k*-distribution

GENLN2 LBL code is updated with absorption data from the HITRAN-2008 database (Rothman et al., 2009). Absorption by H_2O, CO_2, O_3, O_2, and CH_4 has been included in the simulations. The spectral resolution in the computations was $0.02\,cm^{-1}$. The extraterrestrial spectral solar irradiance had a 1 nm resolution from Lean et al (2005) in simulations and the full spectral region considered has been from 0.2 µm to 5.0 µm. For this intercomparison the radiative fluxes were computed using 16 streams in the DISORT code.

A3 Model #2 RFM DISORT (RFMD; *E. Highwood, C. Ryder, B. Harris*)

RFM DISORT is the Reference Forward Model (RFM), a line-by-line radiative transfer model, coupled to a discrete ordinate method (DISORT; Stamnes et al., 1988) for scattering calculations. RFM has been developed at Oxford University, UK (http://www.atm.ox.ac.uk/RFM/) and is based on the GENLN2 model (Edwards, 1992). The spectral resolution used was $1\,cm^{-1}$, covering wavelengths from 0.2 to 10 microns with 4 streams in DISORT. The HITRAN 2004 database (Rothman et al., 2005) is used for gaseous absorption coefficients.

A4 Model #3 Oslo-DISORT (*G. Myhre*)

The Oslo-DISORT code uses the discrete-ordinate method (DISORT) (Stamnes et al., 1988) specifically designed for calculations of atmospheric aerosols. The model has a high number of streams (8), but a low spectral resolution

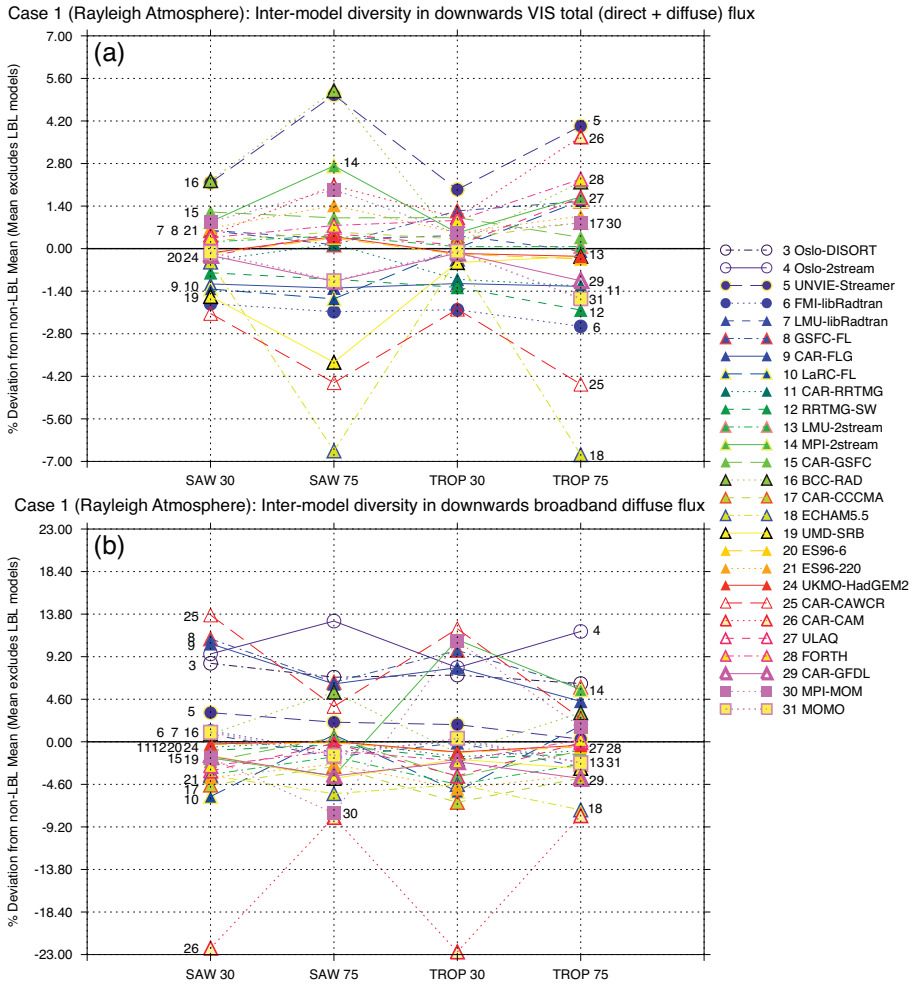

Fig. A1. Inter-model diversity in UV-VIS and broadband diffuse flux down at the surface for the Rayleigh atmosphere (Case 1) expressed as a percent deviation from the non-LBL model mean (i.e. the mean from all models excluding #1, 2, 22 and 23). Note that Models #22–23 are the same as #20-21 in Case 1. As a function of standard atmosphere and solar zenith angle: **(a)** downwards UV-VIS at the surface and **(b)** downwards diffuse broadband flux. Appendix Figures A2 and A3 show the bias of UV-VIS and broadband diffuse down fluxes relative to the LBL benchmarks, respectively.

(4 bands), with the main emphasis on wavelengths below 1.5 µm. The spectral regions are 0.3–0.5 µm, 0.5–0.85 µm, 0.85-1.5 µm, and 1.5–4.0 µm. The absorption by water vapor and ozone is taken into account by the exponential-sum fitting method (ESFT, Wiscombe and Evans, 1977). The number of exponential-sum fitting terms for each spectral region is two or three. Higher accuracy can be obtained with a higher number of exponential-sum fitting terms, but this increases the computational time. The GENLN2 line-by-line model (Edwards, 1992) is used to calculate the transmission data for water vapor with spectroscopic data from the HITRAN92 database (Rothman et al., 1992). Cross-sections for ozone in the ultraviolet and visible region are from WMO (1985). Oslo-DISORT has been validated against the GENLN2-DISORT LBL model for various cases for aerosols with agreement within 10 % (Myhre et. al., 2002).

A5 Model #4 Oslo-2stream (*G. Myhre*)

2-stream version of Oslo-DISORT (Model #3; see above).

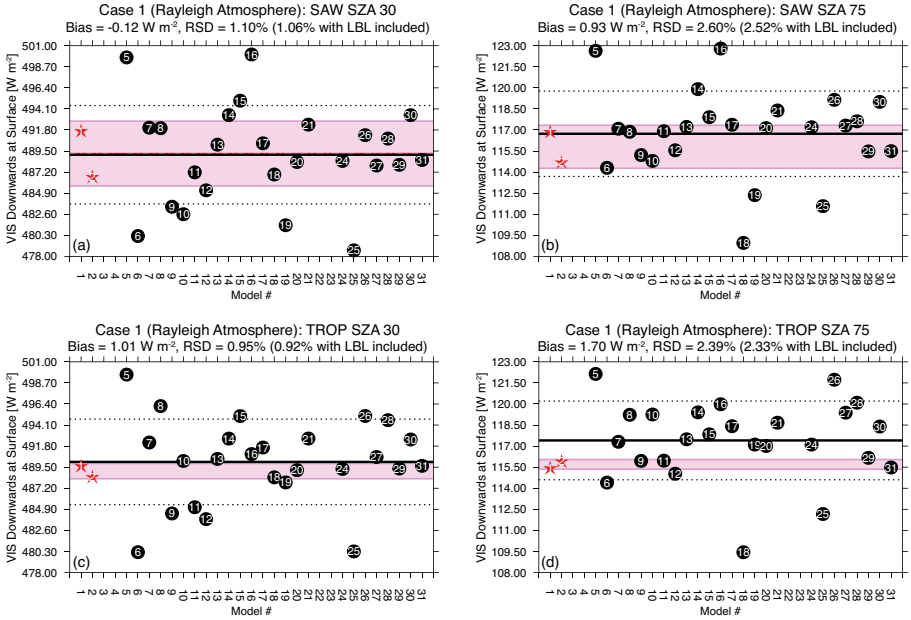

Fig. A2. UV-VIS flux down at the surface in Case 1 (Rayleigh atmosphere) for **(a)** SAW 30°, **(b)** SAW 75°, **(c)** TROP 30°, and **(d)** TROP 75°. LBL results are given as stars; non-LBL models are black circles. The pink shading indicates ±1 standard deviation from the LBL mean. The non-LBL mean is given as the thick black line with ±1 standard deviation indicated by dotted black lines. The model bias relative to the LBL-mean is given as well as the relative standard deviation (RSD) excluding (and in parenthesis including) the LBL models. See Appendix Table A2 for additional statistics.

A6 Model #5 UNIVIE-Streamer (*D. Neubauer, R. Hitzenberger*)

Streamer (Key and Schweiger, 1998) is a radiative transfer model employing the discrete-ordinate (DISORT) method (Stamnes et al., 1988) to solve the radiative transfer equation. We have modified Streamer to increase the spectral range for radiative transfer calculations and to include additional scattering and absorbing gases (Neubauer et al., 2011). The modified model UNIVIE-Streamer accounts for absorption by atmospheric gases using exponential fits (Wiscombe and Evans, 1977) to the LOWTRAN7 (Kneizys et al., 1988) and LBLRTM (Clough et al., 2005) transmittances. In all cases 8 streams and 24 unequal spectral intervals in the solar range 0.2–5.0 µm and 10 bands in the UV/visible range 0.2–0.69 µm were used for computing fluxes. Aerosol optical properties were computed separately using Mie theory for 60 wavelengths (7 in the UV/visible range). Note that the number of ESFT terms varies between 0 and 30 for each spectral band and each atmospheric gas.

A7 Model #6 FMI-libRadtran (*J. Huttunen*)

The Finnish Meteorological Institute version of libRadtran (FMI-libRadtran, Mayer and Kylling, 2005) uses 8-streams and the DISORT2 solver. Delta-M scaling is switched on. Solar spectral irradiance is taken from Gueymard (2004).

A8 Model #7 LMU-libRadtran (*B. Mayer*)

The Ludwig-Maximilians-Universitaet version of libRadtran (Mayer and Kylling, 2005) uses 6-streams, the discrete-ordinate method (DISORT2) for calculation of radiative fluxes, and a plane-parallel atmosphere assumption. Molecular absorption is treated with a *k*-distribution of 32 bands (Kato et al., 1999). The shortwave (SW) bands are the sum of bands 1–32 (240.1–4605.7 nm). The visible (VIS) bands are the sum of 16 bands (204.1–704.4 nm).

A9 Model #8 GSFC Fu-Liou Radiative Transfer Model (GSFC-FL; *H. Yu*)

The Fu-Liou model used by the NASA Goddard Space Flight Center (GSFC) group is a broadband radiative transfer model with a delta-four-stream approximation (Fu and Liou, 1992, 1993). The model accounts for solar radiation over 0.2–4.0 µm range with 6 bands. The first band in the UV-visible (0.2–0.7 µm) is divided into 10 subintervals where the spectral dependences of O_3 absorption and aerosol optical properties are incorporated explicitly. Absorption data for H_2O, O_2, and CO_2 are taken from HITRAN82

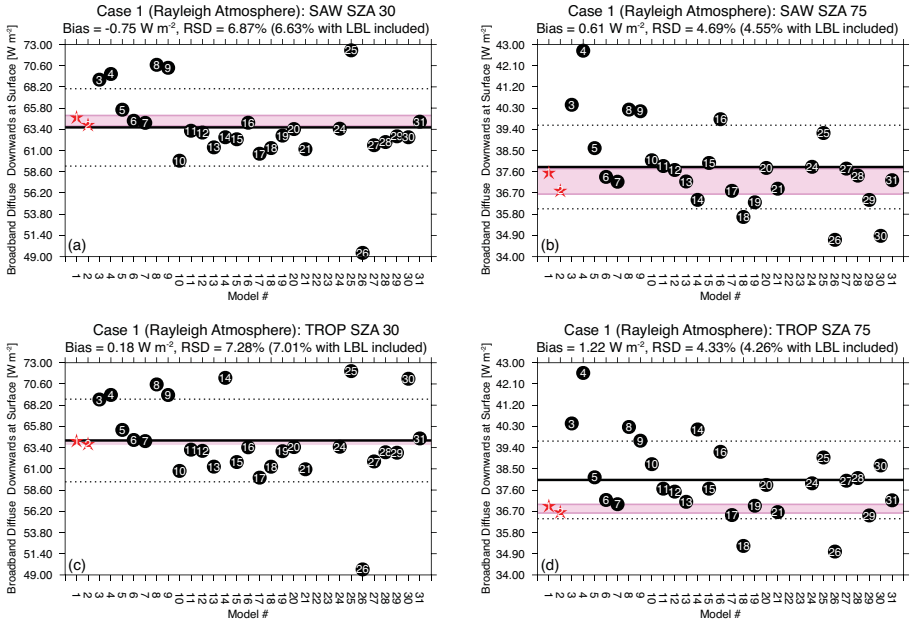

Fig. A3. The same as Fig. A2 except for broadband diffuse flux down at the surface in the Rayleigh atmosphere (Case 1). See Appendix Table A2 for additional statistics.

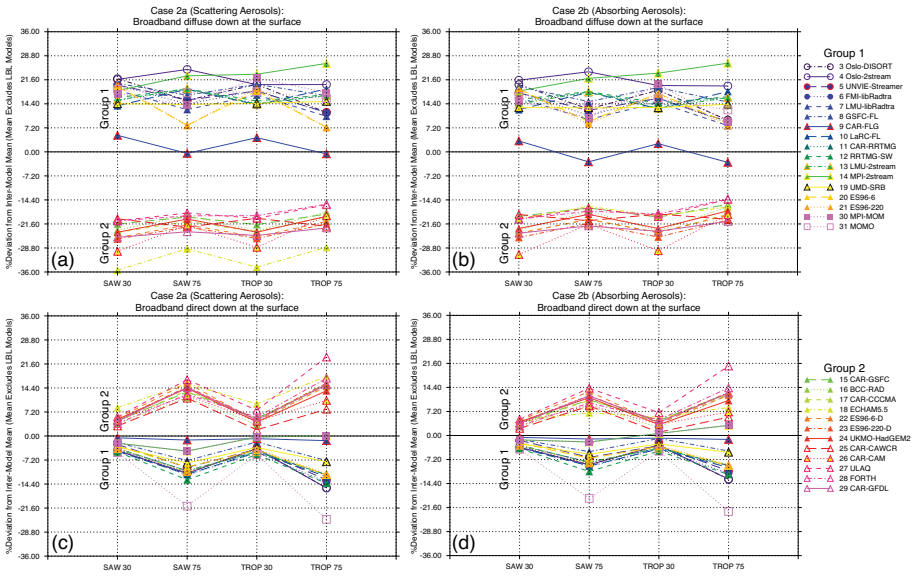

Fig. A4. Inter-model diversity in broadband diffuse and direct flux down at the surface expressed as a percent deviation from the non-LBL model mean (i.e. μ from all models excluding #1 and 2). As a function of standard atmosphere and solar zenith angle the broadband diffuse flux down at the surface is given for: **(a)** Case 2a (Scattering Aerosols) and **(b)** Case 2b (Absorbing Aerosols). Corresponding diversity for the broadband direct flux down at the surface is given for: **(c)** Case 2a (Scattering Aerosols) and **(d)** Case 2a (Absorbing Aerosols). Note that Fig. A4a is the same as Fig. 3.

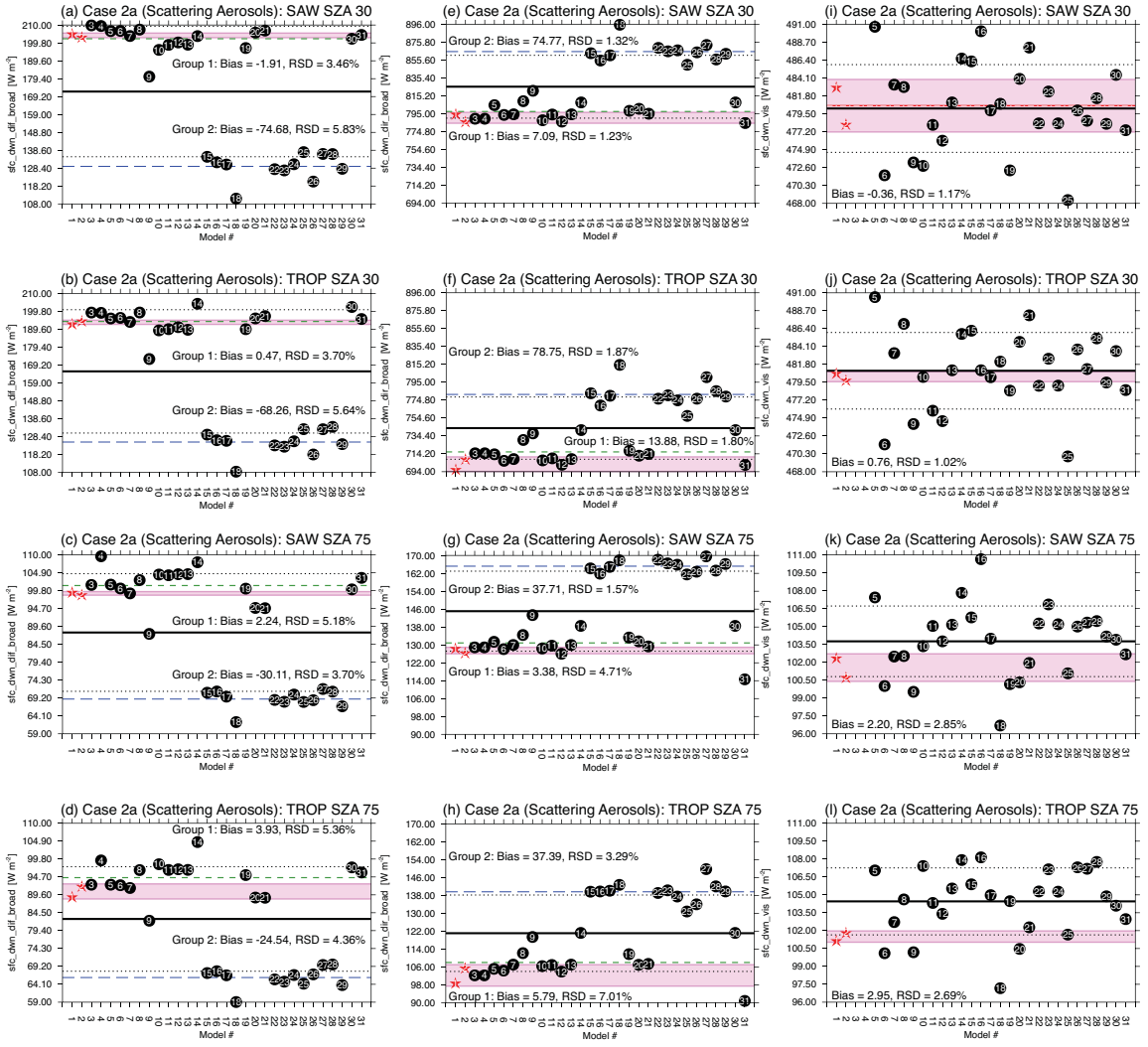

Fig. A5. Broadband diffuse **(a–d)**, broadband direct **(e–h)**, and UV-VIS (direct + diffuse) **(i–l)** flux down at the surface in Case 2a (Scattering Aerosols) as a function of atmosphere and solar zenith angle. LBL results are given as stars; non-LBL models are black circles. The pink shading indicates ±1 standard deviation from the LBL mean. The non-LBL mean is given as the thick black line with ± 1 standard deviation indicated by dotted black lines. For UV-VIS fluxes, the absolute model bias relative to the LBL-mean is given as well as the RSD excluding the LBL models. Green and blue lines indicate the multi-model averages for the groups described in Table 4 for broadband fluxes; statistics are given for each group. Group 1 (green) includes Models # 3–14, 19–21, and 30–31; Group 2 (blue) includes Models #15–18 and 22–29.

(Rothman et al., 1983) and that for O_3 are based on Howard et al. (1961). Rayleigh scattering is parameterized according to Slingo and Schrecker (1982). For this experiment, a total of 73 vertical layers are used, with a resolution of 1 km below 25 km and 2 km for altitudes of 26–120 km.

A10 Model #9 Fu-Liou-Gu radiation scheme (CAR-FLG, *F. Zhang*)

The Fu-Liou-Gu scheme (Gu et al., 2010, 2011; Liou et al., 2008) is a modified and improved version based on the original Fu-Liou scheme (Fu and Liou, 1992, 1993). The model calculates SW flux in a vertically inhomogeneous scattering-absorbing atmosphere using either a

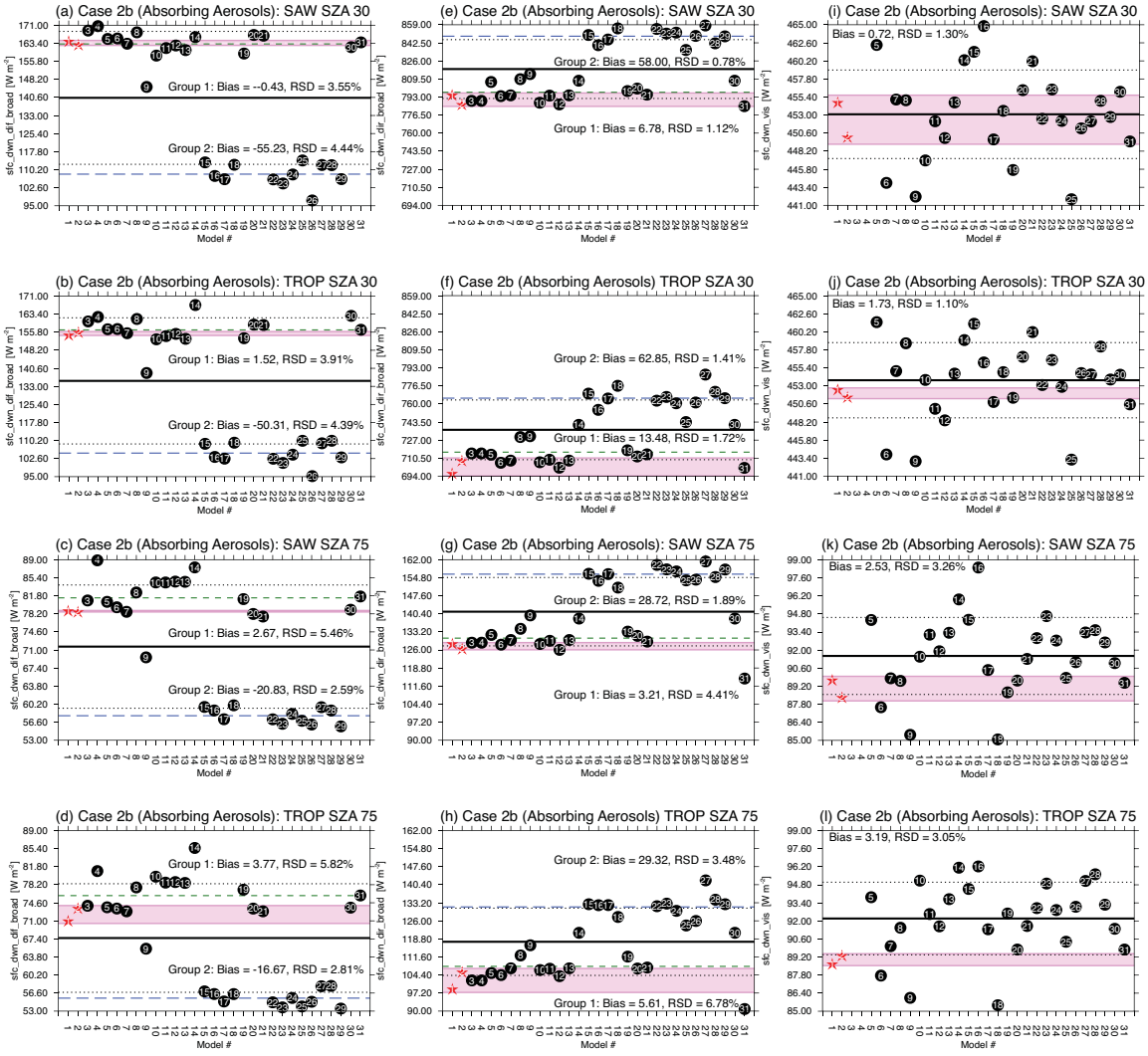

Fig. A6. The same as Fig. A5 except for Case 2b (Absorbing Aerosols).

delta-four-stream approximation or a delta-two-stream (Eddington) approximation. It and accounts for the absorption of all radiatively important gases using the correlated-*k* distribution method (*ck*-D) fits to the 1982 version of the AFGL data type (Fu and Liou, 1992) with some updates fits to HITRAN 2000 (Zhang et al., 2005). There are 6 solar bands with total 54 sub-spectra over 0.2∼4.0 µm. Modeled molecular absorbers in the solar bands are H_2O (including H_2O continuum absorption), O_3, CO_2, CH_4, N_2O, CO and O_2. Here, the four-stream method is used for this intercomparison.

A11 Model #10 NASA LaRC Fu-Liou RTM (LaRC-FL; *F. G. Rose, S. Kato*)

The NASA Langley (LaRC) Fu-Liou Radiative Transfer Model is a modified version based on the original Fu-Liou scheme (Fu and Liou, 1992, 1993). This scheme uses a two-stream delta-Eddington approximation to calculate shortwave flux and the correlated-*k* distribution method (*ck*-D) for gas absorption (coefficients based on HITRAN 2000 including SW continuum absorption). There are 18 shortwave bands (10 visible, 8 near-infrared) spanning the wavelength range 0.17–4.0 µm. The visible to near-IR split is located

Table A2. Case 1: summary of statistics for the Rayleigh atmosphere (excluding only models #22–23)[a, b, c]

	SAW		TROP	
	30° SZA	75° SZA	30° SZA	75° SZA
Direct Broadband Downwards Flux at Surface				
LBL Avg	942.4	216.2	844.5	179.6
LBL RSD	0.8 %	1.1 %	1.1 %	3.9 %
Model Avg.	947.4	218.8	858.1	186.9
Avg. Bias	0.5 %	1.2 %	1.6 %	4.0 %
Model RSD	0.8 %	2.6 %	1.5 %	4.6 %
Diffuse Broadband Downwards Flux at Surface				
LBL Avg	64.4	37.2	64.0	36.8
LBL RSD	0.9 %	1.5 %	0.4 %	0.5 %
Model Avg.	63.6	37.8	64.2	38.0
Avg. Bias	−1.2 %	1.6 %	0.3 %	3.3 %
Model RSD	6.9 %	4.7 %	7.3 %	4.3 %
Diffuse Broadband Flux Up at TOA				
LBL Avg	227.6	82.6	204.7	75.2
LBL RSD	1.3 %	1.5 %	1.3 %	1.8 %
Model Avg.	230.8	84.0	211.4	78.4
Avg. Bias	1.4 %	1.7 %	3.3 %	4.2 %
Model RSD	1.1 %	1.8 %	2.5 %	3.2 %
Total (Direct + Diffuse) UV-VIS Downwards Flux Down at Surface				
LBL Avg	489.2	115.8	489.1	115.7
LBL RSD	0.7 %	1.3 %	0.2 %	0.3 %
Model Avg.	489.1	116.7	490.1	117.4
Avg. Bias	0.0 %	0.8 %	0.2 %	1.5 %
Model RSD	1.1 %	2.6 %	1.0 %	2.4 %
Total near-IR Downwards Flux at Surface[d]				
LBL Avg	519.1	138.0	421.1	101.1
LBL RSD	0.8 %	1.0 %	2.3 %	6.5 %
Model Avg.	522.9	139.9	432.6	108.2
Avg. Bias	0.7 %	1.4 %	2.7 %	7.0 %
Model RSD	1.9 %	3.9 %	3.8 %	7.5 %
Broadband Absorptance[e]				
LBL Avg	0.134	0.201	0.221	0.307
LBL RSD	7.2 %	6.4 %	2.5 %	5.1 %
Model Avg.	0.126	0.186	0.201	0.273
Avg. Bias	−6.1 %	−7.6 %	−8.8 %	−11.1 %
Model RSD	4.9 %	7.6 %	6.2 %	8.9 %

[a] Flux units W m^{-2}; scaled normalized results as described in the text and Fig. 2. Only Models 22 and 23 are excluded because they are the same as Models 20 and 21 in the Rayleigh atmosphere.
[b] Line-by-line (LBL) benchmarks (Avg. of Models #1 and #2) and non-LBL model results.
[c] Avg. Bias is expressed as a percentage of the LBL Avg. RSD = standard deviation as a percentage of mean.
[d] Near-IR is calculated as a difference between broadband and UV-VIS.
[e] Absorptance (Eq. 1) is derived assuming $F^{\uparrow}_{SFC} = \alpha F^{\downarrow}_{SFC}$ and surface albedo $\alpha = 0.2$.

at 14 500 cm^{-1} (0.6896 µm). The code was modified from the original Fu-Liou code to improve treatment of Rayleigh scattering and gas absorption. While two-streams were used for this intercomparison, the code can also be configured for four-streams and gamma-weighted two-streams. The vertical resolution was 32 layers, with 1-km resolution in the troposphere (below 25 km). Between 25 and 65 km, we interpolated online to 5 km vertical resolution using the natural log of pressure.

A12 Models #11 CAR-RRTMG (*F. Zhang*) and #12 RRTMG-SW (*L. Oreopoulos, D. Lee*)

RRTMG-SW (http://rtweb.aer.com/rrtm_frame.html) is a solar radiative transfer model that utilizes the correlated-*k* (*ck*-D) approach to treat gaseous absorption and to calculate shortwave fluxes and heating rates efficiently and accurately in a large-scale model environment (Clough et al., 2005; Iacono et al., 2008). Modeled sources of extinction are water vapor, carbon dioxide, ozone, methane, oxygen, nitrogen, aerosols, clouds, and Rayleigh scattering. The solar spectrum, 0.2–12 µm, is divided into 14 bands and spectral extinction integration within each band is accomplished using a variable number of g-points that add to 112 g-points for the entire solar spectrum. Absorption coefficient data for *ck*-D are obtained directly from the line-by-line radiative transfer model, LBLRTM, which has been extensively validated against observations, principally at the ARM SGP site. Scattering is treated using the delta-Eddington flavor (Joseph et al., 1976) of the two-stream approximation (Meador and Weaver, 1980; Oreopoulos and Barker, 1999).

The last solar band 820–2600 cm^{-1} is coded out of sequence to preserve spectral continuity with the longwave bands. For the visible/UV calculations of this paper the normalized fluxes either included band 9 (12 850–16 000 cm^{-1} or 0.625–0.778 µm) or were only integrated up to 0.625 μm; contributors Oreopoulos and Lee (Model #12) provide results for both, which are averaged in the intercomparison.

A13 Model #13 LMU-2stream (*B. Mayer*)

This is a version of libRadtran that uses a two-stream delta-Eddington radiative transfer solver rather than DISORT. Gaseous transmission is the same as in LMU-libRadtran (Model #7).

A14 Model #14 MPI-2stream (*S. Kinne*)

The Max Plank Institute for Meteorology model computes radiative fluxes with a two-stream method (e.g., Meador and Weaver, 1980) for the solar and infrared spectral region. This necessitates repeated applications (ca. 120 times) to properly approximate the spectral variability of atmospheric particle properties (via 8 solar and 12 infrared spectral sub-bands) and of major trace-gases (O_3, CO_2, CO, N_2O, and CH_4 – through a number of exponential terms in each of the sub-bands). The trace gas absorption (including water vapor) in the near-IR is based on LOWTRAN-5 data and ozone absorption data are based on Vigroux (1953). Trace-gases were

Table A3. Case 2a: summary statistics for scattering aerosols[a,b,c]

	SAW 30° SZA	SAW 75° SZA	TROP 30° SZA	TROP 75° SZA
Total (Direct + Diffuse) Brodband Flux Donwards at Surface				
LBL Avg.	994.6	226.5	896.0	192.8
LBL RSD	0.7 %	0.9 %	1.1 %	3.6 %
Model Avg.	996.9 (997.7)	232.6 (233.0)	906.1 (908.7)	202.7 (203.8)
Avg. Bias	0.2 % (0.3 %)	2.7 % (2.8 %)	1.1 % (1.4 %)	5.1 % (5.7 %)
Model RSD	0.8 % (0.9 %)	1.5 % (2.3 %)	1.0 % (1.6 %)	2.2 % (3.9 %)
Diffuse Broadband Flux Upwards at TOA				
LBL Avg.	236.3	102.9	212.9	93.2
LBL RSD	1.4 %	1.8 %	1.2 %	1.8 %
Model Avg.	240.2 (240.5)	102.8 (102.7)	219.3 (220.6)	95.0 (95.4)
Avg. Bias	1.7 % (1.8 %)	-0.1 % (-0.2 %)	3.0 % (3.6 %)	1.9 % (2.3 %)
Model RSD	1.3 % (1.2 %)	3.1 % (2.9 %)	1.7 % (2.3 %)	2.8 % (3.3 %)
Total UV-VIS Downwards Flux at Surface				
LBL Avg.	480.6	101.5	480.2	101.5
LBL RSD	0.7 %	1.1 %	0.1 %	0.5 %
Model Avg.	480.4 (480.2)	103.7 (103.8)	481.3 (481.0)	104.4 (104.5)
Avg. Bias	0.0 % (-0.1 %)	2.1 % (2.2 %)	0.2 % (0.2 %)	2.8 % (2.9 %)
Model RSD	1.1 % (1.2 %)	3.0 % (2.9 %)	1.0 % (1.0 %)	2.8 % (2.7 %)
Total Near-IR Downwards Flux at Surface[d]				
LBL Avg.	515.7	125.3	417.3	91.6
LBL RSD	0.8 %	0.6 %	2.4 %	7.0 %
Model Avg.	517.3 (518.6)	129.0 (129.3)	425.0 (428.4)	98.9 (100.0)
Avg. Bias	0.3 % (0.6 %)	2.9 % (3.2 %)	1.8 % (2.6 %)	8.0 % (9.2 %)
Model RSD	2.0 % (2.0 %)	2.5 % (3.7 %)	3.1 % (3.7 %)	3.8 % (7.2 %)

[a] Flux units W m^{-2}; scaled normalized results as described in the text and Fig. 2.
[b] Line-by-line (LBL) benchmarks (Avg. of Models #1 and #2) and non-LBL model results. As in Case 1, we exclude Models # 14, 25, 27, 30, and 31 for the model statistics; in parenthesis all models are considered.
[c] Avg. Bias is expressed as a percentage of the LBL Avg. RSD = standard deviation as a percentage of mean.
[d] Near-IR is derived as a difference between broadband and UV-VIS.

interpolated to the model resolution in the vertical using the log of pressure.

A15 Modle #15 GSFC radiation scheme (CAR-GSFC, *F. Zhang*)

The NASA GSFC radiation scheme includes the absorption due to water vapor, O_3, O_2, CO_2, clouds, and aerosols. Interactions among the absorption and scattering by clouds, aerosols, molecules (Rayleigh scattering), and the surface are fully taken into account. There are total 11 SW bands with 38 sub-spectra from 0.175 µm to 10 µm (Chou and Suarez, 1999). Depending upon the nature of absorption, different approaches are applied to different absorbers. In the ultraviolet (UV) and photosynthetically active (PAR) region, the spectrum is divided into 8 bands, and a single O_3 absorption coefficient and Rayleigh scattering coefficient are used for each band. In the infrared, the spectrum is divided into 3 bands, and the *k*-distribution method is applied with ten absorption coefficients used in each band. The flux reduction due to O_2 is derived from a simple function, while the flux reduction due to CO_2 is derived from precomputed tables. Reflection and transmission of a cloud and aerosol-laden layer are computed using the delta-Eddington approximation. Fluxes are then computed using the two-stream adding approximation. A special feature of this model is that absorption due to a number of minor absorption bands is included. Individually the absorption in those minor bands is small, but collectively the effect is large, ∼10 % of the atmospheric heating.

Table A4. Case 2b: summary of statistics for absorbing serosols[a,b,c]

	SAW 30° SZA	SAW 75° SZA	TROP 30° SZA	TROP 75° SZA
Total (Direct + Diffuse) Brodband Flux Donwards at Surface				
LBL Avg.	954.1	206.2	857.7	174.5
LBL RSD	0.8 %	0.8 %	1.1 %	3.8 %
Model Avg.	958.2 (959.0)	212.6 (212.9)	869.2 (871.7)	184.4 (185.2)
Avg. Bias	0.4 % (0.5 %)	3.1 % (3.3 %)	1.3 % (1.6 %)	5.7 % (6.2 %)
Model RSD	0.8 % (0.9 %)	1.4 % (2.4 %)	1.0 % (1.6 %)	2.3 % (4.1 %)
Diffuse Broadband Flux at Upwards at TOA				
LBL Avg.	216.1	89.8	194.4	81.7
LBL RSD	1.4 %	1.3 %	1.3 %	2.1 %
Model Avg.	220.0 (220.4)	90.6 (90.5)	200.5 (201.8)	83.9 (84.3)
Avg. Bias	1.8 % (2.0 %)	0.9 % (0.8 %)	3.1 % (3.8 %)	2.8 % (3.3 %)
Model RSD	1.3 % (1.3 %)	2.8 % (2.6 %)	1.7 % (2.5 %)	2.6 % (3.2 %)
Total UV-VIS Downwards Flux at Surface				
LBL Avg.	452.4	89.0	452.0	89.0
LBL RSD	0.7 %	1.1 %	0.2 %	0.5 %
Model Avg.	453.4 (453.1)	91.5 (91.5)	454.1 (453.4)	92.1 (92.2)
Avg. Bias	0.2 % (0.2 %)	2.8 % (2.9 %)	0.5 % (0.4 %)	3.5 % (3.6 %)
Model RSD	1.3 % (1.3 %)	3.4 % (3.3 %)	1.1 % (1.1 %)	3.1 % (3.1 %)
Total Near-IR Downwards Flux at Surface[d]				
LBL Avg.	503.2	117.5	407.2	85.8
LBL RSD	0.8 %	0.5 %	2.4 %	7.1 %
Model Avg.	505.8 (507.0)	121.3 (121.5)	415.3 (418.6)	92.9 (93.6)
Avg. Bias	0.5 % (0.7 %)	3.2 % (3.4 %)	2.0 % (2.8 %)	8.3 % (9.2 %)
Model RSD	2.0 % (1.9 %)	2.4 % (3.7 %)	3.0 % (3.7 %)	3.8 % (7.0 %)

[a] Flux units W m^{-2}; scaled normalized results as described in the text and Fig. 2.
[b] Line-by-line (LBL) benchmarks (Avg. of Models #1 and #2) and non-LBL model results. We exclude Models # 14, 25, 27, 30, and 31 for the model statistics; in parenthesis all models are considered.
[c] Avg. Bias is expressed as a percentage of the LBL Avg. RSD = standard deviation as a percentage of mean.
[d] Near-IR is derived as a difference between broadband and UV-VIS.

A16 Model #16 Beijing Climate Center (BCC-RAD; *H. Zhang, P. Lu*)

The Beijing Climate Center radiation transfer model (BCC-RAD) uses the correlated *k*-distribution (*ck*-D) algorithm adopted by Zhang et al. (2003, 2006a,b) and the 2-stream Eddington algorithm of radiative transfer. The 10–49 000 cm^{-1} spectral range (0.204–1000 µm) is divided into 17 bands (8 longwave and 9 shortwave). Eight major GHGs including H_2O, CO_2, O_3, N_2O, CH_4, and Chlorofluorocarbons (CFCs) are considered. The HITRAN2000 database (Rothman et al., 2003) was used to give line parameters and cross sections; CKD_2.4 (Zhang et al., 2003) generated continuum absorption coefficients due to water vapor, CO_2, O_3, and O_2. The effective absorption coefficients of *ck*-D were calculated based on LBLRTM (Clough and Iacono, 1995) with a spectral interval of 1/4 of the mean spectral line half-width and with a 25 cm^{-1} cutoff for line wings over each band (Clough et al., 1992; Clough and Iacono, 1995). Modeled molecular absorbers in the solar bands are H_2O (including continuum absorption), O_3 and O_2. Nominally, cloud optical properties are from Nakajima et al. (2000) and aerosol optical properties are calculated by Wei and Zhang (2011) and Zhang et al. (2012).

A17 Model #17 CCCMA radiation scheme (CAR-CCCMA, *F. Zhang*)

The Canadian Climate Center radiation scheme calculates SW flux in a vertically inhomogeneous scattering-absorbing atmosphere using a delta-Eddington approximation and adding method (Li et al., 2005). It accounts for the absorption of all radiatively important gases using the correlated *k*-distribution method (*ck*-D) with fits to the HITRAN 96 (Li and Barker, 2005). There are 4 solar bands with a total of 35

Table A5. Synergy across Aerocom Phase II Aerosol Radiative Forcing Experiments*

Model #	Radiative Transfer Experiment *this work*	Aerocom Prescribed (Stier et el., 2012)	Aerocom Direct RF (Myhre et al., 2013)
3	Oslo-DISORT	OsloCTM2	OsloCTM2
11	CAR-RRTMG	CAM-PNNL and GEOS-CHEM	CAM5.1 and GEOS-CHEM
12	RRTMG-SW	CAM-PNNL and GEOS-CHEM	CAM5.1 and GEOS-CHEM
14	MPI-2stream	MPI-2stream	–
15	CAR-GSFC	GOCART GEOS-4 and GOCART MERRA	GOCART and GMI
16	BCC-RAD	–	BCC
18	ECHAM5.5	ECHAM-HAM2	ECHAM5-HAM
24	UKMO-HadGEM2	HadGEM2-ES	HadGEM2

* Radiation scheme, Model #, and name from this work and corresponding model names in Stier et el. (2012) and Myhre et al. (2013) which use the same or similar radiation schemes.

sub-spectra for pressure layers > 1 mb or 40 sub-spectra for pressure layers < 1 mb over the range 0.2∼4.0 µm. Modeled molecular absorbers in the solar bands are H_2O, O_3, CO_2, and O_2. This model contains a proper treatment of spectral overlap between solar and infrared radiation. The effect of the additional solar energy ($\sim 12\,W\,m^{-2}$ in 0–2500 cm^{-1}) is also included simply by imposing this energy onto the infrared downward flux for the appropriate infrared bands (Li and Barker, 2005). A new parameterization for the effects of atmospheric spherical curvature and refraction and their impact on radiative transfer has been incorporated (Li and Shibata, 2006). This rigorous scheme enables variations in both the path length and the gaseous amount along a solar direct beam. These variations can then be accurately evaluated in the radiative transfer process, and we find better results in flux and heating rates when compared to other parameterizations.

A18 Model #18 ECHAM5.5 (*J. Quaas, S. Kinne, P. Stier*)

The ECHAM5.5 general circulation model (Roeckner et al., 2003) used in several contributions to the AeroCom project applies a solar radiative transfer scheme based on Fouquart and Bonnel (1980). In a two-stream approximation, scattering and absorption by molecules and aerosols are taken into account. Since the update by Cagnazzo et al. (2007), six bands are used, with intervals between 0.185 µm, 0.25 µm, 0.44 µm, 0.69 µm, 1.19 µm, 2.38 µm and 4.0 µm. The range 0.185–0.69 µm is considered the visible range, the range 0.69–4.0 µm, the near-infrared. We use the off-line radiation code extracted by Klocke et al. (2011) and take into account the effects of water vapor, ozone, methane and N_2O from the prescribed profiles, as well as of carbon dioxide with a constant mixing ratio of 348 ppmv. Carbon monoxide is not considered in the radiation, and the mixing ratios of chloroflourocarbons are set to zero.

The configuration is considered as an open ocean surface, and the vertical resolution is chosen as in the input files, where the boundary of the lowest surface is set to 0 km, and the layer-mean values are the averages of the layer interfaces. The uppermost layer-mean values are considered the same as at its lower boundary, with the temperature at the upper boundary as at the lower one, the pressure at the upper boundary 0 hPa, and the layer-mean pressure half the pressure at the lower boundary. For the aerosols, the Ångström exponent is used to extrapolate the 550 nm optical depth to the other bands considering the band-average wavelength. The single-scattering albedo is assumed spectrally constant.

A19 Model #19 UMD-SRB (*Y. Ma and R. T. Pinker*)

The radiative transfer model used in the prescribed tests is part of the University of Maryland Surface Radiative Budget (UMD-SRB) module for satellite retrieval of shortwave (SW) fluxes. It calculates broadband SW fluxes in a plane-parallel, vertically inhomogeneous, scattering and absorbing atmosphere. The model accounts for (1) absorption by water vapor and ozone; (2) Rayleigh scattering; (3) scattering and absorption by aerosols and cloud droplets; and (4) multiple reflection between the atmosphere and surface. Radiative transfer is dealt with the delta-Eddington approximation. In the prescribed AeroCom experiments, SW fluxes are computed in 7 broadband intervals (0.2–0.4, 0.4–0.5, 0.5–0.6, 0.6–0.7, 0.7–1.19, 1.19–2.38 and 2.38–4.00 µm). Water vapor absorption is accounted for in the 0.7–4.0 µm spectral interval; ozone is accounted for in the 0.2–0.4 µm (UV) and in 0.5–0.6 µm (VIS) spectral intervals. For water vapor and water vapor continuum, we use the *k*-distribution method proposed by Chou and Lee (1996) and further advanced by Tarasova and Fomin (2000). Reference transmission database is HITRAN96. Ozone parameterization follows Lacis and Hansen (1974). The model is configured with variable number of layers (>31), depending on presence of aerosol and/or clouds. More details can be found in Wang and Pinker (2009). For this study 1 km resolution was used below 25 km; above this level, the vertical resolution for ozone and water vapor profiles is 5 km.

A20 Models #20-23 University of Reading Edwards and Slingo (ES96, *E. Highwood, C. Ryder, B. Harris*)

The Edwards and Slingo radiation scheme (ES96) is a flexible radiative transfer model as described by Edwards and Slingo (1996) with updates from Walters et al. (2011). Results using the offline version released by the Met Office on 21 December 2009 are presented using a two stream practical improved flux method (PIFM, Zdunkowski et al., 1980). The user is able to define the number of spectral bands and model vertical levels. The spectral resolution is set by an external spectral file. The user is able to use (and adjust) spectral files supplied with the code, or create new versions. Here we provide results using standard supplied versions of spectral files with either 6 or 220 spectral bands covering wavelengths of 0.2 to 10 microns. The spectral file supplies details of atmospheric radiative properties such as gaseous absorption which may differ between spectral files. Therefore each subsequent description of ES96 makes reference to a specific spectral file and differences therein.

Water vapor terms are updated based on the HITRAN 2001 database (Rothman et al., 2003) for gaseous absorption coefficients, with updates up to 2003. For all other gases absorption is based on HITRAN92. Gaseous absorption is represented according to Cusack et al. (1999) using a correlated-*k* method.

ES96 allows the user to select whether delta-rescaling is implemented for particle scattering (ES96-D). Delta-rescaling provides more accurate total flux measurements at the expense of the partitioning between the direct and diffuse fluxes since delta-rescaling effectively increases the flux in the direct beam to account for strong forward aerosol scattering.

Results are presented using ES96 with 6 and 220 spectral bands (Model #20 ES96-6 and Model #21 ES96-220), using the spectral files "sp_sw_hadgem1_3r" and "sp_sw_220_r", respectively. Aerosol properties in the spectral files are adjusted to represent AeroCom protocol requirements. Particle scattering is presented both for cases where no delta rescaling is included (model #20 ES96-6 and model #21 ES96-220) and where delta rescaling is included (model #22 ES96-6-D and model #23 ES96-220-D).

Absorption due to CO_2 and O_2 concentrations are set to $0.579\,g\,kg^{-1}$ and $231\,g\,kg^{-1}$ which are constant with altitude, absorption due to H_20 and O_3, are included as prescribed by AeroCom. N_2O and CH_4 are included from the AFGL standard atmospheres in the 220 band cases (ES96-220) but are excluded in the 6 band cases (ES96-6). CO is not included.

A21 Model #24 UKMO HadGEM2 GCM (*S. T. Rumbold*)

The online radiation code in HadGEM2 is consistent with the offline version of ES96 by design and is maintained as such at the UK Met Office (UKMO). A description of the online implementation can be found in Martin et al. (2011). For the UKMO-HadGEM2 contribution to this intercomparison, the offline code is used and is configured in an identical manner to that of the HadGEM2 online radiation. This configuration is as in ES96-6-D (Model #22), but with vertical profiles of gases interpolated to mid-levels linearly in the logarithm of pressure. All AeroCom prescribed gases are used apart from N_2O, CO and CH_4 as they are not included in the shortwave part of the online radiation scheme. Where needed, aerosol was prescribed at constant mass mixing ratio in the two lower most model layers (zero elsewhere) to achieve the correct optical depth.

A22 Model #25 CAWCR radiation scheme (CAR-CAWCR, *F. Zhang*)

The Center for Australian Weather and Climate Research (CAWCR) Sun-Edwards-Slingo radiation scheme (SES2) is a model used in numerical weather prediction (NWP) and climate models (Sun and Rikus, 1999; Sun, 2008) and is based on the Edwards and Slingo (1996) radiation scheme. The model calculates SW flux in a vertically inhomogeneous scattering-absorbing atmosphere using a delta-two-stream algorithm, and accounts for the absorption of all radiatively important gases using the exponential sum fitting transmission method (ESFT). The line-by-line radiative transfer model (GENLN2) (Edwards, 1992) provides the absorption coefficients for the ESFT method. The accuracy of these absorption coefficients has been established by comparison of GENLN2 with other line-by-line models such as LBLRTM (Clough et al., 1992) and measurements from ARM (Stokes and Schwartz, 1994). Modeled molecular absorbers in the solar bands are H_2O (including continuum effects), O_3, CO_2, CH_4, N_2O, and O_2. There are 9 solar bands with total 27 sub-spectra over 0.2∼5.0 µm. The radiation code has two novel features: one is the flexible spectral resolution of the code, and the second is that the same spectral framework for both the longwave and shortwave components. This makes the code easy to maintain and develop. In this scheme, the effect of the additional solar energy (about $12\,Wm^{-2}$ in 0–$2500\,cm^{-1}$) is also included simply by imposing this energy onto the infrared downward flux for the appropriate infrared bands (Li and Barker, 2005).

A23 Model #26 CAM radiation scheme (CAR-CAM, *F. Zhang*)

The NCAR CAM model (Collins et al., 2004) calculates SW flux in a vertically inhomogeneous scattering-absorbing

atmosphere using a delta-two-stream algorithm. The solar spectrum is divided into 19 discrete spectral and pseudo-spectral intervals: 7 for O_3, 1 for the visible, 7 for H_2O including water-vapor continuum, 3 for CO_2, and 1 for the near-infrared following Collins (1998). The solar absorption by water vapor between 1000 and 18 000 cm^{-1} is treated using seven pseudo-spectral intervals with a constant specific extinction specified for each interval. These extinctions have been adjusted to minimize errors in heating rates and flux divergences relative to line-by-line (LBL) calculations for reference atmospheres (Anderson et al., 1986) using GENLN3 (Edwards, 1992) combined with the radiative transfer solver DISORT2 (Stamnes et al., 1988). This parameterization is essentially an exponential sum fit (e.g., Wiscombe and Evans, 1977). LBL calculations are performed with the HITRAN 2000 line database (Rothman et al., 2003) and the Clough, Kneizys, and Davies (CKD) model version 2.4.1 (Clough et al., 1989). The Rayleigh scattering optical depths in the seven pseudo-spectral intervals have been changed for consistency with LBL calculations of the variation of water-vapor absorption with wavelength. Modeled molecular absorbers in the solar bands are H_2O (including continuum absorption), CO_2, and O_3.

A24 Modle #27 ULAQ (*G. Pitari, G. Di Genova*)

The University of L'Aquila radiative transfer module, operating on-line in the climate-chemistry coupled model ULAQ-CCM, is a two-stream delta-Eddington approximation model (Toon et al., 1989) used for chemical species photolysis rate calculation in UV-visible wavelengths and for solar heating rates and radiative forcing in UV-VIS-NIR bands. Species cross sections are updated using JPL (2011) recommendations from the MPI-MAINZ database, while water vapor absorption data are derived from HITRAN92. Schumann-Runge bands are treated following the parameterization of Minschwaner et al. (1993) based on (fixed-T) ODF formulation. Diurnal averages are calculated with a 5 point Gaussian quadrature.

Top-of-atmosphere solar fluxes are taken from SUSIM-SL2 and LOWTRAN7 and are carefully integrated on the wavelength bins used in the model: they are in total 150 in the UV and visible range and 100 in the NIR, covering the solar spectrum from Lyman-alpha up to 7 µm. Sun-earth distance is calculated daily as a function of orbit eccentricity and the solar cycle is included. Sphericity is treated by means of Chapman functions (Dahlback and Stames, 1991). Refraction is taken into account with an iterated ray-tracing technique in a simple exponential refraction model.

Absorption/scattering optical depths take into account Rayleigh scattering, absorption from O_3, O_2, NO_2, SO_2, H_2O, CO_2 and scattering/absorption from aerosol particles. Aerosol extinction values are passed daily from the ULAQ-CCM aerosol module to the radiative transfer module, with appropriate wavelength-dependent values of Q-ext, *g*, and single scattering albedo, given the calculated size distribution of the particles. Surface albedo is nominally taken from MERRA 2D hourly averaged data.

The native vertical resolution of our model is 570 m. For this study, we linearly interpolate both AFGL O_3 and H_2O concentrations to this higher resolution using the calculated column values on the AFGL vertical grid as a constraint for both species (i.e. the calculated vertical columns after interpolation are re-normalized to the original values).

A25 Model #28 FORTH (*I. Vardavas, N. Hatzianstassiou, C. Matsoukas*)

The incoming solar irradiance conforms to the spectral profile of Gueymard (2004). The model apportions 69.48 % of the incoming spectral irradiance to the ultra violet-visible-near infrared (UV-Vis-NIR) part (0.20–1 µm) and 30.52 % to the near infrared-infrared (NIR-IR) part (1–10 µm). The radiative transfer equations are solved for 118 separate wavelengths for the UV-Vis-NIR part and for 10 bands for the NIR-IR part, using the delta-Eddington method as modified by Joseph et al. (1976). For a more detailed model description the reader is referred to Hatzianastassiou et al. (2004a,b, 2007a); Hatzianastassiou et a. (2007b) and Vardavas and Taylor (2007). The model takes into account clouds, Rayleigh scattering due to atmospheric gas molecules, absorption from O_3, O_2, CO_2, H_2O, and CH_4, and scattering and absorption due to aerosols. The model output includes downwelling and upwelling fluxes at the top of atmosphere, at the surface and at any atmospheric height. For this study we interpolated the AFGL water-vapor and ozone profiles to our model vertical resolution linearly in log(pressure)-log(gas concentration) space.

A26 Model #29 GFDL radiation scheme (CAR-GFDL, *F. Zhang*)

The NOAA GFDL radiation scheme (Freidenreich and Ramaswamy, 1999) uses the exponential-sum-fit technique (ESFT) to develop the parameterization of water vapor transmission in the main absorbing bands. An absorptivity approach is used to represent the heating contributions by CO_2 and O_2, and a spectral averaging of the continuum-like properties is used to represent the O_3 heating. Spectral line data for H_2O, CO_2, O_3, CH_4 and N_2O are now based on the HITRAN92 catalog (Rothman et al., 1992). The delta-Eddington method is used to solve for the reflection and transmission, while the "adding" method is used to combine the layers. The single-scattering properties can account for all types of scattering and absorbing constituents (molecules, drops, ice particles, and aerosols), given their respective single-scattering properties and mass concentrations. There are 18 solar bands with total 38 sub-spectra over 0.173∼20.0 µm.

A27 Model #30 MPI-MOM (*S. Kinne*)

The Max Plank Institute for Meteorology MPI-MOM scheme combines the matrix-operator (Plass et al., 1973) and adding doubling method. The method was prepared for atmospheric broadband sold radiative transfer calculation by Grassl (1978). The trace gas absorption (including water vapor) in the near-IR is based on LOWTRAN-5 data and ozone absorption data are based on Vigroux (1953). Trace-gases were interpolated to the model resolution in the vertical using the log of pressure.

A28 Model #31 Matrix-Operator Model (MOMO; *J. Fischer, L. Doppler*)

MOMO is a radiation transfer code for radiance and irradiance computations in the ocean and atmosphere (Fell and Fischer, 2001; Fischer and Grassl, 1984). Its spectral range is 0.2–100 µm. MOMO combines the matrix-operator (Plass et al., 1973) and adding doubling method. The gas transmission is computed using a code CGASA, derived from XTRA (Rathke and Fischer, 2000). CGASA combines the water-vapor continuum model of Clough et al. (1992) with Voigt line computations. Line properties are taken from the HITRAN-2008 spectral database (Rothman et al., 2009). A *k*-distribution method is used, following Bennartz and Fischer (2000). This *k*-distribution is exact (we do not make the correlated approximation). For this study, we computed MOMO simulations within 55 UV bands and 12 VIS bands, in order to consider the high variation of Rayleigh optical depth. 30 bands have been defined to model the near-IR radiation. 3000 k-intervals have been needed to model water vapor, ozone and mixed gas absorption lines with accuracy. The vertical resolution was 1 km from 0 to 26 km and 2 km from 26 to 100 km. Within aerosols layers, the adding-doubling method divided the layers in 2n sub-layers in order to consider multi-scattering.

Acknowledgements. C. Randles was supported by the NASA Atmospheric Composition Modeling and Analysis (ACMAP) Program Grant NNX11AK20G under R. Eckman. G. Myhre was supported by the projects SLAC (Short Lived Atmospheric Components) and EarthClim funded by the Norwegian Research Council. M. Schulz acknowledges support under the EU ECLIPSE project, contract No. 282688. J. Huttunen was supported by Graduate school in Physics, Chemistry, Biology and Meteorology of Atmospheric Composition and Climate Change: From Molecular Processes to Global Observations and Models. D. Neubauer and R. Hitzenberger acknowledge financial funding from the University of Vienna, FPF 234 and thank Warren Wiscombe (Goddard Space Flight Center) for the ESFT program. D. Neubauer gratefully acknowledges the support by research fellowship F-369, University of Vienna. L. Oreopoulos and D. Lee acknowledge support from NASA's Modeling Analysis and Prediction program managed by D. Considine. The work of R. T. Pinker and Y. Ma was supported under grant NNX11AF54G through the NASA Science of Terra and Aqua Program and grant NNX08AN40A from the NASA Science Mission Directorate-Division of Earth Science. S. T. Rumbold was supported by the Joint DECC and Defra Integrated Climate Programme (GA01101). H. Yu was supported by NASA ACMAP, managed by R. Eckman. F. Zhang was supported by US DOE office of Biological and Environmental Research (BER) DE-SC0001683. H. Zhang was funded and supported by the "Strategic Priority Research Program – Climate Change: Carbon Budget and Relevant Issues" (XDA05040200) and "National High-tech Research and Development (863) Project (2011AA12A104)". P. Lu was supported by National Basic Research Program of China (2011CB403405). The authors thank Q. Fu, Jun Wang, and one anonymous reviewer for their helpful comments that helped to improve the manuscript.

Edited by: Q. Fu

References

Anderson, G. P., Clough, S. A., Kneizys, F. X., Chetwynd, J. H., and Shettle, E. P.: AFGL atmospheric constituent profiles (0–120 km). Technical Report AFGL-TR-86-0110, AFGL (OPI), Hanscom AFB, MA. 01736, 1986.

Arking, A.: Effects of bias in solar radiative transfer codes on global model simulations, Geophys. Res. Lett., 32, L20717, doi:10.1029/2005GL023644, 2005.

Bennartz, R. and Fischer, J. A.: A modified k-distribution approach applied to narrow band water vapor and oxygen absorption estimates in the near infrared, J. Quant. Spectrosc. Radiat. Transfer, 66, 539–553, 2000.

Boucher, O., Schwartz, S. E., Ackerman, T. P., Anderson, T. L., Bergstrom, B., Bonnel, B., Chýlek, P., Dahlback, A., Fouquart, Y. Fu, Q. Halthore, R. N., Haywood, J. M., Iversen, T., Kato, S., Kinne, S., Kirkevåg, A., Knapp, K. R., Lacis, A., Laszlo, I., Mischenko, M. I., Nemensure, S., Ramaswamy, V., Roberts, D. L., Russell, P., Schlesinger, M. E., Stephens, G. L., Wagener, R., Wang, M., Wong, J., and F. Yang: Intercomparison of models representing direct shortwave radiative forcing by sulfate aerosols, J. Geophys. Res., 103, 16979–16998, 1998.

Cagnazzo, C., Manzini, E., Giorgetta, M. A., Forster, P. M. De F., and Morcrette, J. J.: Impact of an improved shortwave radiation scheme in the MAECHAM5 General Circulation Model, Atmos. Chem. Phys., 7, 2503–2515, doi:10.5194/acp-7-2503-2007, 2007.

Chandrasekhar, S.: Radiative Transfer, Dover, Mineola, NY, USA, 393 pp., 1960.

Chou, M.-D. and Lee, K. T.: Parameterizations for the absorption of solar radiation by water vapor and ozone, J. Atmos. Sci., 53, 1203–1208, 1996.

Chou, M.-D. and Suarez, M. J.: A solar radiation parameterization for atmospheric studies, (last revision on March 2002) Technical Report Series on Global Modeling and Data Assimilation, edited by: M. J. Suarez, NASA/TM-1999-104606, Vol. 15, Goddard Space Flight Center, Greenbelt, MD, 42 pp., 1999.

Chýlek, P. and Coakley, J. A.: Aerosols and Climate, Science, 183, 75–77, 1974.

Clough, S. A. and Iacono, M. J.: Line-by-line calculation of atmospheric fluxes and cooling rates 2. Application to carbon dioxide,

ozone, methane, nitrous oxide and the halocarbons, J. Geophys. Res., 100, 16519–16535, 1995.

Clough, S. A., Kneizys, F. X., and Davies, R. W.: Line shape and the water vapor continuum, Atmos. Res., 23, 229–241, 1989.

Clough, S. A., Iacono, M. J., and J. L. Moncet: Line-by-line calculations of atmospheric fluxes and cooling rates: Application to water vapor. J. Geophys. Res., 97, 15761-15785, 1992.

Clough, S. A., Shephard, M. W., Mlawer, E. J., Delamere, J. S., Iacono, M. J., Cady-Pereira, K., Boukabara, S., and Brown, P. D.: Atmospheric radiative transfer modeling: a summary of the AER codes. J. Quant. Spectrosc. Radiat. Transf., 91, 233–244, doi:10.1016/j.jqsrt.2004.05.058, 2005.

Collins, W. D.: A global signature of enhanced shortwave absorption by clouds, J. Geophys. Res., 103, 31669–31679, 1998.

Collins, W. D., Rasch, P. J., Boville, B. A., Hack, J. J., McCaa, J. R., Williamson, D. L., Kiehl, J. T., Briegleb, B., Bitz, C., Lin, S.-J., Zhang, M., and Dai, Y.: Description of the NCAR Community Atmosphere Model (CAM 3.0), NCAR Technical Note, NCAR/TN-464+STR, 226 pp., 2004.

Cusack, S., Edwards, J., and Crowther, J.: Investigating k distribution methods for paramterizing gaseous absorption in the Hadley Centre Climate Model, J. Geophys. Res., 104, 2051–2057, doi:10.1029/1998JD200063, 1999.

Dahlback, A. and Stamnes, K.: A new spherical model for computing the radiation field available for photolysis and heating at twilight, Planet. Space Sci., 39, 671–683, 1991.

Edwards, D. P.: GENLN2: A general line-by-line atmospheric transmittance and radiance model. Technical Report NCAR/TN-367+STR, NCAR, P.O. Box 3000, Boulder, Colorado, 80307–3000, 147 pp., 1992.

Edwards, J. M. and Slingo, A.: Studies with a flexible new radiation code. I: Choosing a configuration for a large-scale model, Q. J. Roy. Meteor. Soc., 122, 689–719, 1996.

Fell, F. and Fischer, J.: Numerical simulation of the light field in the atmosphere–ocean system using the matrix-operator method, J. Quant. Spectrosc. Radiat. Transf., 69, 351–388, 2001.

Fischer, J. and Grassl, H.: Radiative transfer in an atmosphere-ocean system: an azimuthally dependent matrix-operator approach. Appl. Opt., 23, 1032–1039, 1984.

Forster, P., Ramaswamy, V., Artaxo, P., Berntsen, T., Betts, R., Fahey, D. W., Haywood, J., Lowe, J., Myhre, G., Nganga, J., Prinn, R., Raga, G., Schulz, M., and Dorland, R. V.: Climate Change 2007: The Physical Science Basis: Contribution of Working Group I to the Fourth Assessment Report of the Intergovernmental Panel on Climate Change, Chap. Changes in Atmospheric Constituents and in Radiative Forcing, Cambridge University Press, Cambridge, UK and New York, NY, USA, 2007.

Forster, P. M., V. I. Fomichev, E. Rozanov, C. Cagnazzo, A. I. Jonsson, U. Langematz, B. Fomin, M. J. Iacono, B. Mayer, E. Mlawer, G. Myhre, R. W. Portmann, H. Akiyoshi, V. Falaleeva, N. Gillett, A. Karpechko, J. Li, P. Lemennais, O. Morgenstern, S. Oberländer, M. Sigmond, and K. Shibata: Evaluation of radiation scheme performance within chemistry climate models, J. Geophys. Res., 116, D10302, doi:10.1029/2010JD015361, 2011.

Fouquart, Y. and Bonnel, B.: Computations of solar heating of the Earth's atmosphere: A new parameterization, Beitr. Phys. Atmos., 53, 35–62, 1980.

Fouquart, Y., Bonnel, B., and Ramaswamy, V.: Intercomparing shortwave radiation codes for climate studies, J. Geophys. Res., 96, 8955–8968, 1991.

Freidenreich, S. M. and Ramaswamy, V.: A new multiple-band solar radiative parameterization for general circulation models. J. Geophy. Res., 104, 31389–31409, 1999.

Fu, Q. and Liou, K. N.: On the correlated k-distribution method for radiative transfer in nonhomogeneous atmospheres. J. Atmos. Sci., 49, 2139–2156, 1992.

Fu, Q. and Liou, K. N.: Parameterization of the radiative properties of cirrus clouds, J. Atmos. Sci., 50, 2008–2025, 1993.

Gu, Y., Liou, K. N., Chen, W., and Liao, H.: Direct climate effect of black carbon in China and its impact on dust storms, J. Geophys. Res., 115, D00K14, doi:10.1029/2009JD01342, 2010.

Gu, Y., Liou, K. N., Ou, S. C., and Fovell, R.: Cirrus cloud simulations using WRF with improved radiation parameterization and increased vertical resolution. J. Geophys. Res., 116, D06119, doi:10.1029/2010JD014574, 2011.

Gueymard, C. A.: The sun's total and spectral irradiance for solar energy applications and solar radiation models, Sol. Energy, 76, 423–453, 2004.

Grassl, H.: Strahlung in getrübten Atmosphären und in Wolken, Contr. Atmos. Phys., 49, 225–236, 1978.

Halthore, R. N., Crisp, D., Schwartz, S. E., Anderson, G. P., Berk, A., Bonnel, B., Boucher, O., Chang, F.-L., Chou, M.-D., Clothiaux, E. E., Dubuisson, P., Fomin, B., Fouquart, Y., Freidenreich, S., Gautier, C., Kato, S., Laszlo, I., Li, Z., Mather, J. H., Plana-Fattori, A., Ramaswamy, V., Ricchiazzi, P., Shiren, Y., Trishchenko, A., and Wiscombe, W.: Intercomparison of shortwave radiative transfer codes and measurements, J. Geophys. Res., 110, D11206, doi:10.1029/2004JD005293, 2005.

Hatzianastassiou, N., Katsoulis, B., and Vardavas, I.: Global distribution of aerosol direct radiative forcing in the ultraviolet and visible arising under clear skies, Tellus, 56B, 51–71, doi:10.1111/j.1600-0889.2004.00085.x, 2004a.

Hatzianastassiou, N., Matsoukas, C., Hatzidimitriou, D., Pavlakis, C., Drakakis, M., and Vardavas, I.: Ten-year radiation budget of the Earth: 1984–1993, Int. J. Climatol., 24, 1785–1802, doi:10.1002/joc.1110, 2004b.

Hatzianastassiou, N., Matsoukas, C., Drakakis, E., Stackhouse, P. W., Koepke, P., Fotiadi, A., Pavlakis, K. G., and Vardavas, I.: The direct effect of aerosols on solar radiation based on satellite observations, reanalysis datasets, and spectral aerosol optical properties from Global Aerosol Data Set (GADS), Atmos. Chem. Phys., 7, 2585–2599, doi:10.5194/acp-7-2585-2007, 2007a.

Hatzianastassiou, N., Matsoukas, C., Fotiadi, A., P. W. Stackhouse Jr., Koepke, P., Pavlakis, K. G., and Vardavas, I.: Modelling the direct effect of aerosols in the solar near-infrared on a planetary scale, Atmos. Chem. Phys., 7, 3211–3229, doi:10.5194/acp-7-3211-2007, 2007b.

Howard, J. N., King, J. I. F., and Gast, P. R.: Thermal radiation, Handbook of Geophysics, 16, 16:1–16:32, Macmillan, Indianapolis, Indiana, 1961.

Iacono, M. J., Delamere, J. S., Mlawer, E. J., Shephard, M. W., Clough, S. A., and Collins, W. D: Radiative forcing by long-lived greenhouse gases: Calculations with the AER radiative transfer models, J. Geophys. Res., 113, D13103, doi:10.1029/2008JD009944, 2008.

Joseph, J. H., Wiscombe, W. J., and Weinman, J. A.: The Delta-Eddington Approximation for Radiative Flux Transfer. J. Atmos. Sci., 33, 2452–2459, 1976.

JPL: Chemical Kinetics and Photochemical Data for Use in Atmospheric Studies, Evaluation Number 17, JPL Publication 10-6, 2011.

Kato, S., Ackerman, T. P. and Mather, J. H. and Clothiaux, E. E.: The k-distribution method and correlated-k approximation for a shortwave radiative transfer model, J. Quant. Spectrosc. Radiat. Transfer, 62, 109–121, 1999.

Key, J. and Schweiger, A. J.: Tools for atmospheric radiative transfer: Streamer and FluxNet, Comput. Geosci., 24, 443–451, doi:10.1016/S0098-3004(97)00130-1, 1998.

Kinne, S., Schulz, M., Textor, C., Guibert, S., Balkanski, Y., Bauer, S. E., Berntsen, T., Berglen, T. F., Boucher, O., Chin, M., Collins, W., Dentener, F., Diehl, T., Easter, R., Feichter, J., Fillmore, D., Ghan, S., Ginoux, P., Gong, S., Grini, A., Hendricks, J., Herzog, M., Horowitz, L., Isaksen, I., Iversen, T., Kirkevåg, A., Kloster, S., Koch, D., Kristjansson, J. E., Krol, M., Lauer, A., Lamarque, J. F., Lesins, G., Liu, X., Lohmann, U., Montanaro, V., Myhre, G., Penner, J., Pitari, G., Reddy, S., Seland, Ø., Stier, P., Takemura, T., and Tie, X.: An AeroCom initial assessment – optical properties in aerosol component modules of global models, Atmos. Chem. Phys., 6, 1815–1834, doi:10.5194/acp-6-1815-2006, 2006.

Klocke, D., Pincus, R., and Quaas, J.: On constraining estimates of climate sensitivity with present day observations through model weighting, J. Clim., 24, 6092–6099, doi:10.1175/2011JCLI4193.1, 2011.

Kneizys F. X., Shettle E. P., Abreu L. W., Chetwynd J. H., Anderson G. P., Gallery W. O., Selby J. E. A., and S. A. Clough: Report AFGL-TR-88-0177, Air Force Geophysics Laboratory, Hanscom AFB, Massachusetts, USA, 1988.

Koch, D., Schulz, M., Kinne, S., McNaughton, C., Spackman, J. R., Balkanski, Y., Bauer, S., Berntsen, T., Bond, T. C., Boucher, O., Chin, M., Clarke, A., De Luca, N., Dentener, F., Diehl, T., Dubovik, O., Easter, R., Fahey, D. W., Feichter, J., Fillmore, D., Freitag, S., Ghan, S., Ginoux, P., Gong, S., Horowitz, L., Iversen, T., Kirkevåg, A., Klimont, Z., Kondo, Y., Krol, M., Liu, X., Miller, R., Montanaro, V., Moteki, N., Myhre, G., Penner, J. E., Perlwitz, J., Pitari, G., Reddy, S., Sahu, L., Sakamoto, H., Schuster, G., Schwarz, J. P., Seland, Ø., Stier, P., Takegawa, N., Takemura, T., Textor, C., van Aardenne, J. A., and Zhao, Y.: Evaluation of black carbon estimations in global aerosol models, Atmos. Chem. Phys., 9, 9001–9026, doi:10.5194/acp-9-9001-2009, 2009.

Lacis, A. A. and Hansen, J. E.: Parameterization for absorption of solar-radiation in earths atmosphere, J. Atmos. Sci., 31, 118–133, 1974.

Lacis A. A. and Oinas, V. A.: Description of the correlated k-distribution method, J. Geophys. Res.; 96, 9027–9064, 1991.

Lean, J., Rottman, G., Harder, J., and G. Kopp: SOURCE contributions to new understanding of global change and solar variability, Solar Phys., 230, 27–53, 2005.

Lenoble, J.: Radiative Transfer in Scattering and Absorbing Atmospheres: Standard Computational Procedures, A. Deepak, Hampton, VA, USA, 1985.

Li, J. and Barker, H. W.: A radiation alogorithm with Correlated-k Distribution. Part I: Local thermal equilibrium. J. Atmos. Sci., 62, 286–309, 2005.

Li, J. and Shibata, K.: On the effective solar pathlength, J. Atmos. Sci., 63, 1365–1373, doi:10.1175/JAS3682.1, 2006.

Li, J., Dobbie, S., Risnen, P., and Min, Q.: Accounting for unresolved clouds in a 1-D solar radiative-transfer model, Q. J. Roy. Meteorol. Soc., 131, 1607–1629, 2005.

Liang, X.-Z. and F. Zhang: Cloud-Aerosol-Radiation (CAR) Ensemble Modeling System. J. Geophys. Res., submitted, 2012.

Liou, K.-N.: Radiation and Cloud Processes in the Atmosphere, Oxford Univ. Press, New York, USA, 1992.

Liou, K. N., Gu, Y., Yue, Q., and McFarguhar, G.: On the correlation between ice water content and ice crystal size and its application to radiative transfer and general circulation models. Geophys. Res. Lett., 35, L13805, doi:10.1029/2008GL033918, 2008.

The HadGEM2 Development Team: G. M. Martin, Bellouin, N., Collins, W. J., Culverwell, I. D., Halloran, P. R., Hardiman, S. C., Hinton, T. J., Jones, C. D., McDonald, R. E., McLaren, A. J., O'Connor, F. M., Roberts, M. J., Rodriguez, J. M., Woodward, S., Best, M. J., Brooks, M. E., Brown, A. R., Butchart, N., Dearden, C., Derbyshire, S. H., Dharssi, I., Doutriaux-Boucher, M., Edwards, J. M., Falloon, P. D., Gedney, N., Gray, L. J., Hewitt, H. T., Hobson, M., Huddleston, M. R., Hughes, J., Ineson, S., Ingram, W. J., James, P. M., Johns, T. C., Johnson, C. E., Jones, A., Jones, C. P., Joshi, M. M., Keen, A. B., Liddicoat, S., Lock, A. P., Maidens, A. V., Manners, J. C., Milton, S. F., Rae, J. G. L., Ridley, J. K., Sellar, A., Senior, C. A., Totterdell, I. J., Verhoef, A., Vidale, P. L., and Wiltshire, A.: The HadGEM2 family of Met Office Unified Model climate configurations, Geosci. Model Dev., 4, 723–757, doi:10.5194/gmd-4-723-2011, 2011.

Mayer, B. and Kylling, A.: Technical note: The libRadtran software package for radiative transfer calculations – description and examples of use, Atmos. Chem. Phys., 5, 1855–1877, doi:10.5194/acp-5-1855-2005, 2005.

Meador, W. E. and Weaver, W. R.: Two-Stream Approximations to Radiative Transfer in Planetary Atmospheres: A Unified Description of Existing Methods and a New Improvement, J. Atmos. Sci., 37, 630–643, 1980.

Minschwaner, K., Salawitch, R. J., and McElroy, M. B.: Absorption of Solar Radiation by O_2: Implications for O_3 and Lifetimes of N_2O, CFCl3, and CF2Cl2, J. Geophys. Res., 98, 10543–10561, doi:10.1029/93JD00223, 1993.

Myhre, G., Samset, B. H., Schulz, M., Balkanski, Y., Bauer, S., Berntsen, T. K., Bian, H., Bellouin, N., Chin, M., Diehl, T., Easter, R. C., Feichter, J., Ghan, S. J., Hauglustaine, D., Iversen, T., Kinne, S., Kirkevåg, A., Lamarque, J.-F., Lin, G., Liu, X., Lund, M. T., Luo, G., Ma, X., van Noije, T., Penner, J. E., Rasch, P. J., Ruiz, A., Seland, Ø., Skeie, R. B., Stier, P., Takemura, T., Tsigaridis, K., Wang, P., Wang, Z., Xu, L., Yu, H., Yu, F., Yoon, J.-H., Zhang, K., Zhang, H., and Zhou, C.: Radiative forcing of the direct aerosol effect from AeroCom Phase II simulations, Atmos. Chem. Phys., 13, 1853–1877, doi:10.5194/acp-13-1853-2013, 2013.

Myhre, G., Jonson, J. E., Bartnicki, J., Stordal, F., and Shine, K. P.: Role of spatial and temporal variations in the computation of radiative forcing due to sulphate aerosols: A regional study, Q. J. Roy. Meterol. Soc., 128, 973–989, 2002.

Nakajima, T., Tsukamoto, M., Tsushima, Y., Numafuti, A., and Kimura, T.: Modeling of radiative process in an atmospheric general circulation model, Appl. Opt., 39, 4869–4878, 2000.

Nemensure, S., Wagener, R., and Schwartz, S. E.: Direct shortwave forcing of climate by the anthropogenic sulfate aerosol: Sensitivity to particle size, composition, and relative humidity, J. Geo-

phys. Res., 100, 26105–26116.

Neubauer, D., Vrtala, A., Leitner, J. J., Firneis, M. G., and Hitzenberger, R.: Development of a model to compute the extension of life supporting zones for Earth-like exoplanets, Orig. Life Evol. Biosph. 41, 545–552, doi:10.1007/s11084-011-9259-9, 2011.

Oreopoulos, L. and Barker, H. W.: Accounting for subgrid-scale cloud variability in a multi-layer 1-D solar radiative transfer algorithm, Q. Roy. Meteor. Soc., 125, 301–330, 1999.

Oreopoulos, L., Mlawer, E., Delamere, J., Shippert, T., Cole, J., Fomin, B., Iacono, M., Jin, Z., Li, J., Manners, J., Räisänen, P., Rose, F., Zhang, Y., and Wilson, M. J.: The Continual Intercomparison of Radiation Codes: Results from Phase I, J. Geophys. Res., 117, D06118, doi:10.1029/2011JD016821, 2012.

Plass, G., Kattawar, G., and Catchings, F.: Matrix-operator theory of radiative transfer. 1: Rayleigh scattering, Appl. Opt., 12, 314–329, 1973.

Rathke, C. and Fischer, J.: Retrieval of cloud microphysical properties from thermal infrared observations by a fast iterative radiance 1tting method, J. Atmos. Ocean Technol., 17, 1509–1524, 2000.

Roeckner, E., Bäuml, G., Bonaventura, L., Brokopf, R., Esch, M., Giorgetta, M., Hagemann, S., Kirchner, I., Kornblueh, L., Manzini, E., Rhodin, A., Schlese, U., Schulzweida, U., and Tompkins, A.: The atmospheric general circulation model ECHAM5. Part I: Model description, Max Planck Institute for Meteorology Rep. 349, 127 pp., 2003.

Rothman, L. S., Gamache, R. R., Barbe, A., Goldman, A., Gillis, J. R., Brown, L. R., Toth, R. A., Falud, J. M., and Camypeyret, C.: AFGL atmospheric absorption-line parameters compilation – 1982 edition, Appl. Optics, 22, 2247–2256, 1983.

Rothman, L. S., Gamache, R. R., Tipping, R. H., Rinsland, C. P., Smith, M. A. H., Benner, D. C., Devi, V. M., Flaud, J.-M., Camy-Peyret, C., and Perrin, A.: The HITRAN molecular database: Editions of 1991 and 1992, J. Quant. Spectrosc. Radiat. Transfer, 48, 469–507, 1992.

Rothman, L. S., Barbe, A., Benner, D. C., Brown, L. R., Camy-Peyret, C., Carleer, M. R., Chance, K., Clerbaux, C., Dana, V., Devi, V. M., Fayt, A., Flaud, J.-M., Gamache, R. R., Goldman, A., Jacquemart, D., Jucks, K. W., Lafferty, W. J., Mandin, J.-Y., Massie, S. T., Nemtchinov, V., Newnham, D. A., Perrin, A., Rinsland, C. P., Schroeder, J., Smith, K. M., Smith, M. A. H., Tang, K., Toth, R. A., Auwera, J. V., Varanasi, P., and Yoshino, K.: The HITRAN molecular spectroscopic database: Edition of 2000 including updates of 2001. J. Quant. Spectrosc. Radiat. Transfer, 82, 5–44, 2003.

Rothman, L. S., Jacquemart, D., Barbe, A., Chris Benner, D., Birk, M., Brown, L. R., Carleer, M. R., Chackerian, C., Chance, K., Coudert, L. H., Dana, V., Devi, V. M., Flaud, J.-M., Gamache, R. R., Goldman, A., Hartmann, J.-M., Jucks, K. W., Maki, A. G., Mandin, J.-Y, Massie, S. T., Orphal, J., Perrin, A., Rinslad, C. P., Smigh, M. A. H., Tennyson, J., Tolchenov, R. N., Toth, R. A., Vander Auwera, J., Varanasi, P., and G. Wagner: The HITRAN 2004 molecular spectroscopic database, J. Quant. Spectrosc. Radiat. Transfer, 96, 139–204, doi:10.1016/j.jqsrt.2004.10.008, 2005.

Rothman, L. S., Gordon, I. E., Barbe, A., Benner, D. C., Bernath, P. F., Birk, M., Boudon, V., Brown, L. R., Campargue, A., Champion, J.-P., Chance, K., Coudert, L. H., Dana, V., Devi, V. M., Fally, S., Flaud, J.-M., Gamache, R. R., Goldman, A., Jacquemart, D., Kleiner, I., Lacome, N., Lafferty, W. J., Mandin, J.-Y., Massie, S. T., Mikhailenko, S. N., Miller, C. E., Moazzen-Ahmadi, N., Naumenko, O. V., Nikitin, A. V., Orphal, J., Perevalov, V. I., Perrin, A., Predoi-Cross, A., Rinsland, C. P., Rotger, M., Šimečcková, M., Smith, M. A. H., Sung, K., Tashkun, S. A., Tennyson, J., Toth, R. A., Vandaele, A. C., and Vander Auwera, J.: The HITRAN 2008 molecular spectroscopic database, J. Quant. Spectrosc. Radiat. Transfer, 110, 533–572, 2009.

Russell, P. B., S. A. Kinne, and R. W. Bergstrom: Aerosol climate effects: Local radiative forcing and column closure experiments, J. Geophys. Res., 102, 9397–9408, 1997.

Schulz, M., Textor, C., Kinne, S., Balkanski, Y., Bauer, S., Berntsen, T., Berglen, T., Boucher, O., Dentener, F., Guibert, S., Isaksen, I. S. A., Iversen, T., Koch, D., Kirkevåg, A., Liu, X., Montanaro, V., Myhre, G., Penner, J. E., Pitari, G., Reddy, S., Seland, Ø., Stier, P., and Takemura, T.: Radiative forcing by aerosols as derived from the AeroCom present-day and pre-industrial simulations, Atmos. Chem. Phys., 6, 5225–5246, doi:10.5194/acp-6-5225-2006, 2006.

Schulz, M., Chin, M., and Kinne S.: The Aerosol Model Comparison Project, AeroCom, Phase II: Clearing Up Diversity, IGAC Newsletter, No 41, May 2009.

Slingo, A. and Schrecker, H. M.: On the shortwave radiative properties of stratiform water clouds, Q. J. Roy. Meteor. Soc., 108, 407–426, 1982.

Solomon, S., Qin, D., Manning, M., Marquis, M., Averyt, K., Tignor, M., Miller, H., and Chen, Z.: Technical summary, in Climate Change 2007: The Physical Science Basis. Contribution of Working Group I to the Fourth Assessment Report of the Intergovernmental Panel on Climate Change, edited by: Solomon, S., Qin, D., Manning, M., Marquis, M., Averyt, K., Tignor, M., Miller, H., and Chen, Z., 19–94, Cambridge Univ. Press, Cambridge, UK, 2007.

Stamnes, K., Tsay, S. C., Wiscombe, W., and Jayaweera, K.: A numerically stable algorithm for discrete-ordinate-method radiative transfer in multiple scattering and emitting layered media. Appl. Opt., 27, 2502–2509, 1988.

Stier, P., Schutgens, N. A. J., Bian, H., Boucher, O., Chin, M., Ghan, S., Huneeus, N., Kinne, S., Lin, G., Myhre, G., Penner, J. E., Randles, C., Samset, B., Schulz, M., Yu, H., and Zhou, C.: Host model uncertainties in aerosol radiative forcing estimates: results from the AeroCom prescribed intercomparison study, Atmos. Chem. Phys. Discuss., 12, 25487–25549, doi:10.5194/acpd-12-25487-2012, 2012.

Stokes, G. M. and Schwartz, S. E.: The Atmospheric Radiation Measurement (ARM) Program: Programmatic background and design of the cloud and Radiation Testbed, B. Amer. Meteor. Soc., 75, 1201–1221, 1994.

Sun, Z.: Development of the Sun-Edwards-Slingo Radiation Scheme (SES2). CAWCR Technical Report No. 009, Centre for Australian Weather and Climate Research, Australian Bureau of Meteorology, 94 pp., 2008.

Sun, Z. and Rikus, L.: Improved application of exponential sum fitting transmissions to inhomogeneous atmosphere, J. Geophy. Res., 104, 6291–6303, 1999.

Tarasova, T. A. and Fomin, B. A.: Solar radiation absorption due to water vapor: Advanced broadband parameterizations, J. Appl. Met., 39, 1947–1951, 2000.

Textor, C., Schulz, M., Guibert, S., Kinne, S., Balkanski, Y., Bauer, S., Berntsen, T., Berglen, T., Boucher, O., Chin, M., Dentener, F., Diehl, T., Easter, R., Feichter, H., Fillmore, D., Ghan, S., Ginoux, P., Gong, S., Grini, A., Hendricks, J., Horowitz, L., Huang, P., Isaksen, I., Iversen, I., Kloster, S., Koch, D., Kirkevåg, A., Kristjansson, J. E., Krol, M., Lauer, A., Lamarque, J. F., Liu, X., Montanaro, V., Myhre, G., Penner, J., Pitari, G., Reddy, S., Seland, Ø., Stier, P., Takemura, T., and Tie, X.: Analysis and quantification of the diversities of aerosol life cycles within AeroCom, Atmos. Chem. Phys., 6, 1777–1813, doi:10.5194/acp-6-1777-2006, 2006.

Textor, C., Schulz, M., Guibert, S., Kinne, S., Balkanski, Y., Bauer, S., Berntsen, T., Berglen, T., Boucher, O., Chin, M., Dentener, F., Diehl, T., Feichter, J., Fillmore, D., Ginoux, P., Gong, S., Grini, A., Hendricks, J., Horowitz, L., Huang, P., Isaksen, I. S. A., Iversen, T., Kloster, S., Koch, D., Kirkevåg, A., Kristjansson, J. E., Krol, M., Lauer, A., Lamarque, J. F., Liu, X., Montanaro, V., Myhre, G., Penner, J. E., Pitari, G., Reddy, M. S., Seland, Ø., Stier, P., Takemura, T., and Tie, X.: The effect of harmonized emissions on aerosol properties in global models – an AeroCom experiment, Atmos. Chem. Phys., 7, 4489–4501, doi:10.5194/acp-7-4489-2007, 2007.

Toon, O. B., McKay, C. P., Ackerman, T. P., and Santhanam, K.: Rapid Calculation of Radiative Heating Rates and Photodissociation Rates in Inhomogeneous Multiple Scattering Atmospheres, J. Geophys. Res., 94, 16287–16301, doi:10.1029/JD094iD13p16287, 1989.

van de Hulst, H. C.: Multiple Light Scattering: Tables, Formulas, and Applications, vol. 1, Academic Press, San Diego, CA, USA, 436 pp., 1980.

Vardavas, I. M. and Taylor, F. W.: Radiation and Climate: Atmospheric energy budget from satellite remote sensing, Int. Ser. Monogr. Phys., 138, Oxford University Press, Oxford, UK, 512 pp., 2011.

Vigroux, E.: Contribution à l'étude experimentale de l'absorption de l'ozone, Ann. Phys., 8, 709–762, 1953.

Walters, D. N., Best, M. J., Bushell, A. C., Copsey, D., Edwards, J. M., Falloon, P. D., Harris, C. M., Lock, A. P., Manners, J. C., Morcrette, C. J., Roberts, M. J., Stratton, R. A., Webster, S., Wilkinson, J. M., Willett, M. R., Boutle, I. A., Earnshaw, P. D., Hill, P. G., MacLachlan, C., Martin, G. M., Moufouma-Okia, W., Palmer, M. D., Petch, J. C., Rooney, G. G., Scaife, A. A., and Williams, K. D.: The Met Office Unified Model Global Atmosphere 3.0/3.1 and JULES Global Land 3.0/3.1 configurations, Geosci. Model Dev., 4, 919–941, doi:10.5194/gmd-4-919-2011, 2011.

Wang, H. and R. T. Pinker: Shortwave radiative fluxes from MODIS: Model development and implementation, J. Geophys. Res., 114, D20201, doi:10.1029/2008JD010442, 2009.

Wei Xiaodong and Zhang Hua: Analysis of optical properties of nonspherical dust aerosols, Acta Opt. Sin., 31, 0501002-1, 2011.

Wiscombe, W. J. and Evans, J. W.: Exponential-sum fitting of radiative transmission functions, J. Comput. Phys., 24, 416–444, 1977.

WMO: Global ozone research and monitoring project. Report 16, Atmospheric Ozone. WMO, Geneva, Switzerland, 1985.

Zdunkowski, W. G., Welch, R. M., and Korb, G.: An investigation of the structure of typical two-stream methods for the calculation of solar fluxes and heating rates in clouds, Beiträge Phys. Atmosph., 53, 147–166, 1980.

Zhang, H., Nakajima, T., Shi G. Y., Suzuki, T., and Imasu, R.: An optimal approach to overlapping bands with correlated-k distribution method and its application to radiative transfer calculations. J. Geophys. Res., 108, 4641, doi:10.1029/2002JD003358, 2003.

Zhang, F., Zeng, Q. C., Gu, Y., and Liou, K. N.: Parameterization of the absorption of the H_2O continuum, CO_2, O_2, and other trace gases in the Fu-Liou radiation program, Adv. Atmos. Sci., 22, 545–558, 2005.

Zhang, H., Shi, G. Y., Nakajima., T., and Suzuki., T.: The effects of the choice of the k-interval number on radiative calculations, J. Quant. Spectrosc. Radiat. Transfer, 98, 31–43, 2006a.

Zhang, H., Suzuki, T., Nakajima, T., Shi, G. Y., Zhang, X. Y. and Liu, Y.: The effects of band division on radiative calculations. Opt. Eng., 45, 016002, doi:10.1117/1.2160521, 2006b.

Zhang, H., Shen, Z., Wei, X., Zhang, M., and Li, Z.: Comparison of optical properties of nitrate and sulfate aerosol and the direct radiative forcing due to nitrate in China, Atmos. Res., 113, 113–125, 2012.

Zhang, F., Liang, X.-Z., Zeng, Q. C., Gu, Y., and Su, S. J.: Cloud-Aerosol-Radiation (CAR) Ensemble Modeling System: Overall accuracy and efficiency. Adv. Atmos. Sci., doi:10.1007/s00376-012-2171-z, 2013.

Atmos. Chem. Phys., 13, 7895–7901, 2013
www.atmos-chem-phys.net/13/7895/2013/
doi:10.5194/acp-13-7895-2013

Atmospheric Chemistry and Physics Open Access

Influence of observed diurnal cycles of aerosol optical depth on aerosol direct radiative effect

A. Arola[1], T. F. Eck[2,3], J. Huttunen[1], K. E. J. Lehtinen[1], A. V. Lindfors[1], G. Myhre[4], A. Smirnov[5,3], S. N. Tripathi[6], and H. Yu[7,3]

[1]Finnish Meteorological Institute, P.O. Box 1627, 70211 Kuopio, Finland
[2]Universities Space Research Association, Columbia, MD, USA
[3]NASA Goddard Space Flight Center, Greenbelt, MD, USA
[4]Center for International Climate and Environmental Research – Oslo (CICERO), Oslo, Norway
[5]Sigma Space Corporation, Lanham, MD, USA
[6]Department of Civil Engineering, Indian Institute of Technology, Kanpur 208016, India
[7]Earth System Science Interdisciplinary Center, University of Maryland, College Park, MD, USA

Correspondence to: A. Arola (antti.arola@fmi.fi)

Received: 22 February 2013 – Published in Atmos. Chem. Phys. Discuss.: 19 April 2013
Revised: 28 June 2013 – Accepted: 6 July 2013 – Published: 15 August 2013

Abstract. The diurnal variability of aerosol optical depth (AOD) can be significant, depending on location and dominant aerosol type. However, these diurnal cycles have rarely been taken into account in measurement-based estimates of aerosol direct radiative forcing (ADRF) or aerosol direct radiative effect (ADRE). The objective of our study was to estimate the influence of diurnal aerosol variability at the top of the atmosphere ADRE estimates. By including all the possible AERONET sites, we wanted to assess the influence on global ADRE estimates. While focusing also in more detail on some selected sites of strongest impact, our goal was to also see the possible impact regionally. We calculated ADRE with different assumptions about the daily AOD variability: taking the observed daily AOD cycle into account and assuming diurnally constant AOD. Moreover, we estimated the corresponding differences in ADREs, if the single AOD value for the daily mean was taken from the the Moderate Resolution Imaging Spectroradiometer (MODIS) Terra or Aqua overpass times, instead of accounting for the true observed daily variability. The mean impact of diurnal AOD variability on 24 h ADRE estimates, averaged over all AERONET sites, was rather small and it was relatively small even for the cases when AOD was chosen to correspond to the Terra or Aqua overpass time. This was true on average over all AERONET sites, while clearly there can be much stronger impact in individual sites. Examples of some selected sites demonstrated that the strongest observed AOD variability (the strongest morning afternoon contrast) does not typically result in a significant impact on 24 h ADRE. In those cases, the morning and afternoon AOD patterns are opposite and thus the impact on 24 h ADRE, when integrated over all solar zenith angles, is reduced. The most significant effect on daily ADRE was induced by AOD cycles with either maximum or minimum AOD close to local noon. In these cases, the impact on 24 h ADRE was typically around 0.1–0.2 W m^{-2} (both positive and negative) in absolute values, 5–10 % in relative ones.

1 Introduction

Aerosols affect the earth's climate directly by scattering and absorbing radiation (direct aerosol effect) and by affecting cloud properties (indirect aerosol effect). Currently, aerosol forcing is the largest uncertainty in assessing the anthropogenic climate change. In IPCC (2007), the scientific understanding of direct and indirect aerosol climate forcing has been designated as "medium-low" and "low", respectively. Therefore, regardless of the recent progress, also the estimate of direct forcing still contains significant uncertainties (Kahn, 2012). Indeed, the study by Loeb and Su (2010) suggested that the quantitative uncertainties reported by the

IPCC (2007), which were based on the model diversity rather than on aggregated error, are clearly underestimated.

The diurnal variability in aerosol optical depth (AOD) can be significant, depending on location and dominant aerosol type (e.g., Smirnov et al., 2002; Eck et al., 2003; Zhang et al., 2012). These diurnal cycles have rarely been taken into account in measurement-based estimates of aerosol direct radiative forcing (ADRF) or aerosol direct radiative effect (ADRE), the former taking into account the anthropogenic aerosols and the latter both anthropogenic and natural aerosols. However, Christopher et al. (2006) reported that the diurnal variation of dust aerosols could be important for dust radiative forcing calculations. The objective of this study is to provide an estimate of the impact of diurnal AOD variability on the estimates of ADRE at the top of the atmosphere (TOA). This is the first time that the importance of diurnal AOD cycle on ADRE calculations is assessed using data from large number of Aerosol Robotic Network (AERONET) sites. We included all the sites from AERONET (Holben et al., 1998), thus covering a wide range of conditions. We calculated the mean diurnal AOD cycle on a seasonal basis, for each site with enough data, and the related impact of this cycle on TOA ADRE using radiative transfer modeling.

2 Data and methods

2.1 AERONET data

AERONET is a globally distributed network of automatic sun and sky scanning radiometers that measure at several wavelengths, typically centered at 0.34, 0.38, 0.44, 0.50, 0.675, 0.87, 0.94, and 1.02 µm. Each band has a full width of approximately 0.010 µm at half maximum (FWHM), except for the UV channels that have a FWHM bandpass of 0.002 µm. These spectral bands are utilized in the direct sun measurements, while four of them are used for the sky radiance: 0.44, 0.67, 0.87, and 1.02 µm. Spectral aerosol optical depth (AOD) is obtained from direct sun measurements, and inversion products of other aerosol optical properties, such as single scattering albedo (SSA), refractive indices and the column-integrated aerosol size distributions above the measurement site are provided at the sky radiance wavelengths (Holben et al., 1998).

In our study, in order to form the diurnal patterns of AOD, we used level 2.0 direct sun data (quality assured; Smirnov et al., 2000) of AOD at 500 nm, which has accuracy of 0.01 at optical air mass (m) of 1 (Eck et al., 1999) and higher accuracy at larger air mass, proportional to $1\,m^{-1}$. Measurements of AOD are made from air mass of 05:00 in the morning to air mass of 17:00 in the evening. The other wavelengths for radiative transfer calculations were then estimated using the average Ångström exponent based on 380–500 nm (from AERONET direct sun product). The other optical properties

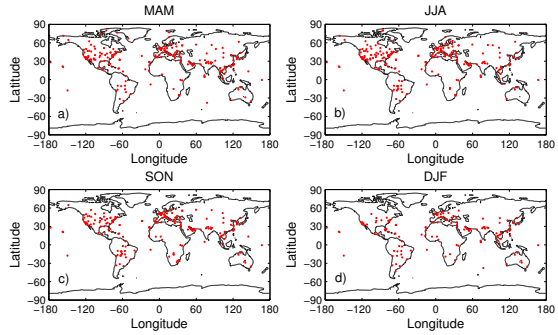

Fig. 1. Included AERONET sites in each season: **(a)** MAM, **(b)** JJA, **(c)** SON, and **(d)** DJF.

(SSA and asymmetry parameter at four wavelengths) from the inversion products (Dubovik et al., 2002) were used in radiative transfer calculations, as explained in more detail in the following section.

All individual observations of AOD at 500 nm for a specific day were taken, and the departures from the daily mean AOD were calculated, requiring that there is at least one AOD observation both before and after the local solar noon. Eventually, these hourly departures were averaged for each hour of local solar time, to form the average daily cycle of departures for each site; an example is given by Fig. 2, which is discussed in more detail in the Results section. All the days were included and analyzed on a seasonal basis: March–May (MAM), June–August (JJA), September–November (SON), and December–February (DJF). We required at least 30 days of AOD data within a multi-year season to form the diurnal AOD pattern. The number of included sites is 224, 253, 208, and 144 for MAM, JJA, SON, and DJF, respectively. The selected sites in each season are shown in the Fig. 1.

2.2 Calculation of the radiative effect

The radiative transfer simulations were performed with the libRadtran package (Mayer and Kylling, 2005). Radiative transfer models of libRadtran have been thoroughly validated and checked against both measurements and other models, for instance recently in Randles et al. (2013). We used two-stream solver and so-called correlated k approach with bands from 240.1185 nm to 3991.003 nm. For the vertical profile, we assumed aerosol extinction decreasing exponentially with height. The AERONET measurements were used as input to these calculations to estimate the diurnally averaged clear-sky TOA ADRE for all AERONET sites that had enough data to form the diurnal AOD pattern as described in the previous section. We performed the calculations with a one-hour time step over a 24 h diurnal cycle with solar insolation of the 15th day of the middle month of the season to provide the seasonal

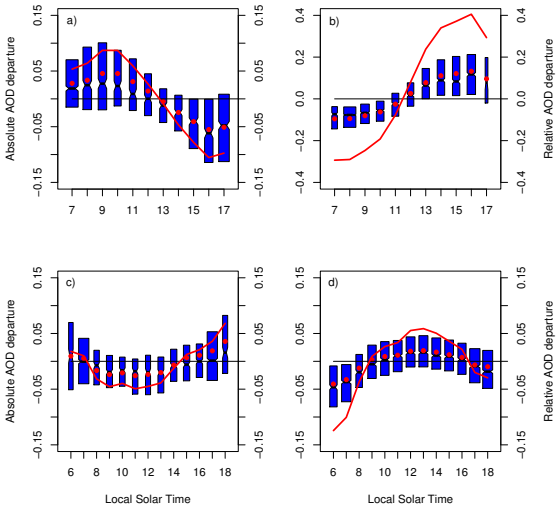

Fig. 2. AOD departures from the daily mean. Box plots give the medians (with 5th/95th percentiles) of absolute AOD departure, and the red solid points provide the mean, in addition. The red line is the relative departure in right axis; the absolute departure in each hour divided by the overall mean AOD of each season and site. The following sites and seasons are shown: **(a)** Silpakorn University, Thailand MAM; **(b)** Mexico City, Mexico, DJF; **(c)** Hamim, United Arab Emirates, JJA; and **(d)** Blida, Algeria, JJA.

averages. The TOA ADRE calculations were performed with different assumptions about the daily AOD variability:

1. diurnally varying AOD according to observations;
2. no diurnal AOD variation, AOD = daily averaged AOD;
3. no diurnal AOD variation, AOD = observed AOD at the MODIS Terra/Aqua overpass time.

Since AODs from the Moderate Resolution Imaging Spectroradiometer (MODIS) data are widely used in ADRF and ADRE calculations, we also wanted to estimate the impact on ADRE, if the single AOD value for the daily mean is taken from the Terra or Aqua overpass times, instead of accounting for the true observed daily variability.

In the following, we will mainly concentrate on the difference between two ADRE estimates; with different assumptions about the diurnal evolution of aerosol optical depth. Therefore, arguably the absolute value of the ADRE in our calculations is less important than the magnitude of the difference between the two ADRE estimates, affected by the diurnal AOD variability only. Regardless of this, we attempted to form the input data for each site to be as site-representative and realistic as possible. Therefore, for instance, we applied the same solar zenith angle dependent MODIS-based surface albedo (black-sky albedo) for each site as that used in the AERONET retrievals (at four wavelengths of the inversion product) as briefly described in Eck et al. (2008). Therefore, in our RT calculations, also the surface albedo exhibited diurnal variability. The surface albedo was linearly interpolated between the inversion data wavelengths. The surface albedo value at 440 nm was extrapolated to the shorter wavelengths as well, while the wavelengths larger than 1020 nm were linearly extrapolated so that the surface albedo at 5 µm is decreased to 0.01.

Seasonally averaged single scattering albedo (SSA) and asymmetry parameter were taken at four wavelengths as well from the inversion product and were interpolated and extrapolated to cover the full range of the solar spectrum. We used level 1.5 inversion product, in order to obtain site-specific SSA and asymmetry parameter values also for those sites where the prevailing conditions of AOD at 440 nm are below 0.4 (which is the AOD limit for the level 2.0 product). However, when we selected the data from the level 1.5 inversion product, we applied all the other level 2.0 AERONET criteria except for the AOD threshold. There are two other justifications for our choice to use level 1.5 product. First, we are interested in ADRE, which decreases as AOD decreases. Thus, although the uncertainty of SSA increases with decreasing AOD, its impact on our calculations decreases as well. Second, and more importantly, our specific interest is in the difference between two ADRE simulations, when the only difference is the diurnal pattern of aerosol optical depth. Therefore, the importance of SSA is further reduced. Nevertheless, we wanted to form as realistic and site-specific input parameters as possible for our ADRE calculations. In addition to aerosol optical properties, also the columnar water vapor measurements (as seasonal averages) from AERONET were used in the calculations.

3 Results

Figure 2 shows an example of observed diurnal AOD patterns from four sites. The data are represented as box plots (with 5 and 95 percentiles), in order to give not only the median, but also an impression about the variability of departures in each hour. Moreover, the boxes are drawn with widths proportional to the square roots of the number of observations in each hour. In addition to the medians, which are given by the box plots, the mean departures in each hour are indicated by the solid red points. The red line gives the mean relative departure, showing the absolute departure in each hour divided by the overall mean AOD at 500 nm in that particular season. This particular choice of sites is based on the inspection of all the results, to select two representative examples of sites with significant AOD variability (Silpakorn University, Mexico City) and less significant diurnal AOD pattern (Hamim, Blida), but the latter having a stronger impact on TOA ADRE (Hamim, Blida), as explained in further detail below.

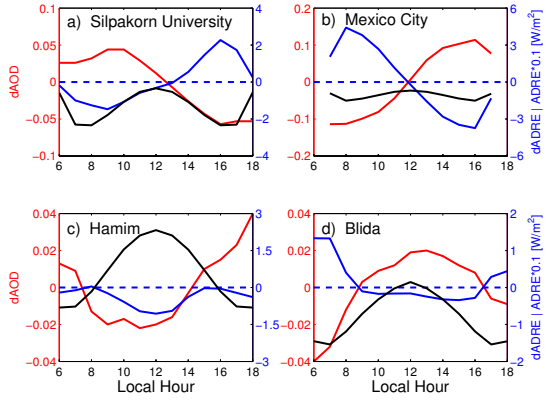

Fig. 3. Hourly AOD departures from the daily mean in red (dAOD, left side y axis) and the instantaneous difference between two ADRE runs (assuming the observed daily AOD variability and with mean daily AOD) in blue (dADRE, right side y axis). Black line shows ADRE with true diurnal AOD cycle (right side y axis); ADRE is multiplied by 0.1 to match the common y axis with dADRE better. Same sites and seasons (and in the same order) as in the Fig. 2.

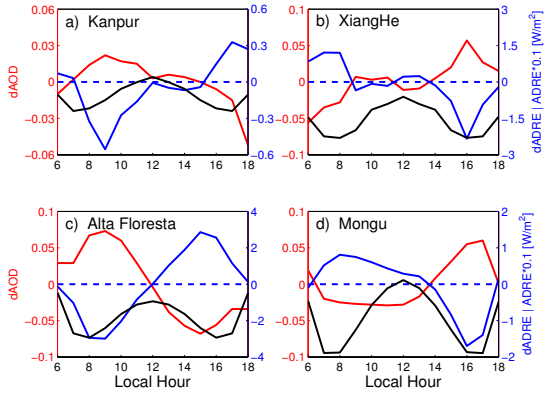

Fig. 4. As in Fig. 3, but for the following sites and seasons: **(a)** Kanpur, India, MAM; **(b)** Xianghe, China, MAM; **(c)** Alta Floresta, Brazil, SON; and **(d)** Mongu, Zambia, SON. Black line shows ADRE with true diurnal AOD cycle (right side y axis); ADRE is multiplied by 0.1 in all other sites, but by 0.01 in Kanpur.

There can be several different potential reasons for site-specific diurnal AOD variability, and those have been discussed in more detail in previous studies (e.g., Smirnov et al., 2002; Eck et al., 2003; Zhang et al., 2012). For instance, Gautam et al. (2012) reported a similar diurnal cycle for Silpakorn University, which is shown in Fig. 2. They speculated that one reason for the enhanced aerosol loading in the morning in this biomass burning region may be associated with smoke transport through the night.

Figure 3 shows the same sites as in Fig. 2, and in addition to AOD cycle, the time evolution of the instantaneous difference between two ADRE simulations (dADRE) is also shown, in order to illustrate the impact of diurnal AOD variability on diurnally averaged ADRE estimates. Moreover, ADRE with true diurnal AOD cycle is included (black line), to make it easier to interpret the dADRE pattern, particularly when ADRE can change from cooling to warming. ADRE is multiplied by 0.1 to make it better match the common y scale. Two upper panels show sites with a significant diurnal variability, which however does not translate into equally significant impact on 24 h ADRE. This is the case, for instance, in Mexico City, which has the strongest morning to afternoon contrast in the measured AOD out of all AERONET sites (note its different y axis scale). However, when temporally integrated over the day, the impact in the morning is compensated in the afternoon, which can be seen in Fig. 3b: although there is a positive ADRE difference before local solar noon, which is about 4.5 W m^{-2} at the maximum at 08:00 local solar time, there is a very similar pattern of opposite sign in the afternoon. Therefore, the integrated difference in 24 h ADRE is eventually only 0.041 W m^{-2}.

The bottom panels of Fig. 3, on the other hand, illustrate two sites with clearly less significant daily AOD cycle, yet resulting in more significant impact on the estimate of diurnally averaged ADRE. The main reason for this enhanced impact on dADRE in Hamim (-0.213 W m^{-2}), for instance, is that the hours of positive dAOD correspond mostly to those solar zenith angles when ADRE is negative (cooling effect), while during the negative dAOD hours (around noon) ADRE is positive. Therefore, the instantaneous dADRE during almost all the hours is negative (it is only slightly positive at 08:00 local hour), and thus there is no similar compensation to that of the sites shown in the upper panels. In Blida, there is somewhat similar impact, however with the opposite AOD cycle; the largest instantaneous dADRE is formed in the morning hours, when ADRE is clearly negative, which then is not much compensated around noon (when dAOD is positive), since ADRE is clearly reduced and becomes even slightly positive at local noon.

Figure 4 shows four additional AERONET sites that all have long data records, which have been also widely analyzed before. Therefore, we consider it interesting to show here also their diurnal AOD patterns and the impact of these patterns on the calculation of aerosol direct radiative effect. The upper panel plots show two sites, affected heavily by urban pollution (Kanpur in India and Xianghe in China) and additionally by desert dust primarily in MAM (Eck et al., 2010), while the lower panel plots show two sites affected seasonally by strong biomass burning. Note that ADRE (black line) is multiplied by 0.01 in Kanpur and by 0.1 in other sites. Although all these sites are influenced by strong seasonally varying aerosol emissions, it is evident

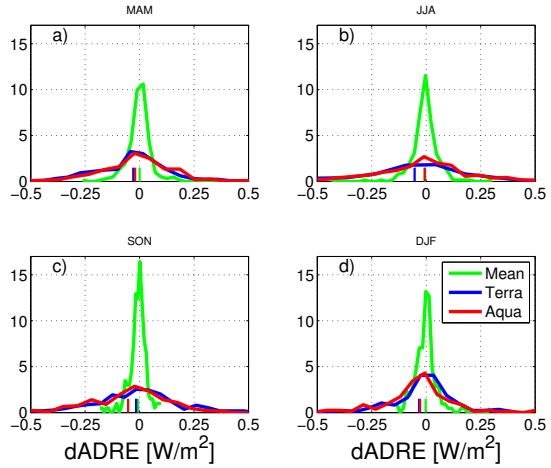

Fig. 5. Histograms of all AERONET sites on a seasonal basis: **(a)** MAM, **(b)** JJA, **(c)** SON, and **(d)** DJF. Green line is ADRE difference between two AOD assumptions: with observed diurnal variability and assuming daily mean AOD. In the blue line case, AOD is taken from the observed diurnal cycle at Terra overpass time and in the red line case at Aqua overpass time. The histograms are scaled so that the area below each curve equals unity.

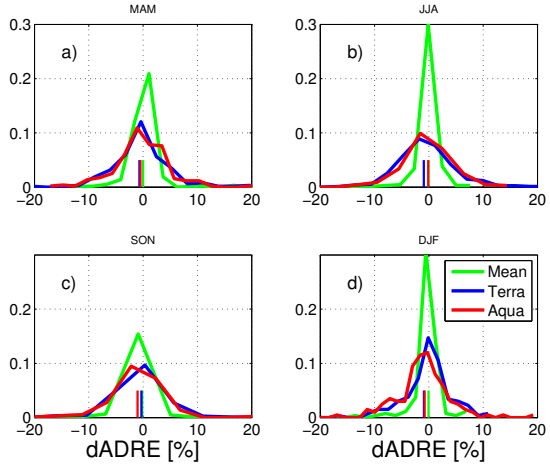

Fig. 6. As in Fig. 5, but for relative dADRE difference (dADRE divided by ADRE assuming true diurnal AOD variability).

(also by the data of other seasons, not shown here) that the diurnal AOD variability does not draw a significant influence on daily averaged direct aerosol effect; it is only slightly negative for all shown cases: $-0.026\,\mathrm{W\,m^{-2}}$, $-0.053\,\mathrm{W\,m^{-2}}$, $-0.014\,\mathrm{W\,m^{-2}}$, and $-0.016\,\mathrm{W\,m^{-2}}$, for Kanpur, Xianghe, Alta Floresta, and Mongu, respectively.

Table 1 provides the ADRE differences in these eight sites for all seasons. In addition, it provides the TOA ADRE values (assuming diurnally varying AOD), to allow an impression about the relative impact of diurnal AOD variability on daily averaged TOA ADRE, which is given also in percentage in the last column. Relatively, the AOD daily variability does not result in very large impact on TOA ADRE. For example, in Hamim (JJA) ADRE is slightly positive (due to the combined effect of high surface albedo and relatively low SSA), which is overestimated by $0.213\,\mathrm{W\,m^{-2}}$ (7.3 %), if constant diurnally averaged AOD is used. Generally, however, the relative impact is lower. And the overall influence, when including a large number of sites, is relatively small. This is evident also from Table 1, which includes additionally the overall statistics of all sites in each season.

The diurnal AOD cycle cannot be captured by using data from polar-orbiting satellites. Therefore, those absolute and relative ADRE differences are also given in the Table 1, when the single AOD value (to represent the daily mean) is taken from MODIS Terra (around 10:30 local solar time) or Aqua (around 13:30 local solar time) overpass times. Now there are clearly cases of much larger influence in daily averaged dADRE. For instance, in Mexico City and DJF season, which exhibited close to zero impact ($0.041\,\mathrm{W\,m^{-2}}$) due to the diurnal AOD variability compared to a daily mean, the difference between ADRE with daily AOD variability and AOD taken at satellite overpass time is $-0.83\,\mathrm{W\,m^{-2}}$ and $0.98\,\mathrm{W\,m^{-2}}$ for Terra and Aqua, respectively.

Figure 5 summarizes the difference in daily averaged ADRE, using different assumptions about diurnal AOD variability, including all AERONET sites of each season that had enough data to form the diurnal AOD cycle. Small vertical lines in each color indicate the mean of the distribution. It can be seen that the mean difference in ADRE, due to the diurnal AOD cycle, over all the available AERONET sites is very close to zero. However, there are sites with an impact of around $0.1\,\mathrm{W\,m^{-2}}$ (both positive and negative), and examples of those are given in Figs. 1–4.

Red and blue curves of Fig. 5 illustrate the impact on the 24 h ADRE, if AOD is taken either at MODIS Terra (around 10:30 local solar time) or Aqua (around 13:30 local solar time) overpass times. For instance in Mexico City and for DJF season, the difference between ADRE with daily AOD variability and AOD taken at satellite overpass time is quite significant. However, the overall mean of these cases (average over all sites) is relatively close to zero, indicating that the use of either Terra or Aqua AOD data does not result in significant systematic global bias, which would be caused by an unaccounted diurnal AOD cycle. The comparison of the subplots of Fig. 5, on the other hand, suggests a slight seasonal dependence; in JJA season the use of Aqua (afternoon) overpass data and in SON Terra data (before noon) better captures the prevailing AOD cycles, from the point of view of their impact on diurnally averaged ADRE. Figure 6 shows the relative dADRE results of all the sites. They are es-

Table 1. Diurnally averaged ADRE by the diurnally varying AOD; absolute and relative difference between two ADRE simulations, dADRE, assuming the observed daily AOD variability and the following three cases: (1) observed mean daily AOD, (2) AOD at the Terra overpass time, and (3) AOD at Aqua overpass time.

Site	Season	ADRE ($W\,m^{-2}$)	dADRE mean AOD ($W\,m^{-2}$)/(%)	dADRE AOD at Aqua time ($W\,m^{-2}$)/(%)	dADRE AOD at Terra time ($W\,m^{-2}$)/(%)
Alta Floresta	DJF	−2.31	−0.004/−0.2	−0.103/−4.5	0.145/6.3
Blida	DJF	−3.02	0.061/2.0	0.233/7.7	−0.247/−8.2
Hamim	DJF	0.54	−0.041/−7.5	−0.048/−8.8	0.027/4.9
Kanpur	DJF	−8.14	−0.050/−0.6	0.136/1.7	0.117/1.4
Mexico City	DJF	−4.94	0.041/0.8	0.984/19.9	−0.827/−16.7
Mongu	DJF	−3.19	0.003/0.1	−0.134/−4.2	−0.118/−3.7
Silpakorn Univ	DJF	−8.71	−0.024/−0.3	0.109/1.3	−0.014/−0.2
Xianghe	DJF	−5.56	−0.008/−0.1	0.046/0.8	0.113/2.0
Alta Floresta	MAM	−1.67	0.028/1.7	0.025/1.5	0.075/4.5
Blida	MAM	−2.72	0.026/1.0	0.277/10.2	−0.016/−0.6
Hamim	MAM	2.28	−0.097/−4.3	−0.068/−3.0	−0.021/−0.9
Kanpur	MAM	−6.27	−0.026/−0.4	0.034/0.5	0.124/2.0
Mexico City	MAM	−5.28	0.057/1.1	1.125/21.3	−0.302/−5.7
Mongu	MAM	−3.86	0.008/0.2	0.051/1.3	−0.026/−0.7
Silpakorn Univ	MAM	−7.29	0.014/0.2	−0.188/−2.6	0.487/6.7
Xianghe	MAM	−8.67	−0.053/−0.6	−0.103/−1.2	0.024/0.3
Alta Floresta	JJA	−3.00	0.034/1.1	0.128/4.3	−0.025/−0.8
Blida	JJA	−4.53	0.093/2.1	0.369/8.1	0.245/5.4
Hamim	JJA	2.93	−0.213/−7.3	−0.070/−2.4	−0.052/−1.8
Kanpur	JJA	−7.48	−0.001/−0.0	0.008/0.1	0.107/1.4
Mexico City	JJA	−3.81	0.093/2.4	0.623/16.4	0.102/2.7
Mongu	JJA	−3.38	0.004/0.1	0.000/0.0	−0.140/−4.2
Xianghe	JJA	−12.99	0.012/0.1	0.099/0.8	0.038/0.3
Alta Floresta	SON	−9.79	−0.014/−0.1	−0.799/−8.2	0.710/7.2
Blida	SON	−3.71	0.008/0.2	0.264/7.1	−0.119/−3.2
Hamim	SON	1.44	−0.081/−5.6	−0.001/−0.1	−0.017/−1.2
Kanpur	SON	−9.18	−0.008/−0.1	0.149/1.6	0.004/0.0
Mexico City	SON	−3.85	0.050/1.3	0.795/20.6	−0.511/−13.3
Mongu	SON	−5.11	−0.016/−0.3	−0.063/−1.2	−0.327/−6.4
Silpakorn Univ	SON	−5.06	−0.015/−0.3	−0.061/−1.2	−0.057/−1.1
Xianghe	SON	−8.42	−0.016/−0.2	−0.035/−0.4	0.311/3.7
Mean of 144 sites	DJF	−3.57	−0.003/−0.07	−0.028/−0.8	−0.033/−0.9
Mean of 224 sites	MAM	−4.30	0.0002/0.04	−0.021/−0.5	−0.029/−0.7
Mean of 253 sites	JJA	−5.70	−0.007/−0.1	−0.006/−0.1	−0.053/−0.9
Mean of 208 sites	SON	−5.18	−0.008/−0.2	−0.053/−1.0	−0.016/−0.3

sentially within ±10 %, the major part being centered within ±5 %.

4 Conclusions

The influence of diurnal AOD variability on TOA ADRE estimates, exploiting a large number of AERONET sites, has not been estimated before. We formed the diurnal AOD cycles as departures from daily means, similar to Smirnov et al. (2002) and Zhang et al. (2012), for all the AERONET sites with a sufficient amount of data. We required at least 30 days of data to form the daily cycle, and this resulted in the following numbers of sites in our analysis: 224, 253, 208, and 144 for MAM, JJA, SON, and DJF, respectively. We then calculated the influence of these observed patterns on diurnally averaged aerosol direct radiative effect at the top of the atmosphere on a seasonal basis. In addition to the impact due to the observed AOD cycle itself, we also estimated similarly the influence, if using the AOD from satellite overpass times of either Terra or Aqua, as is commonly done.

Examples of some selected sites demonstrated that the strongest observed AOD variability (the strongest morning afternoon contrast) does not typically result in significant impact in 24 h TOA ADRE, compared to the use of daily mean AOD. In most of those cases, the morning and afternoon

AOD patterns are opposite, and thus the impact on 24 h ADRE, when integrated over all solar zenith angles, is clearly reduced (as illustrated in Fig. 3). The most significant effect on daily ADRE was induced by AOD cycle, with either maximum or minimum AOD close to local noon.

In individual sites there can be significant biases in ADRE estimates due to the impact of diurnal AOD variability. However, the mean impact of diurnal AOD variability on 24 h ADRE estimates, averaged over all AERONET sites, is rather small; it is relatively small even for the cases when AOD is taken either from Terra or Aqua overpass time. This latter finding suggests that, even though there can be more substantial influences regionally or in individual sites, overall the diurnal AOD variability is not a very strong factor influencing the diurnally averaged ADRE. Therefore, the use of AOD data from polar-orbiting satellites does not likely result in significant bias in global ADRE estimates, assuming AERONET sites represent well enough the possible diurnal variabilities.

Acknowledgements. We thank the principal investigators and their staff for establishing and maintaining the AERONET sites used in this study. Antti Arola wants to acknowledge the support from the Academy of Finland (through the grant "Researcher training and research abroad", decision No. 136996). S. N. Tripathi acknowledges the financial support from DST Climate Change Programme.

Edited by: E. Gerasopoulos

References

Christopher, S. A., Wang, J., Ji, Q., and Tsay, S.-C.: Estimation of diurnal shortwave dust aerosol radiative forcing during PRIDE, J. Geophys. Res., 108, 8596, doi:10.1029/2002JD002787, 2003.

Dubovik, O., Holben, B. N., Eck, T. F., Smirnov, A., Kaufman, Y. J., King, M. D., Tanr, D., and Slutsker, I.: Variability of absorption and optical properties of key aerosol types observed in worldwide locations, J. Atmos. Sci., 59, 590–608, 2002.

Eck, T., Holben, B., Reid, J. S., Dubovik, O., Smirnov, A., O'Neill, N. T., Slutsker, I., and Kinne, S.: Wavelength dependence of the optical depth of biomass burning urban and desert dust aerosols, J. Geophys. Res., 104, 31333–31349, doi:10.1029/1999JD900923, 1999.

Eck, T. F., Holben, B. N., Ward, D. E., Mukelabai, M. M., Dubovik, O., Smirnov, A., Schafer, J. S., Hsu, N. C., Piketh, S. J., Queface, A., Le Roux, J., Swap, R. J., and Slutsker, I.: Variability of biomass burning aerosol optical characteristics in southern Africa during the SAFARI 2000 dry season campaign and a comparison of single scattering albedo estimates from radiometric measurements, J. Geophys. Res., 108, 8477, doi:10.1029/2002JD002321, 2003.

Eck, T. F., Holben, B. N., Reid, J. S., Sinyuk, A., Dubovik, O., Smirnov, A., Giles, D., O'Neill, N. T., Tsay, S. C., Ji, Q., Al Mandoos, A., Ramzan, A., Reid, E. A., Schafer, J. S., Sorokine, M., Newcomb, W., and Slutsker, I.: Spatial and temporal variability of column-integrated aerosol optical properties in the southern Arabian Gulf and United Arab Emirates in summer, J. Geophys. Res., 113, D01204, doi:10.1029/2007JD008944, 2008.

Eck, T. F., Holben, B. N., Siniuk, A., Pinker, R. T., Goloub, P., Chen, H., Chatenet, B., Li, Z., Singh, R. P., Tripathi, S. N., Reid, J. S., Giles, D. M., Dubovik, O., O'Neill, N. T., and Smirnov, A.: Climatological aspects of the optical properties of fine/coarse mode aerosol mixtures, J. Geophys. Res., 115, D19205, doi:10.1029/2010JD014002, 2010.

Gautam, R., Hsu, N. C., Eck, T. F., Holben, B. N., Janjai, S., Jantarach, T., Tsay, S., and Lau, W. K.: Characterization of aerosols over the Indochina peninsula from satellite-surface observations during biomass burning pre-monsoon season, Atmos. Environ.,78, 51–59, doi:10.1016/j.atmosenv.2012.05.038, 2012.

Holben, B. N., Eck, T. F., Slutsker, I., Tanre, D., Buis, J. P., Setzer, A., Vermote, E., Reagan, J. A., Kaufman, Y., Nakajima, T., Lavenu, F., Jankowiak, I., and Smirnov, A.: AERONET – A federated instrument network and data archive for aerosol characterization, Rem. Sens. Environ., 66, 1–16, 1998.

Intergovernmental Panel on Climate Change (IPCC), Climate Change 2007: The Scientific Basis, Contribution of Working Group I to the Fourth Assessment Report of the Intergovernmental Panel on Climate Change, edited by: Solomon, S., Qin, D., Manning, M., Chen, Z., Marquis, M., Averyt, K. B., Tignor, M. and Miller, H. L., Cambridge Univ. Press, New York, 2007.

Kahn, R.: Reducing the Uncertainties in Direct Aerosol Radiative Forcing Surveys in Geophysics, Surv. Geophys., 33, 701–721, doi:10.1007/s10712-011-9153-z, 2012.

Loeb, N. G. and Su, W.: Direct aerosol radiative forcing uncertainty based on a radiative perturbation analysis, J. Climate, 23, 5288–5293, 2010.

Mayer, B. and Kylling, A.: Technical note: The libRadtran software package for radiative transfer calculations – description and examples of use, Atmos. Chem. Phys., 5, 1855–1877, doi:10.5194/acp-5-1855-2005, 2005.

Randles, C. A., Kinne, S., Myhre, G., Schulz, M., Stier, P., Fischer, J., Doppler, L., Highwood, E., Ryder, C., Harris, B., Huttunen, J., Ma, Y., Pinker, R. T., Mayer, B., Neubauer, D., Hitzenberger, R., Oreopoulos, L., Lee, D., Pitari, G., Di Genova, G., Quaas, J., Rose, F. G., Kato, S., Rumbold, S. T., Vardavas, I., Hatzianastassiou, N., Matsoukas, C., Yu, H., Zhang, F., Zhang, H., and Lu, P.: Intercomparison of shortwave radiative transfer schemes in global aerosol modeling: results from the AeroCom Radiative Transfer Experiment, Atmos. Chem. Phys., 13, 2347–2379, doi:10.5194/acp-13-2347-2013, 2013.

Smirnov, A., Holben, B. N., Eck, T. F., Dubovik, O., and Slutsker, I.: Cloud-Screening and Quality Control Algorithms for the AERONET Database, Remote Sens. Environ., 73, 337–349, doi:10.1016/S0034-4257(00)00109-7, 2000.

Smirnov, A., Holben, B. N., Eck, T. F., Slutsker, I., Chatenet, B., and Pinker, R. T.: Diurnal variability of aerosol optical depth observed at AERONET (Aerosol Robotic Network) sites, Geophys. Res. Lett., 29, 2115, doi:10.1029/2002GL016305, 2002.

Zhang, Y., Yu, H., Eck, T. F., Smirnov, A., Chin, M., Remer, L. A., Bian, H., Tan, Q., Levy, R., Holben, B. N., and Piazolla, S.: Aerosol daytime variations over North and South America derived from multiyear AERONET measurements, J. Geophys. Res., 117, D05211, doi:10.1029/2011JD017242, 2012.

Atmos. Chem. Phys., 14, 6103–6110, 2014
www.atmos-chem-phys.net/14/6103/2014/
doi:10.5194/acp-14-6103-2014

Atmospheric Chemistry and Physics
Open Access

Effect of water vapor on the determination of aerosol direct radiative effect based on the AERONET fluxes

J. Huttunen[1,2], A. Arola[1], G. Myhre[3], A. V. Lindfors[1], T. Mielonen[1], S. Mikkonen[2], J. S. Schafer[4], S. N. Tripathi[5], M. Wild[6], M. Komppula[1], and K. E. J. Lehtinen[1,2]

[1]Finnish Meteorological Institute, Kuopio, Finland
[2]Department of Applied Physics, University of Eastern Finland, Kuopio, Finland
[3]Center for International Climate and Environmental Research – Oslo (CICERO), Oslo, Norway
[4]NASA/Goddard Space Flight Center (GSFC), Biospheric Sciences Branch, Greenbelt, MD, USA
[5]Department of Civil Engineering, Indian Institute of Technology, Kanpur, India
[6]Institute for Atmospheric and Climate Science, ETH Zurich, Switzerland

Correspondence to: J. Huttunen (jani.huttunen@fmi.fi)

Received: 24 October 2013 – Published in Atmos. Chem. Phys. Discuss.: 10 January 2014
Revised: 14 May 2014 – Accepted: 16 May 2014 – Published: 20 June 2014

Abstract. The aerosol direct radiative effect (ADRE) is defined as the change in the solar radiation flux, F, due to aerosol scattering and absorption. The difficulty in determining ADRE stems mainly from the need to estimate F without aerosols, F^0, with either radiative transfer modeling and knowledge of the atmospheric state, or regression analysis of radiation data down to zero aerosol optical depth (AOD), if only F and AOD are observed. This paper examines the regression analysis method by using modeled surface data products provided by the Aerosol Robotic Network (AERONET). We extrapolated F^0 by two functions: a straight linear line and an exponential nonlinear decay. The exponential decay regression is expected to give a better estimation of ADRE with a few percent larger extrapolated F^0 than the linear regression. We found that, contrary to the expectation, in most cases the linear regression gives better results than the nonlinear. In such cases the extrapolated F^0 represents an unrealistically low water vapor column (WVC), resulting in underestimation of attenuation caused by the water vapor, and hence too large F^0 and overestimation of the magnitude of ADRE. The nonlinear ADRE is generally 40–50 % larger in magnitude than the linear ADRE due to the extrapolated F^0 difference. Since for a majority of locations, AOD and WVC have a positive correlation, the extrapolated F^0 with the nonlinear regression fit represents an unrealistically low WVC, and hence too large F^0. The systematic underestimation of F^0 with the linear regression is compensated by the positive correlation between AOD and water vapor, providing the better result.

1 Introduction

Significant uncertainties exist in the current estimates of aerosol effects on climate (IPCC, 2013). This holds also for the aerosol direct radiative effect (ADRE) and aerosol direct radiative forcing (ADRF). The ADRE defines the attenuation of the (cloud-free sky) surface solar radiation flux (F) due to aerosol scattering and absorption. Herein, we consider the solar radiation flux at the surface, although ADRE applies also for the longwave flux and above the atmosphere. In the definitions of ADRE and ADRF, effects relate to both anthropogenic and natural aerosol particles, while forcing refers to the impact of anthropogenic aerosol particles. Although, for example, Myhre (2009) recently showed an increment of the consistency between observation-based and global aerosol model estimates, with a reduction in the uncertainty of this effect, other studies (e.g., Loeb and Su, 2010) highlight that considerable uncertainties are still associated with ADRE, mainly due to the uncertainties in single scattering albedo (SSA). Satheesh and Ramanathan (2000) employed a method in which ADRE is estimated using the aerosol direct effect efficiency (ADREE), which is the ADRE normalized by the aerosol optical depth (AOD), and it is estimated by fitting a

straight line into surface solar flux and AOD observations. A linear dependence between aerosol attenuation and AOD has been commonly assumed when estimating ADRE (e.g., Kaufman et al., 2002; Bush and Valero, 2002, 2003; Dumka et al., 2006; Roger et al., 2006; di Sarra et al., 2008; Garcia et al., 2009; Satheesh et al., 2010). Typical attenuation of radiation intensity, however, implies nonlinear decay, as considered by for example Conant et al. (2003), Markowicz et al. (2008) and Kudo et al. (2010). Thus, a linear fit to F and AOD data may result in an incorrect extrapolation of F^0.

The aim of this paper is to examine the uncertainties involved in estimating ADRE, both using the linear fitting method and a nonlinear approach if F and AOD data are available from surface or satellite measurements. For this, we use Aerosol Robotic Network (AERONET) products (http://aeronet.gsfc.nasa.gov/) from all available AERONET stations, which cover different aerosol types and surface reflectance properties and provide modeled surface solar radiation fluxes also. We conducted our analysis using these modeled fluxes since they represent realistically enough the aerosol-induced relative changes in F and furthermore give an estimate for F^0, which is self-consistent within the selected F (AOD) data set. As AERONET provides an estimation of F^0, we can compare the estimations immediately with the baseline (AERONET). Special attention is paid to the possible effect of water vapor on estimating ADRE.

2 Methods and data

AERONET is a ground-based remote-sensing global network of Cimel sun photometers (Holben et al., 1998) including the AERONET inversion code with radiative transfer code implementation. The inversion strategy, described in Dubovik and King (2000), provides a group of parameters, e.g., AOD, Ångström exponent (AE) and water vapor column (WVC) from the sun measurements and, for example, SSA, asymmetry parameter (ASYM) and size distribution from the sky measurements. AOD is provided with wavelength channels 340, 380, 440, 500, 670, 870, 1020 and 1640 nm (all or some of these, depending on site of AERONET), WVC from 940 nm and, for example, SSA and ASYM from 440, 670, 870 and 1020 nm. The discrete ordinates method provides broadband fluxes (both at the top of atmosphere and at the surface, with and without aerosols), calculated with the correlated-k distribution in the Global Atmospheric Model (GAME) code from 200 to 4000 nm. The ozone is based on monthly averaged climatology by the Total Ozone Mapping Spectrometer (TOMS). Moreover, the US standard 1976 atmosphere model sets the atmospheric gaseous profile. The surface reflectivity is approximated by the bidirectional reflectance distribution function (BRDF) and observations from the Moderate-Resolution Imaging Spectroradiometer (MODIS). More details about the AERONET description from, for example, García et al. (2012). The uncertainty of AOD is 0.01–0.02 depending on the wavelength (Eck et al., 1999), the uncertainty in SSA approximately 0.03 (Dubovik et al., 2000), and the uncertainty in WVC of 12 % (Holben et al., 1998). We used broadband modeled surface shortwave fluxes from this data set. In this study, level 1.5 sky AERONET data are divided into groups by station, season (December–February, March–May, June–August and September–November) and by solar zenith angle (SZA) (3° steps in the range 0–80°). A data set was included in the analysis if it had at least 20 observations and the data contained AOD 550 nm values above 0.3 and below 0.1. We chose to use level 1.5 data because using level 2.0 would leave out all quality-assured data with AOD 440 nm < 0.4 (including, for example, quality assured SSA and F calculations). The drawback of this choice is that, at these low values of AOD, there are significant uncertainties in the optical properties retrieved. This is especially true for SSA, which is an important parameter. Thus, we applied all other level 2 criteria except for AOD (and SZA) limit, in order to enhance the accuracy of the data set selected. Moreover, we have imposed an additional data flagging criterion, removing those SSA points at the AOD 440 nm < 0.4, which are outside the average SSA ± standard deviation, defined for the AOD 440 nm > 0.4.

ADRE at the surface is the difference between the solar flux with and without aerosols: ADRE $= \Delta F = F^{\mathrm{aer}} - F^0$ (F^{aer} is flux with aerosols).The major challenge obviously is the determination of F^0. The methodology for its estimation employed in this study is illustrated in Fig. 1, in which F^{aer}(+symbols) is plotted as a function of AOD (from now on 550 nm) for the AERONET site in Kanpur station (26° N, 80° E) for the spring months March–May with SZA $= 69° \pm 1.5°$ (F^{aer} values were normalized for the average Earth–Sun distance and cosine correction of F^{aer} was done within SZA ranges to its midpoints). F^0 represents the case AOD $= 0$, but with measurements only at AOD above ca. 0.15, we have to extrapolate down to 0. In Fig. 1 we show two such extrapolations: a linear fit (dashed line) and a nonlinear decay fit (solid line) with the data.

We chose this data subset since it represent a case in which the F^{aer} and AOD data exhibit the natural nonlinear behavior of radiation intensity decay. Thus the resulting intercepts of the two curves at AOD $= 0$ are quite different: 317 Wm^{-2} with linear extrapolation and 349 Wm^{-2} with nonlinear regression, with a difference of 32 Wm^{-2} when estimating ADRE. Also, for each F^{aer} we show the corresponding AERONET F^0 (circles), based on the retrieved WVC and surface albedo, and calculated with a radiative transfer model (e.g., Garcia et al., 2008; Derimian et al., 2008). We use the ADRE obtained by averaging these F^0 (circles) values (bar at $F = 325\ \mathrm{Wm}^{-2}$ on the y axis) as the benchmark against which the extrapolation methods are evaluated.

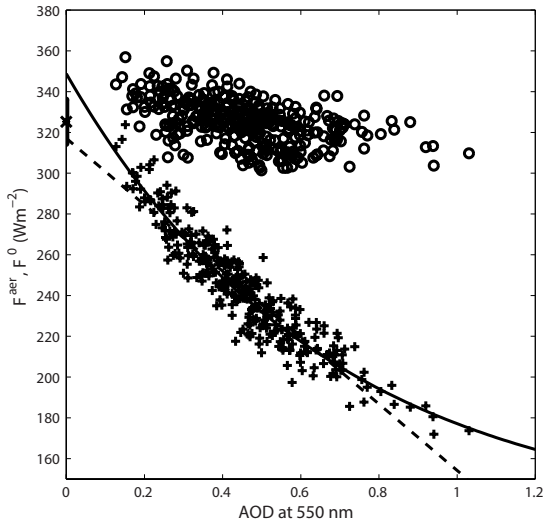

Figure 1. Radiative flux with aerosols F^{aer} (plusses) and without aerosols F^0 (circles) as a function of AOD for the AERONET site in Kanpur in March–May and with SZA = 69° ± 1.5°. The bar on the vertical axis represents the mean value of the estimated F^0 (all circles). The solid and dashed lines represent the exponential and linear fits to the data, respectively.

Mathematically, our analysis can be summed up as a comparison between the extrapolated ADRE

$$\text{ADRE}_{\text{extrapol}} = \frac{1}{n}\sum F_i^{\text{aer}} - F^0_{\text{extrapol}} \quad (1)$$

and the AERONET ADRE

$$\text{ADRE}_{\text{AERONET}} = \frac{1}{n}\sum F_i^{\text{aer}} - \frac{1}{n}\sum F_i^0, \quad (2)$$

where F_i^{aer} and F_i^0 are F^{aer} and F^0, respectively, with i varying from one to the number of data set, n. Notably, the extrapolated F^0 (F^0_{extrapol}) derived with fits represents a single value for a data set, but in the AERONET, F^0 is determined side by side with each F^{aer}. F^0_{extrapol} is calculated using fits as follows:

$$F_i^{\text{nonlin}} = x_1 + x_2 * \exp(-x_3 * \text{AOD}_i); \quad F^{0,\text{nonlin}}_{\text{extrapol}} = x1 + x2, \quad (3)$$

$$F_i^{\text{lin}} = x_1' + x_2' * \text{AOD}_i; \; F^{0,\text{lin}}_{\text{extrapol}} = x_1', \quad (4)$$

where F_i^{nonlin} and F_i^{lin} are estimated F^{aer} derived for each AOD with the nonlinear and linear method, respectively. Constants of fits are x_1, x_2, x_3, x_1' and x_2'. $F_i^{0,\text{nonlin}}$ and $F_i^{0,\text{lin}}$, thus F^0_{extrapol} of the nonlinear and linear fits, are provided with the constants.

Our decision to use the modeled F from AERONET, instead of pyranometer measurements, was based on two different aspects. First, this allowed us to include a multiple number of sites, with very different and varying aerosol conditions. Second, AERONET data provided interesting ancillary measurements to support and better understand our analysis, WVC being the most crucial one. In addition, the AERONET F's agree with pyranometer measurements with a correlation better than 99 %, and the relative difference varies from 0.98 to 1.02 (Garcia et al., 2008). Moreover, we tested the analysis at two sites – Alta Floresta and Goddard Space Flight Center (GSFC) – by using pyranometer measured fluxes F and found no significant difference of the results at these two sites, if compared to the corresponding analysis using the AERONET-modeled fluxes instead (see Supplement Sect. S1).

3 Results

As further examples of determining ADRE using regression analysis, we show F^{aer} and AOD data from four sites in Fig. 2. In addition, the linear (dashed line) and nonlinear decay (solid line) fits to the data are shown. The bar on the vertical axis represents the average (with SD) value for F^0. GSFC (39° N, 77° W) (SZA = 70°) (Fig. 2a) and Rio Branco (10° S, 68° W) (SZA = 70°) (Fig. 2b) represent cases in which the data are of sufficient quality for estimating ADRE: AOD values reach close zero with only minor changes in WVC, aerosol optical properties and surface reflectance for a given AOD, resulting in a narrow spread in the data. In these cases, since the nonlinear decay represents a more realistic decay of radiation intensity (based on squared values of residuals), the intersection of the nonlinear fit with the AOD = 0 axis (y axis) is within the SD of the baseline value. Dhadnah (26° N, 56° E) (SZA = 70°) (Fig. 2c) and GSFC at SZA = 22° (Fig. 2d) are examples of more challenging cases: in Fig. 2c only data points with AOD > 0.2 exist so that a more extensive extrapolation is needed, and in Fig. 2d there is significant scatter in the points.

Perhaps the most interesting feature shown in Fig. 2, which also significantly affects the quality of ADRE estimation, is the correlation of F^0 with AOD. In Fig. 2a–d there is a negative correlation while in Fig. 2b the correlation is positive. The negative correlation between F^0 and AOD is indirectly caused mainly by a positive correlation of AOD with WVC due to humid air masses with large aerosol concentration. Only in some cases, where air masses are dominated by dust aerosols, the correlation is negative. With increasing AOD and WVC, the WVC dims an increasing fraction of the radiation intensity – resulting in a smaller F^0. The opposite occurs if AOD and WVC have a negative correlation. Increase in the AOD as a function of WVC is presumably partly due to hygroscopic growth (e.g., Kitamori et al., 2009), although probably a major part of the correlation can be attributed to

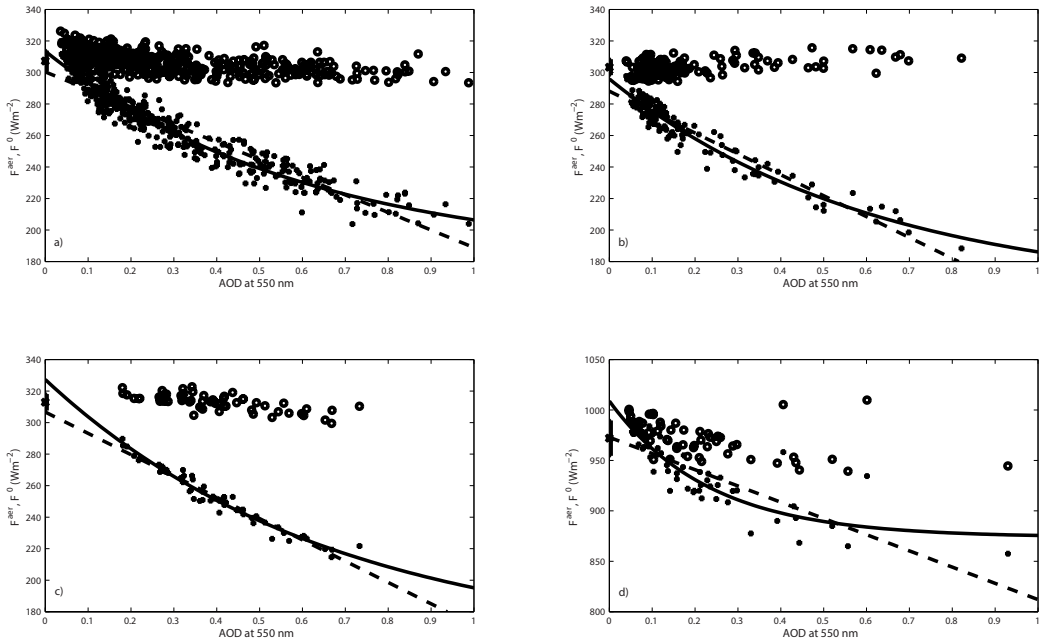

Figure 2. Same as Fig. 1, but for the June–August season in **(a)** GSFC (SZA = 70°), **(b)** Rio Branco (SZA = 70°), **(c)** Dhadnah (SZA = 70°), and **(d)** GSFC (SZA = 22°).

a large variance in atmospheric conditions of aerosol properties and air humidity during seasons.

The intersections of the nonlinear decay fits (solid lines in Fig. 2) with the AOD = 0 axis – 313.5 W m^{-2} (Fig. 2a), 295.9 W m^{-2} (Fig. 2b), 327.4 W m^{-2} (Fig. 2c) and 1008.9 W m^{-2} (Fig. 2d) – approximate the F^0 value at AOD = 0. This is clear from the figure, if one imagines straight line fits through the circles and extrapolates fits down to AOD = 0. This approximation is, however, not necessarily a good one for the mean F^0, if F^0 and AOD correlate (through the AOD–WVC correlation). For the negative correlation cases (Fig. 2a–d), the intersections of the nonlinear decay fits with the AOD = 0 axis tend to therefore overestimate the mean baseline F^0 (307.3 W m^{-2} for Fig. 2a, 312.9 W m^{-2} for Fig. 2c, and 972.1 W m^{-2} for Fig. 2d) – as the majority of F^0 values are below the extrapolated F^0. Typically, for the positive correlation cases (Fig. 2b, mean of $F^0 = 303.4$ W m^{-2}) the opposite occurs. As the linear fit obviously results in a lower estimation of F^0, the linear regression method can result often in a better estimation of the mean F^0, as is clearly the case in Fig. 2c (mean $F^0 = 306.7$ W m^{-2}) and Fig. 2d (mean $F^0 = 973.0$ W m^{-2}) – even if the nonlinear regression is physically more correct.

The performance of the two different regression methods and, in particular, the WVC and AOD correlation effect on the performance is illustrated as scatterplots in Fig. 3. In Fig. 3a all data are presented in ADRE (nonlinear decay method) and ADRE (AERONET $\Delta F^{\text{average}}$, Eq. 2) form. The color of the single points indicates the correlation of the WVC and AOD. In Fig. 3b the same is shown for the linear regression case. Evidently, a majority of the cases are such that WVC and AOD have a strong positive correlation (red colored points). In addition, it seems that, for most of these cases, the linear regression method (Fig. 3b) results in a better ADRE estimation than the nonlinear decay regression method (Fig. 3a). This means that the inaccuracy inherent in the linear regression cancels out errors caused by the WVC and AOD correlation. For a weak WVC and AOD correlation, the nonlinear decay method appears to be clearly better. Other parameters such as surface albedo, ASYM or SSA do not play as crucial of a role as WVC. We classified the ADRE estimates of the both methods against the baseline in respect of AOD, albedo, ASYM, SSA and WVC. It was evident that only WVC can explain the observed differences of both methods when compared against the baseline (see Supplement Sect. S2). Moreover, we confirmed, by modeling a short wavelength range (310–500 nm), that this WVC effect vanishes, if some other wavelength band as for example the visible range of 400–700 nm containing no significant water vapor absorption is under consideration, instead of the broadband wavelength range of F^{aer} (see Supplement Sect. S3).

Next we investigated possible geographical features of this correlation. Figure 4 shows the WVC and AOD correlation (in the color scales) at all the sites available from AERONET,

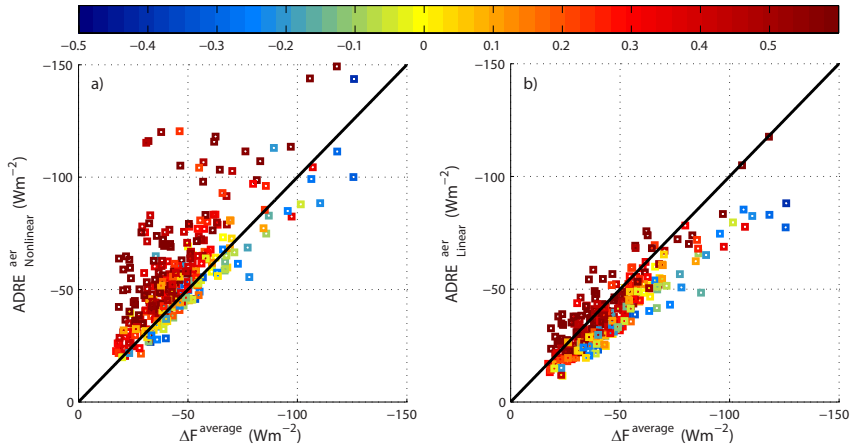

Figure 3. ADRE predicted with exponential decay **(a)** and linear **(b)** regression methods (Eq. 1), compared with AERONET values (Eq. 2). The color of the data points represents the correlation coefficient of the AOD and WVC correlation, with red color indicating positive and blue color negative correlation.

in this case for seasons: December–February (DJF, Fig. 4a), March–May (MAM, Fig. 4b), June–August (JJA, Fig. 4c) and September–November (SON, Fig. 4d) (all years available). Most of the points are colored either green or red, indicating an absent or a positive correlation. The strongest positive correlation is for the stations in Europe and eastern USA, presumably due to aerosol hygroscopic growth. This holds especially for the JJA and SON seasons. The DJF and MAM seasons provide weaker positive correlation, indicating that the linear method can then provide there somewhat underestimated ADRE. Interestingly, the strongest negative correlation appears during the JJA season in the west Saharan region and Central America, probably caused by a strong desert dust domination and low WVC in the Saharan outflow region (Marsham et al., 2008). During those particular cases, the linear method can significantly underestimate ADRE, as indicated by the points of largest negative WVC vs. AOD correlation in Fig. 3b, while the nonlinear decay provides then a better estimate.

Finally, the ADRE estimations of all data are grouped together in numerical form in Table 1. As already evident from the figures, the nonlinear decay regression method overestimates (mean $= -57.2\,\mathrm{Wm}^{-2}$) while the linear method underestimates (mean $= -39.4\,\mathrm{Wm}^{-2}$) the magnitude of ADRE (AERONET value $= -46.1\,\mathrm{Wm}^{-2}$). Overall, the linear method yields better results than the nonlinear decay method.

Previous studies have shown that the AERONET WVC agrees well with radiosonde sounding data (e.g., Prasad and Singh, 2009; Bokoye et al., 2007). Also, Smirnov et al. (2004) indicate that the AERONET WVC provides the root mean square difference of 7.0 % in a multiyear comparison with WVC measurements derived from GPS. We also compared AERONET WVC measurements against radiosonde data from five sites (Alta Floresta, Cuiaba-Miranda, Niamey, Thessaloniki and Wallops) and observed similarly high correlations between these two data sources. However, we wanted to assess in particular whether there exists any systematic dependence between WVC from these two data sources as a function of AOD, which could affect our ADRE analysis based on the modeled F. We found that while the ratio between the AERONET and radiosonde WVC is essentially constant for AODs (at 500 nm) larger than about 0.1, in many sites WVC can deviate for the cases of smallest AOD (below 0.1). We estimated how our ADRE values (based on the F and AOD relation) would change if we normalized the AERONET-modeled fluxes to incorporate the WVC from the radiosonde measurements instead of AERONET-measured WVC. We found that the increased WVC uncertainty at the lowest AOD values introduces an insignificant change in our ADRE estimates.

4 Conclusions

Determining the ADRE at the earth's surface from radiative flux, F, measurements is not straightforward because it involves the estimation of the flux without aerosols F^0. This requires either radiative transfer modeling or an extrapolation of F down to AOD $= 0$.

We have evaluated two such extrapolation methods: (i) a linear fit and (ii) a nonlinear decay fit to the F and AOD data. As a reference we used the AERONET ADRE data in which F^0 (and F) is calculated with radiative transfer modeling. Radiation attenuation due to multiple scattering and absorption results typically in a near-nonlinear decay of the

Table 1. The estimated ADRE (F^{aer}) with standard deviations compared with the AERONET value. MAD – mean absolute deviation. Units are in Wm^{-2}, except for the correlation coefficient (CC).

Parameter	AERONET	Method	Estimate	Est. – AERONET	CC	MAD
ADRE	-46.1 ± 20.4	Exp. decay	-57.2 ± 23.4	-11.1	0.75	13.4
		Linear	-39.4 ± 16.9	$+6.7$	0.89	8.9

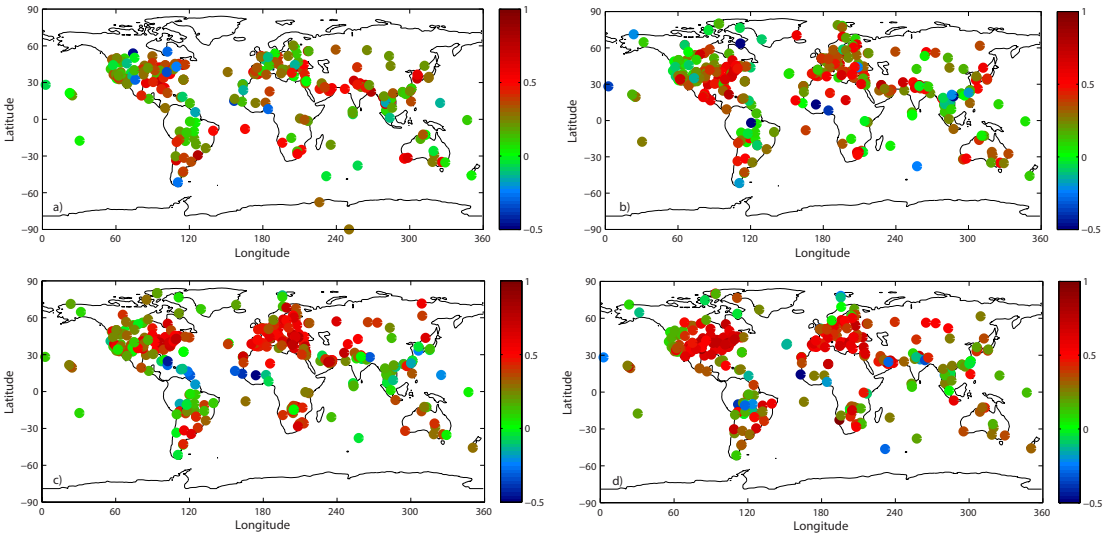

Figure 4. Geographical distribution of the AOD and WVC correlation, at all AERONET stations considered in this study for **(a)** December–February, **(b)** March–May, **(c)** June–August and **(d)** September–November (all available years).

intensity, and thus the nonlinear decay regression is expected to give a better estimation of ADRE. This would be the case if the typically positive correlation of WVC and AOD did not affect the dependency. F^0 represents an unrealistically low WVC, resulting in an underestimation of attenuation caused by the WVC, and hence a too large F^0. This leads to an overestimation of the magnitude of ADRE. For stations and data series in which there is no correlation between WVC and AOD, the nonlinear decay fit is superior.

As the WVC effect was found to be of such importance, we also investigated the geographical correlation of WVC and AOD. The positive correlations clearly dominate, and clear negative correlations occur predominantly in desert-dust-dominated data series, such as the regions at the Saharan outflow. The strongest positive correlation was found in stations in Europe and eastern USA. Our results indicate that the regression method, either linear or nonlinear, can readily produce a significant error due to the correlation of WVC and AOD. Since for a majority of locations AOD and water vapor column (WVC) have a positive correlation, the linear method gives somewhat better results in general than the nonlinear approach, for the reasons discussed above. However, there are specific regions of strong negative WVC and AOD correlation, most notably in the Saharan dust outflow region, where the opposite takes place and nonlinear approach results in better estimate for ADRE. Therefore, based on our results we recommend that when the surface ADRE is estimated by using pyranometer and AOD measurements, the site-specific correlation between WVC and AOD should be also estimated to deduce whether linear or nonlinear approach is more suitable. We moreover recommend taking one step forward and additionally attempting to correct for the possible bias due to WVC and AOD correlation. When the data for the WVC become available, then better ADRE accuracy is likely achieved if the flux measurements are normalized to constant WVC amount with simple scaling obtained from RT modeling.

The Supplement related to this article is available online at doi:10.5194/acp-14-6103-2014-supplement.

Acknowledgements. We thank the AERONET team, principal investigators and other participants for theirs effort in establishing and maintaining the network. This study is supported by the Academy of Finland Doctoral Programme ACCC and the Maj and Tor Nessling Foundation. We also thank Larry Oolman from Department of Atmospheric Science, University of Wyoming, for providing radiosonde data of atmospheric water vapor column abundance.

Edited by: E. Gerasopoulos

References

Bokoye, A. I., Royer, A., Cliche, P., and O'Neill, N.: Calibration of Sun Radiometer – based atmospheric water vapor retrievals using GPS meteorology, J. Atmos. Ocean. Tech., 24, 964–979, doi:10.1175/JTECH2011.1, 2007.

Bush, B. C. and Valero, F. P. J.: Spectral aerosol radiative forcing at the surface during the Indian Ocean Experiment (INDOEX), J. Geophys. Res., 107, 8003, doi:10.1029/2000JD000020, 2002.

Bush, B. C. and Valero, F. P. J.: Surface aerosol radiative forcing at Gosan during the ACE-Asia campaign, J. Geophys. Res., 108, 8660, doi:10.1029/2002JD003233, 2003.

Conant, W. C., Seinfeld, J. H., Wang, J., Carmichael, G. R., Tang, Y., Uno, I., Flatau, P. J., Markowicz, K. M., and Quinn, P. K.: A model for the radiative forcing during ACE-Asia derived from CIRPAS Twin Otter and R/V Ronald H. Brown data and comparison with observations, J. Geophys. Res., 108, 8661, doi:10.1029/2002JD003260, 2003.

Derimian, Y., Léon, J.-F., Dubovik, O., Chiapello, I., Tanré, D., Sinyuk, A., Auriol, F., Podvin, T., Brogniez, G., and Holben, B. N.: Radiative properties of aerosol mixture observed during the dry season 2006 over M'Bour, Senegal (African Monsoon Multidisciplinary Analysis campaign), J. Geophys. Res., 113, D00C09, doi:10.1029/2008JD009904, 2008.

Di Sarra, A., Pace, G., Meloni, D., De Silvestri, L., Piacentino, S., and Monteleone, F.: Surface shortwave radiative forcing of different aerosol types in the central Mediterranean, Geophys. Res. Lett., 35, L02714, doi:10.1029/2007GL032395, 2008.

Dubovik, O. and King, M. D.: A flexible inversion algorithm for retrieval of aerosol optical properties from Sun and sky radiance measurements, J. Geophys. Res., 105, 20673–20696, doi:10.1029/2000JD900282, 2000.

Dubovik, O., Smirnov, A., Holben, B. N., King, M. D., Kaufman, Y. J., Eck, T. F., and Slutsker, I.: Accuracy assessments of aerosol optical properties retrieved from Aerosol Robotic Network (AERONET) Sun and sky radiance measurements, J. Geophys. Res., 105, 9791–9806, doi:10.1029/2000JD900040, 2000.

Dumka, U. C., Satheesh, S. K., Pant, P., Hegde, P., and Krishna Moorthy, K.: Surface changes in solar irradiance due to aerosols over central Himalayas, Geophys. Res. Lett., 33, L20809, doi:10.1029/2006GL027814, 2006.

Eck, T. F., Holben, B. N., Reid, J. S., Dubovik, O., Smirnov, A., O'Neill, N. T., Slutsker, I., and Kinne, S.: Wavelength dependence of the optical depth of biomass burning, urban, and desert dust aerosols, J. Geophys. Res., 104, 31333–31349, doi:10.1029/1999JD900923, 1999.

García, O. E., Díaz, A. M., Expósito, F. J., Díaz, J. P., Dubovik, O., Dubuisson, P., Roger, J.-C., Eck, T. F., Sinuyk, A., Derimian, Y., Dutton, E. G., Schafer, J. S., Holben, B. N., and García, C. A.: Validation of AERONET estimates of atmospheric solar surface fluxes and aerosol radiative forcing by ground-based broadband measurements, J. Geophys. Res., 113, D21207, doi:10.1029/2008JD010211, 2008.

García, O. E., Díaz, A. M., Expósito, F. J., Díaz, J. P., Redondas, A., and Sasaki, T.: Aerosol radiative forcing and forcing efficiency in the UVB for regions affected by Saharan and Asian Mineral Dust, J. Atmos. Sci., 66, 1033–1040, doi:10.1175/2008JAS2816.1, 2009.

García, O. E., Díaz, J. P., Expósito, F. J., Díaz, A. M., Dubovik, O., and Derimian, Y.: Aerosol Radiative Forcing: AERONET-Based Estimates, Climate Models, Dr. Leonard Druyan (Ed.), ISBN: 978-953-51-0135-2, InTech, available at: http://www.intechopen.com/books/climate-models/aerosol-radiative-forcing-aeronet-based-estimates, 275–296, 2012.

Holben, B. N., Eck, T. F., Slutsker, I., Tanré, D., Buis, J. P., Setzer, A., Vermote, E., Reagan, J. A., Kaufman, Y. J., Nakajima, T., Lavenu, F., Jankowiak, I., and Smirnov, A.: AERONET – a Federated Instrument Network and Data Archive for aerosol characterization, Remote Sens. Environ., 66, 1–16, doi:10.1016/S0034-4257(98)00031-5, 1998.

IPCC: Climate Change 2013: The Physical Science Basis. Contribution of Working Group I to the Fifth Assessment Report of the Intergovernmental Panel on Climate Change, edited by: Stocker, T. F., Qin, D., Plattner, G.-K., Tignor, M., Allen, S. K., Boschung, J., Nauels, A., Xia, Y., Bex, V., and Midgley, P. M., Cambridge University Press, Cambridge, United Kingdom and New York, NY, USA, 1535 pp., 2013.

Kaufman, Y. J., Tanré, D., Holben, B. N., Mattoo, S., Remer, L. A., Eck, T. F., Vaughan, J., and Chatenet, B.: Aerosol radiative impact on spectral solar flux at the surface, derived from principal-plane sky measurements, J. Atmos. Sci., 59, 635–646, doi:10.1175/1520-0469(2002)059<0635:ARIOSS>2.0.CO;2, 2002.

Kitamori, Y., Mochida, M., and Kawamura, K.: Assessment of the aerosol water content in urban atmospheric particles by the hygroscopic growth measurements in Sapporo, Japan, Atmos. Environ., 43, 3416–3423, 2009.

Kudo, R., Uchiyama, A., Yamazaki, A., Sakami, T., and Kobayashi, E.: From solar radiation measurements to optical properties: 1998–2008 trends in Japan, Geophys. Res. Lett., 37, L04805, doi:10.1029/2009GL041794, 2010.

Loeb, N. G. and Su, W.: Direct aerosol radiative forcing uncertainty based on a radiative perturbation analysis, J. Climate, 23, 5288–5293, doi:10.1175/2010JCLI3543.1, 2010.

Markowicz, K. M., Flatau, P. J., Remiszewska, J., Witek, M., Reid, E. A., Reid, J. S., Bucholtz, A., and Holden, B.: Observations and modeling of the surface aerosol radiative forcing during UAE2, J. Atmos. Sci., 65, 2877–2891, doi:10.1175/2007JAS2555.1, 2008.

Marsham, J. H., Parker, D. J., Grams, C. M., Johnson, B. T., Grey, W. M. F., and Ross, A. N.: Observations of mesoscale and boundary-layer scale circulations affecting dust transport and uplift over the Sahara, Atmos. Chem. Phys., 8, 6979–6993, doi:10.5194/acp-8-6979-2008, 2008.

Myhre, G.: Consistency between satellite-derived and modeled estimates of the direct aerosol effect, Science, 325, 187–190, doi:10.1126/science.1174461, 2009.

Prasad, A. K. and Singh, R. P.: Validation of MODIS Terra, AIRS, NCEP/DOE AMIP-II Reanalysis-2, and AERONET Sun photometer derived integrated precipitable water vapor using ground-based GPS receivers over India, J. Geophys. Res., 114, D05107, doi:10.1029/2008JD011230, 2009.

Roger, J. C., Mallet, M., Dubuisson, P., Cachier, H., Vermote, E., Dubovik, O., and Despiau, S.: A synergetic approach for estimating the local direct aerosol forcing: application to an urban zone during the Expriénce sur Site pour Contraindre les Modèles de Pollution et de Transport d'Emission (ESCOMPTE) experiment, J. Geophys. Res., 111, D13208, doi:10.1029/2005JD006361, 2006.

Satheesh, S. K. and Ramanathan, V.: Large differences in tropical aerosol forcing at the top of the atmosphere and Earths surface, Nature, 405, 60–63, doi:10.1038/35011039, 2000.

Satheesh, S. K., Vinoj, V., and Krishna Moorthy, K.: Radiative effects of aerosols at an urban location in southern India: Observations vs. model, Atmos. Environ., 44, 5295–5304, doi:10.1016/j.atmosenv.2010.07.020, 2010.

Smirnov, A., Holben, B. N., Lyapustin, A., Slutsker, I., and Eck, T. F.: AERONET processing algorithm refinement, paper presented at AERONET Workshop, Univ. of Huelva and the Span. Soc. of Optics, El Arenosillo, Spain, 10–14 May, 2004.

Atmos. Chem. Phys., 16, 8181–8191, 2016
www.atmos-chem-phys.net/16/8181/2016/
doi:10.5194/acp-16-8181-2016

Atmospheric Chemistry and Physics
Open Access
EGU

Retrieval of aerosol optical depth from surface solar radiation measurements using machine learning algorithms, non-linear regression and a radiative transfer-based look-up table

Jani Huttunen[1,2], Harri Kokkola[1], Tero Mielonen[1], Mika Esa Juhani Mononen[3], Antti Lipponen[1,2], Juha Reunanen[4], Anders Vilhelm Lindfors[1], Santtu Mikkonen[2], Kari Erkki Juhani Lehtinen[1,2], Natalia Kouremeti[5,6], Alkiviadis Bais[6], Harri Niska[7], and Antti Arola[1]

[1]Finnish Meteorological Institute (FMI), Atmospheric Research Centre of Eastern Finland, Kuopio, Finland
[2]Department of Applied Physics, University of Eastern Finland, Kuopio, Finland
[3]Independent researcher, Kuopio, Finland
[4]Tomaattinen Oy, Helsinki, Finland
[5]Physikalisch-Meteorologisches Observatorium Davos, Dorfstrasse 33, 7260 Davos Dorf, Switzerland
[6]Aristotle University of Thessaloniki, Laboratory of Atmospheric Physics, Thessaloniki, 54124, Greece
[7]Department of Environmental and Biological Sciences, University of Eastern Finland, Kuopio, Finland

Correspondence to: Antti Arola (antti.arola@fmi.fi)

Received: 20 January 2016 – Published in Atmos. Chem. Phys. Discuss.: 25 January 2016
Revised: 9 June 2016 – Accepted: 14 June 2016 – Published: 7 July 2016

Abstract. In order to have a good estimate of the current forcing by anthropogenic aerosols, knowledge on past aerosol levels is needed. Aerosol optical depth (AOD) is a good measure for aerosol loading. However, dedicated measurements of AOD are only available from the 1990s onward. One option to lengthen the AOD time series beyond the 1990s is to retrieve AOD from surface solar radiation (SSR) measurements taken with pyranometers. In this work, we have evaluated several inversion methods designed for this task. We compared a look-up table method based on radiative transfer modelling, a non-linear regression method and four machine learning methods (Gaussian process, neural network, random forest and support vector machine) with AOD observations carried out with a sun photometer at an Aerosol Robotic Network (AERONET) site in Thessaloniki, Greece. Our results show that most of the machine learning methods produce AOD estimates comparable to the look-up table and non-linear regression methods. All of the applied methods produced AOD values that corresponded well to the AERONET observations with the lowest correlation coefficient value being 0.87 for the random forest method. While many of the methods tended to slightly overestimate low AODs and underestimate high AODs, neural network and support vector machine showed overall better correspondence for the whole AOD range. The differences in producing both ends of the AOD range seem to be caused by differences in the aerosol composition. High AODs were in most cases those with high water vapour content which might affect the aerosol single scattering albedo (SSA) through uptake of water into aerosols. Our study indicates that machine learning methods benefit from the fact that they do not constrain the aerosol SSA in the retrieval, whereas the LUT method assumes a constant value for it. This would also mean that machine learning methods could have potential in reproducing AOD from SSR even though SSA would have changed during the observation period.

1 Introduction

The Fifth Assessment Report of the Intergovernmental Panel on Climate Change states that the most significant source of uncertainty in the projections of climate is related to aerosols (IPCC, 2013). One significant contribution to this uncertainty comes from the fact that without the knowledge of the aerosol burden in the past, we are not able to estimate

the current forcing of anthropogenic aerosol. For example, the effect of changes in the current aerosol emissions on climate depends on the background aerosol load during the pre-industrial era (e.g. Andreae and Rosenfeld, 2008; Carslaw et al., 2013). In addition, the current estimates of past aerosol emissions are highly uncertain (Granier et al., 2011), thus increased knowledge on historical aerosol levels would increase our ability to estimate the present day aerosol radiative forcing.

One limiting factor in determining the properties of global aerosol in the past has been that observations of aerosol radiative effects have been limited to fairly recent periods. For example, the aerosol optical depth has mainly been measured using sun photometers and the most widely known ground-based network of sun photometers is Aerosol Robotic Network (AERONET; Holben et al., 1998). Although, AERONET already contains over 700 stations globally, with a fairly good spatial coverage compared to many other observation networks, it still lacks in temporal coverage, having provided aerosol optical properties and AOD only since 1990s and reaching the current status in recent years. The earliest records of satellite-based AOD are provided by TOMS (total ozone mapping spectrometer, e.g. Torres et al., 2002) and AVHRR (Advanced Very High Resolution Radiometer, Geogdzhayev et al., 2005) from 1979 and 1983 onwards respectively. However, neither one of these instruments were specifically designed to retrieve aerosol properties. The more recent dedicated aerosol sounders, such as ATSR (The Along Track Scanning Radiometer 2, Llewellyn-Jones and Remedios, 2012), MODIS (Moderate Resolution Imaging Spectroradiometer, Levy et al., 2010), VIISR (Visible Infrared Imaging Radiometer Suite, Jackson et al., 2013) and MISR (Multi-angle Imaging SpectroRadiometer, Kahn and Gaitley, 2015) offer data from 1995, 2000 and 2002 onwards respectively. It is therefore apparent that neither sun photometer nor satellite records of AOD are available for all the decades where industrialization has had a significant effect on the aerosol load.

There have been, however, recent studies where aerosol load has been indirectly retrieved from global surface solar radiation (SSR) or separately from direct and diffuse radiation measurements, which cover much longer time periods than sun photometer and satellite observations of AOD. Recently, Kudo et al. (2011) and Lindfors et al. (2013) used radiation measurements taken with pyranometers and pyrheliometers to estimate AOD. Lindfors et al. (2013) demonstrated that AOD can be estimated by using SSR and water vapour information and a look-up table (LUT) generated with a radiative transfer code. Their method produces AOD estimates that have 2/3 of the results within ± 20 or ± 0.05 % of collocated AERONET AODs. Because pyranometer SSR measurements have been since 1950s over the globe, the usage of AOD estimates based on SSR measurements would enable us to construct AOD time series that go several decades back in time.

Since the 1990s machine learning methods have made their way to atmospheric sciences and have been used e.g. in satellite data processing, climate modelling and weather prediction (Hsieh, 2009). Because of their ability to retrieve parameters from data that have strongly non-linear relationships, they have the potential to retrieve AOD from a combination of solar radiation measurements and auxiliary data such as water vapour content (WVC) and solar zenith angle (SZA), similarly to what was done by Lindfors et al. (2013) using a radiative transfer-based approach. The aim of the present work is to investigate how well machine learning methods are able to estimate AOD from pyranometer observations by evaluating their performance in comparison with a radiative transfer-based look-up-table approach. We chose four different methods: neural network (NN, McCulloch and Pitts, 1943), random forest (RF, Breiman, 2001), Gaussian process (GP, Santner et al., 2013) and support vector machine (SVM, Smola and Schölkopf, 2004) and compared them against a look-up table and a non-linear regression method (NR, Bates and Watts, 1988). The performance of these methods was evaluated with AERONET AOD observations in Thessaloniki, Greece, after the AOD estimates were derived with SSR observations. Non-linear regression has been successfully used in multiple studies within aerosol and atmospheric sciences (e.g. Huttunen et al., 2014; Ahmad et al., 2013). Of these machine learning methods, neural networks (NNs) have been actively used in different types of applications in atmospheric sciences. For example, it has been applied to retrieve aerosol properties from remote sensing instruments (Olcese et al., 2015; Taylor et al., 2014). Moreover, Foyo-Moreno et al. (2014) uses NNs to indicate that a ratio between solar diffuse radiation and normal direct irradiance is the most adequate parameter for estimating AOD from solar radiation measurements. There have been, however, recent studies where aerosol load has been indirectly retrieved from global surface solar radiation (SSR) or separately from direct and diffuse radiation measurements, which cover much longer time periods than sun photometer and satellite observations of AOD. Recently, Kudo et al. (2011) and Lindfors et al. (2013) used radiation measurements taken with pyranometers and pyrheliometers to estimate AOD. The study by Olcese et al. (2015) is similar to ours in the sense that they use alternative data together with neural network approach in an attempt to retrieve AOD at an AERONET site. In their study, they fill in missing AOD values (e.g. due to cloud cover) at one AERONET station based on trajectories and AOD observed on another site. To our knowledge, the rest of the analysed methods have not been used to retrieve aerosol properties directly from observations.

2 Data and methods

We compared the ability of several methods to estimate AOD, based on SSR and water vapour measurements (and

SZA that can be readily determined for any given time and location) against AERONET AOD measurements at 500 nm (henceforth AOD) taken at Thessalonki, Greece. This site was chosen for this study, because it has all the necessary high quality measurements from a 10-year time period, because it is the same site to which Lindfors et al. (2013) applied their LUT approach. Furthermore, the location has varying aerosol concentrations and relatively high AOD values throughout the year.

2.1 Pyranometer measurements of surface solar radiation

SSR has been measured at Thessaloniki since January 1993 with a CM21 pyranometer manufactured by Kipp and Zonen. The instrument is located on the roof of the Physics Department at the Aristotle University of Thessaloniki (40.63° N, 22.96° E), ca. 60 m above sea level. The data are sampled every 1–2 s and every minute the average and standard deviation of the samples are recorded (see more details from Lindfors et al., 2013). The calibration of the pyranometer has been confirmed to stay within the quoted manufacturer accuracy (Bais et al., 2013).

2.2 AERONET measurements

AERONET is a network of sun and sky scanning radiometers that measure direct sun and sky radiance at several wavelengths, typically centred at 340, 380, 440, 500, 670, 870, 940 and 1020 nm, providing measurements of various aerosol-related properties (Holben et al., 1998). From direct sun measurements we exploited AOD and WVC data. When sky radiance measurements are also included, more detailed aerosol properties such as single scattering albedo (SSA) and asymmetry parameter (gg) can be retrieved (Dubovik et al., 2000). In the evaluation of the machine learning methods we used Level 2.0 (cloud-screened and quality assured) AERONET direct sun measurements of AOD and WVC for Thessaloniki. The Cimel sun photometer is located on the roof of the Physics Department in the close vicinity of the pyranometer discussed above. From the inversion products, to interpret some of our results in more detail, we used level 1.5 (cloud-screened) retrievals. However, when we selected the data from the Level 1.5 inversion product, we applied all the other level 2.0 AERONET criteria except for the AOD threshold. In other words, we applied the same rigorous quality control that is required for Level 2 data, but we only relaxed the requirement for AOD at 440 nm to range from 0.4 to 0.1, in order to have more reliable measurements for our data analysis.

2.3 Cloud-screening of the pyranometer measurements and collocation with the AERONET measurements

Cloud screening is a crucial factor in the analysis, thus only contribution of aerosols are considered, not clouds. The SSR data were at first cloud screened in order to ensure that only clear-sky measurements were included in the analysis (see Lindfors et al., 2013, for more details). However, during the analysis of the data it became evident that even after the initial cloud screening, the SSR data still included observations that deviated significantly from the main body of the observations. Since there is a high probability that these outliers in the data were caused e.g. by cloud contamination, we applied additional screening to the data. Thus, we removed the clear outliers of possibly undetected clouds, in our case those observations that deviated by more than $\pm 20\,\mathrm{W\,m^{-2}}$ from the exponential regression fit ($\mathrm{SSR} = a \times \exp(-b \times \mathrm{AOD}) + c$, where a, b and c are regression constants). This additional screening was applied through regression of SSR against AOD for a given range of SZA (within $\pm 0.5°$). It has to be noted that these data were only a small fraction of all the data that remained after the cloud screening and it is very unlikely that the additional cloud screening would affect the main results and the conclusions of our study.

The SSR values were collocated for each AOD with the ± 1 min difference, averaged and finally normalized for the Sun–Earth distance corresponding to 1 January. The training data set for the machine learning methods contained the years 2009–2014 and the validation (verification) data set years 2005–2008. These periods were selected because we wanted to verify whether the methods could provide reasonable AOD estimates for a period other than the training period. The training data set covered approximately 2/3 and the validation data set 1/3 of the whole data. For all methods the input parameters are SSR, WVC and SZA and they produce AOD estimates. Table A1 in Appendix A summarizes the statistics of maximum, minimum, average, SD and median for the input and the output parameters. Table A1 shows that AOD is larger for the validation data set, although the maximum value is larger for the training.

2.4 LUT and NR methods for AOD retrievals

2.4.1 Radiative transfer model based look-up table (LUT)

To retrieve AOD from SSR observations Lindfors et al. (2013) produced a LUT based on radiative transfer simulations. They simulated SSR in different atmospheric conditions by varying AOD, WVC and SZA systematically. They used a single aerosol model for all the simulations, and therefore called their AOD estimate as an effective AOD, which is only a function of SSR, SZA and WVC. Other parameters were assumed as constants, e.g. Ångström Exponent of 1.1, SSA at 500 nm of 0.92 (the SSA's spectral pattern follows the rural background aerosol model by Shettle (1989), where SSA changes from roughly 0.92 at 400 nm to 0.89 at 1000 nm). The asymmetry parameter was assumed wavelength independent with a value of 0.68, while the albedo

Table 1. Statistical characteristics of observed (AERONET) and predicted AOD by the methods of NR (non-linear regression), LUT (look-up table), NN (neural network), RF (random forest), GP (Gaussian process), SVM (support vector machine) and some of their combinations (averages without weights, e.g. NN, SVM combination is their average result). Correlation coefficient (R^2), mean absolute deviation (MAD), median and their ±20 % percentiles between the observed and predicted. Time consumptions with a recent average computer power of the methods for training/estimation in the magnitude of seconds, minutes and hours. The number of observations is 10 684.

Method	Average(SD)	R^2	MAD	Median	Fraction in ±20 %	Time consumption
AERONET	0.240(0.147)			0.207		
NR	0.228(0.123)	0.880	0.053	0.210	48.4 %	seconds/< second
LUT	0.254(0.136)	0.920	0.046	0.236	52.6 %	hours/minutes
NN	0.251(0.156)	0.920	0.044	0.212	59.1 %	hours/< second
RF	0.225(0.116)	0.870	0.052	0.204	52.9 %	tens of seconds/< second
GP	0.240(0.130)	0.927	0.041	0.213	60.8 %	minutes/tens of seconds
SVM	0.242(0.150)	0.918	0.044	0.201	58.4 %	tens of seconds/< second
NN, SVM	0.247(0.152)	0.924	0.043	0.207	59.7 %	
NN, SVM, RF	0.240(0.138)	0.922	0.042	0.205	59.9 %	
SVM, RF	0.234(0.131)	0.913	0.044	0.202	58.0 %	
NN, RF	0.238(0.134)	0.916	0.043	0.207	59.0 %	

was varying with wavelength and SZA. For a more detailed description of the LUT method see Lindfors et al. (2013).

2.4.2 Non-linear regression method (NR)

The non-linear regression (NR) is a multivariate analysis method which is used when the dependencies between the study variables are not linear (Bates and Watts, 1988). NR is useful especially when there are physical reasons for believing that the relationship between the response and the predictors follows a particular functional form. Benefits of NR are that it needs only moderate-sized samples of the studied phenomena to give adequately precise results and as an output it gives a simple but not predefined function for prediction. An additional advantage of NR against the other methods presented in this paper is that once the parameters are estimated, they can be used in similar cases without additional training data. In this study we assume that AOD can be estimated as a function of SSR, WVC and SZA. Multiple different formulations for the NR function were tested and the function with the best prediction ability found for this data is given by

$$\begin{aligned}\mathrm{AOD} = {} & b_0 + b_1 \exp\left(\frac{1}{\mathrm{SZA}}\right) + b_2 \exp\left(\frac{1}{\mathrm{SSR}}\right) \\ & + b_3 \exp\left(\frac{1}{\mathrm{WVC}}\right) + b_4 \exp\left(\frac{1}{\mathrm{SZA}} + \frac{1}{\mathrm{SSR}}\right) \\ & + b_5 \exp\left(\frac{1}{\mathrm{SZA}} + \frac{1}{\mathrm{WVC}}\right) \\ & + b_6 \exp\left(\frac{1}{\mathrm{SSR}} + \frac{1}{\mathrm{WVC}}\right). \end{aligned} \quad (1)$$

The coefficients b_0–b_6 were determined using R-software (R Core Team, 2014) and are shown in Table A2.

2.5 Machine learning methods for AOD retrievals

2.5.1 Neural network (NN)

Artificial neural networks belong to the family of machine learning methods (McCulloch and Pitts, 1943). As usual in machine learning methods, the aim of an artificial NN is to generate a mathematical model to represent the phenomenon that is examined. The mathematical model of NN structure specifically consists of interconnected neurons with numeric weights. A typical NN model is multilayer perceptron (MLP) (Rosenblatt, 1958), which is used in this study. A MLP network consists of several neuron layers: an input layer, hidden layers and an output layer. The weights and other parameters of the model are tuned or trained with a specific training data set containing input–output pairs of the phenomenon. In this case the model inputs are SSR, WVC and SZA, and the output is AOD. The training is executed with a training algorithm and in this paper the Levenberg–Marquardt algorithm is used (Hagan and Menhaj, 1994). A total of 20 NNs were trained in this case. The NNs differed from each other by the number of neurons in a hidden layer. Five networks with the smallest prediction error within the training data set were selected to the final committee of networks. The final prediction of the NN model was computed as a median of the outputs of all networks in the committee. For more information on NNs see, for example, Bishop (1995).

2.5.2 Random forest (RF)

Random forest is a machine learning technique that may be used for classification and non-linear regression (Breiman, 2001). RF for non-linear regression consists of an ensemble of binary regression trees. Each of these trees is constructed using a randomized training scheme and is essentially a piecewise constant fit to the training data set. The

prediction of a RF model is obtained by averaging the regression tree predictions over the whole model ensemble. In this study, the RF implementation from the Scikit–Learn machine learning library (Pedregosa et al., 2011) was used. We used (SSR, WVC, SZA, SSRxWVC, SSWxSZA, WVCxSZA) as the RF model inputs and AOD as the output. A randomized cross-validation scheme was used to find the optimal training parameters for the RF. For more information on RFs see, for example, Friedman et al. (2001).

2.5.3 Support vector machine (SVM)

Support vector machine (SVM) is a machine learning technique (Vapnik, 1995; Burges, 1998). In this study, we use the standard SVM regression (SVR), the formulation based on the commonly used ε-SVR with radial basis kernel function. For implementing the SVM the libsvm package was used (Chang and Lin, 2011). The objective of ε-SVR is to find a function that has at most ε deviation from the training data set outputs. The training of an ε-SVR model is formulated as a quadratic (convex) optimization problem in which the Vapnik's ε-insensitive loss function is minimized (e.g. Vapnik, 1995). The ε-SVR model has two training parameters that were used to control the training: the regularization parameter, which controls the smoothness of the approximation function (sensitivity to noise) and the parameter ε, which dominates the number of support vectors by governing the accuracy of the approximation function. The determination of SVM control parameters was solved by the means of a grid search. For a more detailed description of the method, the reader is referred to Smola and Schölkopf (2004).

2.5.4 Gaussian process (GP)

Gaussian process (GP) for machine learning is a generic supervised learning method that may be used, for example, for non-linear regression. In GP learning, the function inputs and outputs are treated as Gaussian random variables and the correlations between these variables are modelled. The predictions given by a GP model are computed as conditional probability distributions given the training data and function inputs. As the prediction given by a GP model is a probability distribution, the error estimates for the predicted point estimates are obtained automatically. In this study, the GP implementation from the Scikit–Learn machine learning library was used. The same inputs and output variables as with the RF models were used in the GP training. The best performing correlation function training parameters were sought for using maximum likelihood estimation. A total of 25 GP models were trained. The training of each model was carried out using 2500 training data samples that were randomly sampled from the full training data set. The five best performing GP models were selected into the final GP model committee. The final prediction was computed as the median of the predictions given by the GP models in the committee. For more information on GPs for machine learning see, for example, Welch et al. (1992), Rasmussen and Williams (2006), and Santner et al. (2013).

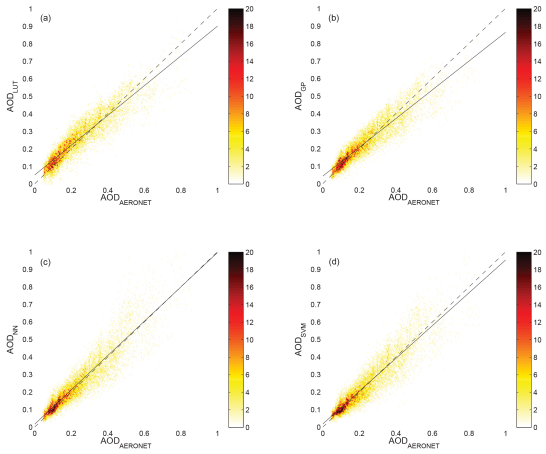

Figure 1. Observed (AERONET) and predicted AOD using the methods of **(a)** LUT (look-up table), **(b)** GP (Gaussian process), **(c)** NN (neural network) and **(d)** SVM (support vector machine). The colourbar indicates the absolute number of results in the areas with the interval of 0.01×0.01. The 1 : 1 lines and linear fits included. The number of observations is 10 684. The relation for the linear fits is estimated $\mathrm{AOD} = a1 + a2 \times \mathrm{AERONET}$ AOD, and the coefficients of the least square fits with their errors are ($a1$, $a2$): 0.050($\pm$0.001), 0.849($\pm$0.004); 0.043($\pm$0.001), 0.820($\pm$0.003); 0.016($\pm$0.001), 0.979($\pm$0.004) and 0.018($\pm$0.001), 0.936($\pm$0.004), for LUT, GP, NN and SVM respectively.

3 Results

3.1 Comparison of the methods

Table 1 shows the statistics of the AOD observed by AERONET together with the statistical characteristics of the predicted AOD for the years 2005–2008. From the table, we can see that predicted values show good correlation against the observations for all the methods. Predictions by RF had the lowest correlation coefficient with a value of 0.87 while the correlation coefficient for NR was only slightly larger, 0.88. For the best performing methods, LUT, GP, NN and SVM, the correlation coefficients were approximately 0.92. Their predicted AODs in comparison to AERONET AOD are shown in Fig. 1. To visualize the distribution of the data, the colourbar in Fig. 1 represents the number of observations for each AOD interval of 0.005. Based on the different statistics in Table 1, machine learning methods (NN, SVM, GP) produce a good match with AERONET data and they perform equally well or better than the LUT method according to all the metrics. Due to the fact that RF and NR are not able to

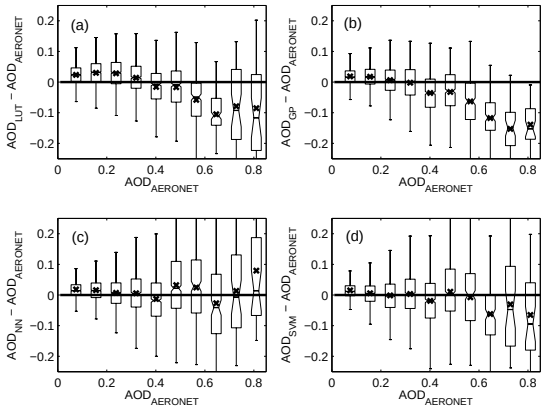

Figure 2. Differences between predicted and observed (AERONET) AOD for the methods: **(a)** LUT (look-up table), **(b)** GP (Gaussian process), **(c)** NN (neural network) and **(d)** SVM (support vector machine) with respect to the observed AOD. The crosses indicate the means of each subgroup, the limits of the boxes are 25, 50 and 75 % of the data, and the lines are plotted with 1.5 times the interquartile ranges.

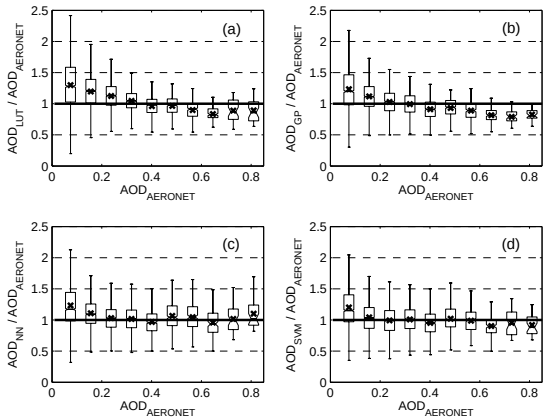

Figure 3. The same as Fig. 2, but the vertical axis indicates the ratio of the predicted to the observed (AERONET) AOD.

produce as good estimates as the LUT method, they were left out from the more detailed analysis.

Although these methods are able to predict the average AOD with a good accuracy, they differ when we compare their ability to predict different AOD levels. In Fig. 1, the colourbar indicates the absolute number of results in the areas with the interval of 0.01×0.01 (vertically and horizontally) for AOD; in addition 1 : 1 lines and linear fits are included. Based on the linear fits, NN appears to have the best agreement with AERONET data for the whole AOD range. As the average and median values of AERONET AOD are 0.240 and 0.207 respectively (Table 1), the main population of the measurements is in the range of moderate AODs. The machine learning methods are obviously weighted to perform best in this range of AODs. However, from Fig. 2, which shows the absolute difference between AERONET and predicted AOD, we can see that LUT and GP tend to significantly underestimate AOD for AODs larger than 0.5, while NN and SVM are able to reach smaller differences with AERONET on average, although with larger overall variabilities than LUT and GP. Although NN and SVM also start to deviate from the observations at higher AODs, these deviations are more modest in a relative sense as can be seen from Fig. 3, which shows the relative difference between the observations and predictions. All the methods overestimate AOD in relative terms when AOD approaches zero (Fig. 3). However, as Fig. 2 demonstrates, the absolute error is systematically very low in the small AOD region (AOD < 0.2). NN and SVM are generalized better for large AODs than the other methods, where the amount of data are small.

In Table 1, the four last rows represent the values for cases where the results of machine learning methods are combined by averaging them. As can be seen from the table, these combinations do not improve the estimates compared to the statistical values of individual methods.

3.2 The effect of water vapour on AOD predictions

Huttunen et al. (2014) showed that WVC and AOD typically have a positive correlation. Therefore, we investigated how the AOD estimates from different methods are affected by WVC. Figure 4 shows the relative difference between the predictions and measured AOD with respect to WVC. From this figure, we can see that the LUT-based AODs are overestimated at the smallest and underestimated at the largest WVC contents. The reason for this behaviour is that the LUT method has been set to assume prescribed and constant properties for many relevant parameters that affect SSR (other than AOD and WVC); e.g. aerosol single scattering albedo, asymmetry parameter and surface albedo (Lindfors et al., 2013). Consequently, the assumption of constant SSA in particular leads to WVC-dependent systematic bias of the LUT-based AOD, as we will show next. The other methods are closer to the ratio of 1 without such a systematic bias, excluding the SVM underestimation for the smallest WVC.

Figure 5 shows measured SSR and LUT-based SSR for a narrow set of SZAs (48.50–51.50°). AOD is on the horizontal axis, SSR on the vertical axis and WVC is shown with the colourbar. From Fig. 5a it is evident that LUT incorporates a strong WVC-dependent structure: for a given SSR level, AOD decreases with increasing water vapour content. This pattern follows from the assumption that the aerosol composition remains the same, i.e. it has a fixed SSA value. Thus in the LUT method, increases in SSR absorption by water vapour are compensated by decreases in aerosol extinction.

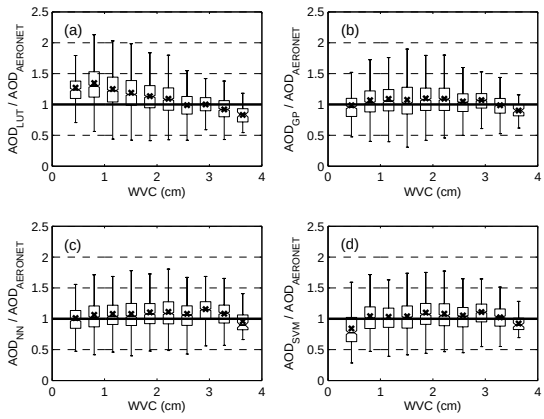

Figure 4. The same as Fig. 3, but the ratio of predicted to measured AOD is given as a function of the water vapour content (WVC).

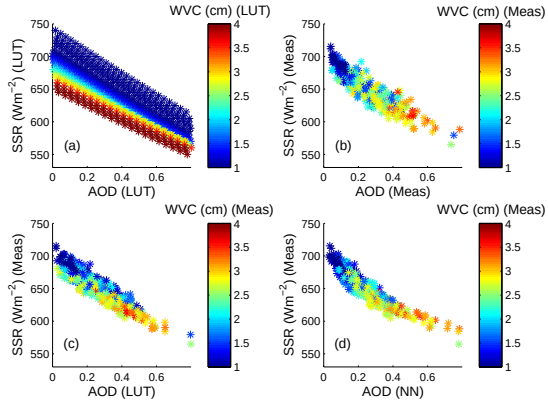

Figure 5. Solar surface radiation (SSR), aerosol optical depth (AOD) and water vapour content (WVC) for a fixed solar zenith angle (48.50–51.50°) for **(a)** look-up table (LUT) and **(b)** measurements (Meas). The predicted AODs for **(c)** LUT and **(d)** neural network (NN) are the same for SSR, WVC and SZA.

In the real atmosphere, water vapour content also has implications on aerosol composition and size. If all conditions apart from water vapour remained constant, increase of water vapour would also increase the uptake of water into aerosol particles thus affecting the aerosol SSA. The effect of fixed SSA is also visible in the way the LUT-based AOD estimates are distributed (Fig. 5a). In Figure 5c we can see that for a given AOD in the LUT, the highest WVC values always correspond to the lowest SSR values. However, the same pattern is not clearly visible either in the plot with the measured values (Fig. 5b) or in the plot with AOD from NN (Fig. 5d). This indicates that although the machine learning methods do not explicitly get any information about the possible systematic covariability of WVC and SSA, they seem to be able to detect it indirectly, at least to some extent.

To further illustrate this, Fig. 6a shows the AERONET measurements of AOD and single scattering co-albedo, 1-SSA at 500 nm as a function of WVC. Here, together with the absorption strength by the water vapour, we considered more illustrative to show the single scattering co-albedo rather than SSA. In this plot, SZA, SSR and season were limited respectively to $58° < \mathrm{SZA} < 62°$, $420\,\mathrm{W\,m^{-2}} < \mathrm{SSR} < 460\,\mathrm{W\,m^{-2}}$, June–August, allowing enough data with the limited parameters. Thus, the plot illustrates the co-variability of WVC and SSA for a limited range of surface solar radiation and SZA, for conditions when the LUT method produces lower AOD values for higher WVC (Fig. 5a). However, Fig. 6a clearly shows that an opposite relationship between AOD and WVC is obtained by the measurements. Moreover, this pattern is compensated by aerosol absorption (remember that in this subset we constrained SSR), which decreases with increasing WVC; this is likely related to the aerosol swelling by hygroscopic growth that increases the scattering of the aerosol. Therefore, we can conclude from the measurements that because of the covariability of WVC and SSA in Thessaloniki, the assumption of a fixed SSA in the LUT causes limitations for predicting AOD, while the machine learning methods can take into account, at least to some extent, this relationship indirectly. Using radiative transfer modelling we demonstrated the magnitude of these changes in water vapour and aerosol absorption, as indicated in Fig. 6. Indeed, they induced opposite effects of similar magnitude in surface solar irradiance. For the base case, we simulated SSR with WVC of 2.8 cm and 1-SSA of 0.06 (with SZA of 60° and AOD of 0.3) as inputs, resulting in $439.9\,\mathrm{W\,m^{-2}}$. When we increased the water vapour column to 3.6 cm, the corresponding decrease in SSR was about $6.8\,\mathrm{W\,m^{-2}}$. However, when we additionally decreased the aerosol absorption (1-SSA) to 0.04, the difference to the base case shrank to $1.8\,\mathrm{W\,m^{-2}}$ and this remaining amount can mostly be explained by the asymmetry parameter, which also exhibits a systematic dependence with WVC (stronger forward scattering by particles grown in humid conditions).

The lower panel of Fig. 6 further illustrates the role of fixed SSA in the observed WVC-dependent bias in the LUT results, which can be avoided with the machine learning methods. It shows the mean ratio of LUT-estimated and AERONET-measured AOD on the right-hand side y axis as a function of water vapour content (so essentially the same results shown by a box-plot in Fig. 4). Additionally, on the left-hand side y axis, the single scattering albedo (estimated for 500 nm) from AERONET measurements is shown as a function of water vapour amount as well. This also demonstrates that the over- and underestimations of the LUT method coincide with SSA range that is under and over the assumed fixed value of 0.92 (shown with red dashed line) respectively. Visibly, the ratio in the right-hand axis of Fig. 6b, reaches one

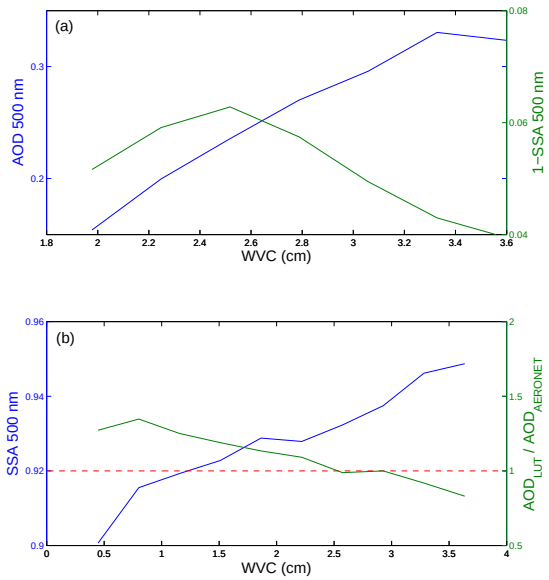

Figure 6. (a) Aerosol optical depth (AOD), water vapour content (WVC) and 1-SSA at 500 nm from the AERONET inversion sky data. **(b)** SSA at 500 nm, WVC and the LUT's predicted AOD divided with the observational AOD (AERONET), with the red line fixed to SSA (500 nm) = 0.92 (as in LUT).

not until SSA is roughly 0.93 instead of 0.92. Presumably, SSA has actually a different wavelength pattern than the one assumed in LUT.

4 Conclusions

We have used several inverse methods to retrieve aerosol optical depth (AOD) from surface solar radiation (SSR) and water vapour content (WVC) measurements (with corresponding solar zenith angle data) taken in Thessaloniki, Greece. Two traditional (look-up table and non-linear regression) and four machine learning methods (Gaussian process, neural network, random forest and support vector machine) were used to retrieve AOD estimates for the years 2005–2008. Then we compared the AOD estimates with collocated AOD measurements by Aerosol Robotic Network (AERONET). Our comparisons showed the following.

AOD estimates based on the LUT method agreed better with AERONET than the NR estimates but apart from RF, the machine learning methods produced AOD estimates that were comparable or better than LUT.

NN and SVM methods reproduced good correspondence to AERONET observations for both low and high AODs while the rest of the methods tended to overestimate low AODs and underestimate high AODs. The main reason for the better performance of these machine learning methods was that there were no constraints of the aerosol single scattering albedo (SSA) in the retrieval. In other words, the methods do not need to explicitly make assumptions on the optical aerosol properties of the atmosphere because they seem to be able to indirectly account for the covariation of WVC and SSA.

When compared with AERONET measurements, the best AOD estimates were retrieved with the machine learning algorithms, but only NN and SVM were also able to generalize accurate estimates for large AODs.

The machine learning methods are sensitive to the selection of the training data set and other constraints, and are generally valid only for the range of variables used for their training; thus care needs to be taken when these methods are employed.

These tools have the potential to be used in the retrieval of AOD from SSR measurements to lengthen the time series of AOD. Historical AOD is essential in the estimation of anthropogenic aerosol effects and in the evaluation of AOD retrievals from space-borne instruments before the 1990s.

The intention of comparing different methods was to test their ability in an "out-of-the-box" configuration. With this in mind, methods were not particularly tuned to reach the best possible results. It is very likely that e.g. optimizing the free parameters used in each of the non-linear modelling approaches, their ability to reproduce observed AOD could be further improved.

Appendix A

Table A1. The statistics between the training and the validation data for the input and the output parameters. The units for SZA, SSR and WVC are degrees, W m^{-2} and centimetres respectively.

Training: Parameter	Max	Min	Average	SD	Median
SZA	78.6	17.5	56.2	15.7	60.0
SSR	1071.9	120.5	522.7	247.1	479.6
WVC	4.12	0.23	2.23	0.73	2.29
AOD	1.06	0.01	0.22	0.12	0.20
Validation: Parameter	Max	Min	Average	SD	Median
SZA	78.7	17.5	60.6	14.7	65.3
SSR	1060.0	113.2	450.2	235.9	384.5
WVC	3.81	0.27	1.87	0.82	1.79
AOD	0.85	0.03	0.24	0.15	0.21

Table A2. The coefficient values of Eq. (1) and errors (SD) for the NR method.

Coefficients	Estimate	SD error
b_0	1.716×10^5	8.372×10^2
b_1	-1.696×10^5	8.272×10^2
b_2	-1.715×10^5	8.363×10^2
b_3	-1.206×10^1	5.727×10^{-1}
b_4	1.694×10^5	8.264×10^2
b_5	5.145×10^0	2.465×10^{-1}
b_6	6.819×10^0	3.728×10^{-1}

Acknowledgements. We thank the AERONET team, principal investigators and other participants for their effort in establishing and maintaining the network. This study is supported by Graduate school in Physics, Chemistry, Biology and Meteorology of Atmospheric Composition and Climate Change: From Molecular Processes to Global Observations and Models. The Academy of Finland Center of Excellence program (project number 272041) is also acknowledged. The financial support by the strategic funding of the University of Eastern Finland is gratefully acknowledged. The author thank Juha Tonttila and Mikko Pitkänen from Finnish Meteorological Institute, Kuopio, for their help with the python (http://python.org) and in the production of the MatLab (http://mathworks.com) box plot figures. Also J. Huttunen thank the Finnish Cultural Foundation, North Savo Regional fund.

Edited by: B. Mayer

References

Ahmad, I., Mielonen, T., Grosvenor, D., Portin, H., Arola, A., Mikkonen, S., Kühn, T., Leskinen, A., Joutsensaari, J., Komppula, M., Lehtinen, K., Laaksonen, A., and Romakkaniemi, S.: Long-term measurements of cloud droplet concentrations and aerosol-cloud interactions in continental boundary layer clouds, Tellus B, 65, 20138, doi:10.3402/tellusb.v65i0.20138, 2013.

Andreae, M. O. and Rosenfeld, D.: Aerosol–cloud–precipitation interactions. Part 1. The nature and sources of cloud-active aerosols, Earth Sci. Rev., 89, 13–41, 2008.

Bais, A. F., Drosoglou, Th., Meleti, C., Tourpali, K., and Kouremeti, N.: Changes in surface shortwave solar irradiance from 1993 to 2011 at Thessaloniki (Greece), Int. J. Climatol., 33, 2871–2876, doi:10.1002/joc.3636, 2013.

Bates, D. M. and Watts, D. G.: Nonlinear Regression Analysis and Its Applications, Wiley, New York, 1988.

Bishop C. M.: Neural Networks for Pattern Recognition, Oxford University Press, Inc. New York, NY, USA, ISBN:0198538642, 1995.

Breiman, L.: Random forests, Mach. Learn., 45, 5–32, 2001.

Burges, C. J. C.: A tutorial on support vector machines for pattern recognition, Data Min. Knowl. Disc., 2, 121–167, 1998.

Carslaw, K. S., Lee, L. A., Reddington, C. L., Pringle, K. J., Rap, A., Forster, P. M., Mann, G. W., Spracklen, D. V., Woodhouse, M. T., Regayre, L. A., and Pierce, J. R.: Large contribution of natural aerosols to uncertainty in indirect forcing, Nature, 503, 67–71, doi:10.1038/nature12674, 2013.

Chang, C.-C. and Lin, C.-J.: LIBSVM: a library for support vector machines, ACM Transactions on Intelligent Systems and Technology, 2, 27.1–27.27, 2011.

Dubovik, O., Smirnov, A., Holben, B. N., King, M. D., Kaufman, Y. J., Eck, T. F., and Slutsker, I.: Accuracy assessments of aerosol optical properties retrieved from AERONET sun and sky-radiance measurements, J. Geophys. Res., 105, 9791–9806, 2000.

Foyo-Moreno, I., Alados, I., Anton, M., Fernandez-Galvez, J., Cazorla, A., and Alados-Arbodelas, L.: Estimating aerosol characteristics from solar irradiance measurements at an urban location in southeastern Spain, J. Geophys. Res.-Atmos, 119, 1845–1859, doi:10.1002/2013JD020599, 2014.

Friedman, J., Hastie, T., and Tibshirani, R.: The elements of statistical learning, Springer Science & Business Media, Berlin, Germany, Vol. 1, 2001.

Geogdzhayev, I. V., Mishchenko, M. I., Terez, E. I., Terez, G. A., and Gushchin, G. K.: Regional advanced very high resolution radiometer–derived climatology of aerosol optical thickness and size, J. Geophys. Res., 110, D23205, doi:10.1029/2005JD006170, 2005.

Granier, C., Bessagnet, B., Bond, T., D'Angiola, A., Denier van der Gon, H., Frost, G. J., Heil, A., Kaiser, J. W., Kinne, S., Klimont, Z., Kloster, S., Lamarque, J.-F., Liousse, C., Masui, T., Meleux, F., Mieville, A., Ohara, T., Raut, J.-C., Riahi, K., Schultz, M. G., Smith, S. J., Thompson, A., van Aardenne, J., van der Werf, G. R., and van Vuuren, D. P.: Evolution of anthropogenic and biomass burning emissions of air pollutants at global and regional scales during the 1980–2010 period, Climatic Change, 109, 163–190, 2011.

Hagan, M. T. and Menhaj, M. B.: Training feedforward networks with the Marquardt algorithm, IEEE T. Neural Networ., 5, 989–993, 1994.

Holben, B. N., Eck, T. F., Slutsker, I., Tanre, D., Buis, J. P., Setzer, A., Vermote, E., Reagan, J. A., Kaufman, Y., Nakajima, T., Lavenu, F., Jankowiak, I., and Smirnov, A.: AERONET – A federated instrument network and data archive for aerosol characterization, Remote Sens. Environ., 66, 1–16, 1998.

Hsieh, W. W.: Machine Learning Methods in the Environmental Sciences Neural Networks and Kernels, Cambridge Univ. Press, 2009.

Huttunen, J., Arola, A., Myhre, G., Lindfors, A. V., Mielonen, T., Mikkonen, S., Schafer, J. S., Tripathi, S. N., Wild, M., Komppula, M., and Lehtinen, K. E. J.: Effect of water vapor on the determination of aerosol direct radiative effect based on the AERONET fluxes, Atmos. Chem. Phys., 14, 6103–6110, doi:10.5194/acp-14-6103-2014, 2014.

IPCC: Climate Change 2013: The Physical Science Basis. Contribution of Working Group I to the Fifth Assessment Report of Intergovernmental Panel on Climate Change, Cambridge University Press, Cambridge, United Kingdom and New York, NY, USA, ISBN 978-1-107-66182-0, doi:10.1017/CBO9781107415324, 2013.

Jackson, J. M., Liu, H., Laszlo, I., Kondragunta, S., Remer, L. A., Huang, J., and Huang, H.-C.: Suomi-NPP VIIRS aerosol algorithms and data products, J. Geophys. Res.-Atmos., 118, 12673–12689, doi:10.1002/2013JD020449, 2013.

Kahn, R. A. and Gaitley, B. J.: An analysis of global aerosol type as retrieved by MISR, J. Geophys. Res.-Atmos., 120, 4248–4281, doi:10.1002/2015JD023322, 2015.

Kudo, R., Uchiyama, A., Yamazaki, A., Sakami, T., and Ijima, O.: Decadal changes in aerosol optical thickness and single scattering albedo estimated from ground-based broadband radiometers: A case study in Japan, J. Geophys. Res., 116, D03207, doi:10.1029/2010JD014911, 2011.

Levy, R. C., Remer, L. A., Kleidman, R. G., Mattoo, S., Ichoku, C., Kahn, R., and Eck, T. F.: Global evaluation of the Collection 5 MODIS dark-target aerosol products over land, Atmos. Chem. Phys., 10, 10399–10420, doi:10.5194/acp-10-10399-2010, 2010.

Llewellyn-Jones, D. and Remedios, J.: The Advanced Along Track Scanning Radiometer (AATSR) and its predecessors ATSR-1

and ATSR-2: An introduction to the special issue, Remote Sens. Environ., 116, 1–3, doi:10.1016/j.rse.2011.06.002, 2012.

Lindfors, A. V., Kouremeti, N., Arola, A., Kazadzis, S., Bais, A. F., and Laaksonen, A.: Effective aerosol optical depth from pyranometer measurements of surface solar radiation (global radiation) at Thessaloniki, Greece, Atmos. Chem. Phys., 13, 3733–3741, doi:10.5194/acp-13-3733-2013, 2013.

McCulloch, W. and Pitts, W.: A Logical Calculus of Ideas Immanent in Nervous Activity, B. Math. Biophys., 5, 115–133, doi:10.1007/BF02478259, 1943.

Olcese, L. E., Palancar, G. G., and Toselli, B. M.: A method to estimate missing AERONET AOD values based on artificial neural networks, Atmos. Environ., 113, 140–150, doi:10.1016/j.atmosenv.2015.05.009, 2015.

Pedregosa, F., Varoquaux, G., Gramfort, A., Michel, V., Thirion, B., Grisel, O., Blondel, M., Prettenhofer, P., Weiss, R., Dubourg, V., Vanderplas, J., Passos, A., Cournapeau, D., Brucher, M., Perrot, M., and Duchesnay, E.: Scikit-learn: Machine Learning in Python, J. Mach. Learn. Res., 12, 2825–2830, 2011.

Rasmussen, C. E. and Williams, C. K. I.: Gaussian processes for machine learning, MIT Press, Massachusetts Institute of Technology, Massachusetts, USA, 2006.

R Core Team: R: A language and environment for statistical computing, R Foundation for Statistical Computing, Vienna, Austria, available at: http://www.R-project.org/ (last access: 4 July 2016), 2014.

Rosenblatt, F. A.: probabilistic model for information storage and organization in the brain, Psychol. Rev., 65, 368–408, 1958.

Santner, T. J., Williams, B. J., and Notz, W. I.: The design and analysis of computer experiments, Springer Science & Business Media, Berlin, Germany, 2013.

Shettle, E. P.: Models of aerosols, clouds and precipitation for atmospheric propagation studies, in: Atmospheric Propagation in the UV, Visible, IR and mm-region and Related System Aspects, no. 454 in AGARD Conf. Proc., 15–1–15–13, 1989.

Smola, A. J. and Schölkopf, B.: A tutorial on support vector regression, Stat. Comput., 14, 199–222, 2004.

Taylor, M., Kazadzis, S., Tsekeri, A., Gkikas, A., and Amiridis, V.: Satellite retrieval of aerosol microphysical and optical parameters using neural networks: a new methodology applied to the Sahara desert dust peak, Atmos. Meas. Tech., 7, 3151–3175, doi:10.5194/amt-7-3151-2014, 2014.

Torres, O., Bhartia, P. K., Herman, J. R., Sinyuk, A., Ginoux, P., and Holben, B.: A long-term record of aerosol optical depth from TOMS observations and comparison to AERONET measurements, J. Atmos. Sci., 59, 398–413, 2002.

Vapnik, V.: The Nature of Statistical Learning Theory, New York: Springer, 1995.

Welch, W. J., Buck, R. J., Sacks, J., Wynn, H. P., Mitchell, T. J., and Morris, M. D.: Screening, predicting, and computer experiments, Technometrics, 34, 15–25, 1992.

FINNISH METEOROLOGICAL INSTITUTE
Erik Palménin aukio 1
P.O. Box 503
FI-00101 HELSINKI
tel. +358 29 539 1000
WWW.FMI.FI

FINNISH METEOROLOGICAL INSTITUTE
CONTRIBUTIONS No. 135
ISBN 978-952-336-026-6 (paperback)
ISSN 0782-6117
Erweko
Helsinki 2017

ISBN 978-952-336-027-3 (pdf)
Helsinki 2017